UNIVERSITY OF CALIFORNIA
RIVERSIDE

Experimental Study of Spin Current Transport in Heterostructures

A Dissertation submitted in partial satisfaction
of the requirements for the degree of

Doctor of Philosophy

in

Physics

by

Yadong Xu

June 2017

Dissertation Committee:
Dr. Jing Shi, Chairperson
Dr. Ward Beyermann
Dr. Vivek Aji

The Dissertation of Yadong Xu is approved:

_____

_____

_____

Committee Chairperson

University of California, Riverside

Acknowledgement

It is an exciting and proud moment to accomplish my Ph.D. study. There are so many happy and painful experiences in this six-year journey, which will become my lifelong memories. I am grateful to the study in UC Riverside, as it prepares me solid foundation for the future.

First I would like to sincerely acknowledge my advisor Prof. Jing Shi, for his patient instructions in research and kind help in life. Prof. Shi is a great scientist with deep insights and careful thinking. His expertise in physics and passions for research motivate me throughout the Ph.D. study. Prof. Shi is also a gracious mentor who provides me a lot of precious suggestions, which help me build up optimistic and proactive attitudes towards life. His guidance will benefit me for the rest of life.

I also would like to acknowledge my committee members, Prof. Ward Beyermann and Prof. Vivek Aji. They give me valuable instructions and suggestions on my research projects. I want to thank my qualifying exam committee members, Prof. Jory Yarmoff and Prof. Jianlin Liu for their useful discussions and comments.

I would like to thank my colleagues in the lab for their assistance in my research, they are Xinfei Liu, Tao Lin, Ray Sachs, Zhiyong Wang, Hamad Alyahyaei, Zilong Jiang, Chi Tang, Zhisheng Lin, Mohammed Aldosary, Bowen Yang, Victor Ortiz, Junxue Li, Yawen Liu, Mark Lohmann, Jhen-Yong Hong, Benjamin Madon, Zhong Shi and Mohammed Alghamdi. I also want to thank my colleagues Dong Gui, Hang Zhang, Xiaoxiao He, Tengfei Miao, Bin Cheng, Peng Wang, Fenglin Wang, Cheng Pan, Yong

Wu, Jun Xu, Renjing Zheng, Changtao Hou, Yanmeng Shi, Weimin Zhou, Supeng Ge, Yi Wu, Shaolong Chen and so many people that I can't list here, for their help and friendship.

I would like to thank my collaborators who provide me great help and extraordinary ideas. They are Prof. Cui-Zu Chang from PSU, Prof. Jagadeesh S. Moodera from MIT, Houchen Chang and Prof. Mingzhong Wu from CSU, Koichi Murata and Prof. Kang L. Wang from UCLA, Prof. Shufeng Zhang from UA, Prof. Roger Lake from UCR, Michael Schneider and Renu Whig from Everspin Technologies, Jian-Guo Zheng from UCI.

I would like to thank Dong Yan, Dexter Humphrey, Nissim Amos, John Butler, Frank Lee and Mark Heiden in the Center for Nanoscale Science and Engineering for their technical assistance to my research. I also want to express my sincere appreciation to Glenda Barraza, Dorothea Northcutt in SHINES and Derek Beving in Department of Physics and Astronomy for their support with great patience.

Last but not least, I want to express my deep gratitude to my family. I want to thank my father Zhanyin Xu and mother Cuihua Wu for raising me up and giving me endless love. I also want to thank my brother Dongfang Xu for his encouragement. Without their support, I wouldn't be able to finish my Ph.D. study.

Acknowledgement of previously published material

1. Part of Chapter 2 has been published in "Yadong Xu, Bowen Yang, Chi Tang, Zilong Jiang, Michael Schneider, Renu Whig and Jing Shi Heat-driven spin transport in a ferromagnetic metal. *Appl. Phys. Lett.* **105**, 242404 (2014)".
2. Chapter 3 has been published in "Junxue Li*, Yadong Xu*, Mohammed Aldosary, Chi Tang, Zhisheng Lin, Shufeng Zhang, Roger Lake and Jing Shi Observation of magnon-mediated current drag in Pt/yttrium iron garnet/Pt(Ta) trilayers. *Nature Commun.* **7**, 10858 (2016)". (* These authors contributed equally to this work.)
3. Part of Chapter 4 has been published in "Zilong Jiang, Cui-Zu Chang, Massoud Ramezani Masir, Chi Tang, Yadong Xu, Jagadeesh S. Moodera, Allan H. MacDonald & Jing Shi Enhanced spin Seebeck effect signal due to spin-momentum locked topological surface states. *Nature Commun.* **7**, 11458 (2016)".

ABSTRACT OF THE DISSERTATION

Experimental Study of Spin Current Transport in Heterostructures

by

Yadong Xu

Doctor of Philosophy, Graduate Program in Physics
University of California, Riverside, June 2017
Dr. Jing Shi, Chairperson

Spin current transport plays an important role in modern solid state physics. Research efforts on this field not only reveal fundamental principles, but also promote engineering applications. We explore spin current transport in various heterostructures.

We first give a brief introduction to the recent advancements in spin current transport, including the observation of spin Hall effect (SHE) in materials with strong spin-orbit coupling, the discovery of spin Seebeck effect (SSE) in both conductive and insulating magnetic materials, and the realization of spin current transport without free charge motion in magnetic insulators.

Then we present the results related to spin current transport in ferromagnetic metal (FM)/normal metal (NM) heterostructures, driven by spin pumping or heat flow. In the spin pumping experiment, we observe inverse SHE signals at ferromagnetic

resonance states and anomalous Nernst effect (ANE) signals due to a vertical temperature gradient. In the longitudinal SSE experiment, we disentangle SSE, ANE and proximity effect contributions and discover the spin current draining effect, i.e., an adjacent NM changes the spin chemical potential and induces an additional spin current in the FM.

The third part provides details about the observation of magnon-mediated current drag effect. We grow high quality Pt/yttrium iron garnet (YIG)/Pt(Ta) trilayer heterostructures and realize electronic signal transmission through YIG, a magnetic insulator, by magnon current. A charge current in the bottom Pt layer induces spin accumulation by SHE. The electronic spins convert to magnons in YIG and convert back to electronic spins in the top Pt(Ta) layer.

The study of topological SSE in YIG/topological insulator (TI) heterostructures is presented at last. Magnons driven by a vertical temperature gradient are converted to a charge current in TI surface states. We tune the Fermi level by changing TI composition ratio or applying a top gate and demonstrate the dominant role of the topological surface states in the magnon-charge conversion.

Contents

List of Figures

Chapter 1 Introduction to recent advancements in spin current transport

1.1 Introduction to spintronics

Spintronics adds the spin degree of freedom to traditional charge transport in condensed-matter materials and devices. The discovery of giant magnetoresistance (GMR) is considered as the beginning of spintronics[1]. GMR has achieved a big success in electronic applications as it greatly enhances the capacity of magnetic data storage. Although the initial application of spintronics is only focused on information storage, combining charge property of electrons with spin has appealing potentials in achieving nonvolatile memory and logic devices with less energy consumption, higher data processing speed, and increased integration densities. To realize the potentials, developing efficient ways for spin current generation, manipulation, and detection is necessary. Some of recent advancements in spin current transport provide new views to understand the fundamental phenomenon and inspire possible new applications. These recent advancements focus on several subfields: spin orbitronics, spin caloritronics and magnon spintronics.

1.2 Spin orbitronics

Spin orbitronics aims to utilize spin-orbit coupling to generate and detect spin currents. In early spintronics exploration, partially spin polarized currents are usually generated by passing a charge current through a ferromagnetic metal or a semiconductor. Recently, spin-orbit interaction is found to provide new ways to efficiently generate spin

currents from charge currents flowing through nonmagnetic materials. Among them, the spin Hall effect (SHE) has attracted great interests in the spintronics community.

In a SHE, a charge current passing through a material with strong spin-orbit coupling can generate a transverse pure spin current with spin polarized perpendicular to both the charge and spin currents[2]. A pure spin current applied to the same material can generate a charge current. This is the inverse spin Hall effect (ISHE). SHE and ISHE are reciprocal processes sharing the same origins. SHE is due to extrinsic spin-dependent scattering[3] (extrinsic SHE) or intrinsic mechanism related to electronic band structure[4,5] (intrinsic SHE).

SHE is first observed with optical method in GaAs. A magneto-optical Kerr microscope is used to spatially image the spin polarization due to SHE while a charge current is applied[6]. The SHE observed here is ascribed to the extrinsic effect. It is also reported that circularly polarized electroluminescence at opposite edges of a GaAs channel is detected with coplanar *p-n* diodes[7]. Here it is believed to originate from the intrinsic SHE. A few years later, the optical generation of the ISHE is reported in an experiment with a GaAs/Pt bilayer structure. Circularly polarized light generates spin polarized carriers in GaAs and induced pure spin current is converted to an electrical voltage in Pt due to ISHE[8].

The detection of SHE with transport methods are first proposed by Hirsch[2] and Zhang[9]. Hirsch proposed a device that consists a metallic slab and a transverse strip which connects the edges of the slab. SHE induced spin accumulation in the slab can be detected by the transverse strip through ISHE. Zhang proposed to measure the spin

accumulation via a ferromagnet probe, which is similar to nonlocal spin valve devices. The observation of SHE via electrical method is first achieved in a geometry that consists a ferromagnetic metal (FM) spin injector and a normal metal (NM) Hall cross spin detector[10]. The perpendicularly polarized spins diffuse to the Hall cross and generate a charge voltage due to ISHE. The ISHE is also observed in a FM/NM bi-layer structure, where the spin current is injected from FM to NM with the spin pumping technique[11].

SHE also induces a new type of magnetoresistance in a magnetic insulator/NM bi-layer structure[12,13]. A charge current flowing in the NM generates a spin current towards the magnetic insulator. When the magnetization aligns with the spin polarization, the spin backflow generates an ISHE current to the longitudinal current. When the magnetization is perpendicular to spin polarization, the spin current absorption by the magnetic insulator is maximum. This phenomenon is called spin Hall magnetoresistance.

SHE is found to have modulation on magnetization damping[14]. When a FM/NM bilayer is driven to ferromagnetic resonance (FMR), the spin pumping effect takes away the angular momentum and contributes additional relaxation to the precessing magnetization, which is observed from the linewidth broadening compared with FM single layer film. In turn, a DC current inside the NM will generate a spin current flowing towards the interface due to SHE. The spin current exerts a spin transfer torque (STT) on the precessing magnetization and modulates the magnetization relaxation of the FM layer. Furthermore, the SHE in the NM can excite magnetic precession in the adjacent FM[15]. A longitudinal microwave current in the FM/NM bilayer generates a transverse alternating spin current in the NM due to SHE. The spin current transfers angular

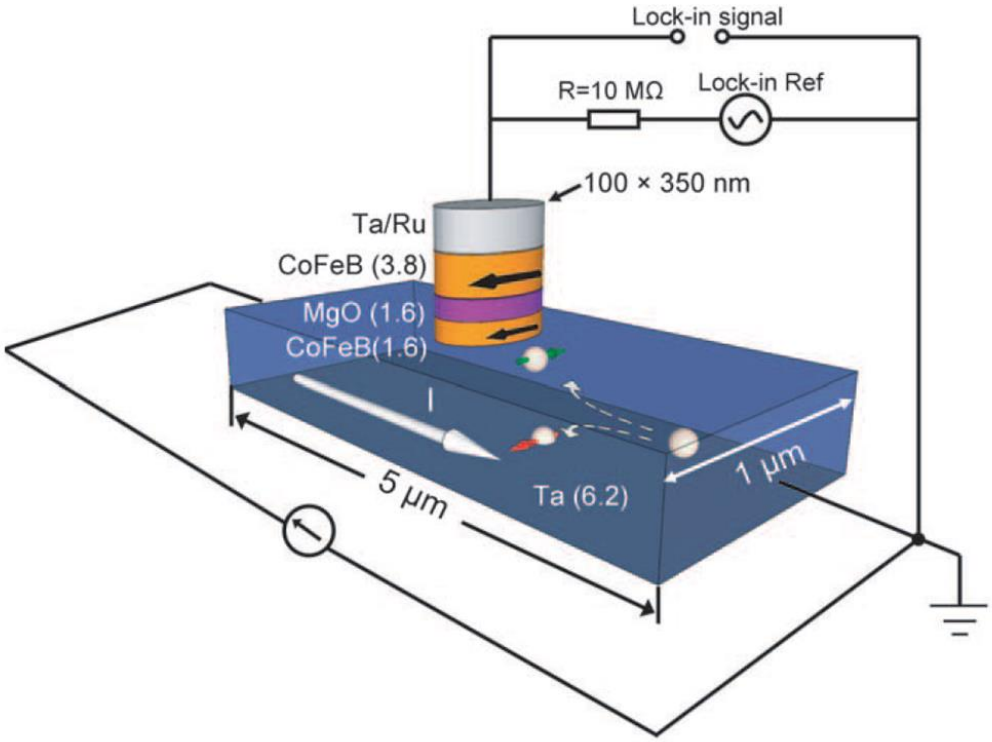

Figure 1-1 Room temperature magnetic switching for an in-plane magnetized nanomagnet induced by Spin Hall effect. A DC current flowing in the Ta film generates a spin transfer torque and switches the bottom CoFeB of the magnetic tunnel junction. Adapted from Liu, *et al*. *Science* **336**, 555-558 (2012).

momentum to the FM, applies an oscillatory STT on the magnetic moments and induces it to FMR state. This effect helps to quantitatively determine the spin current and spin Hall angle of the NM. One of the most promising applications of SHE is to switch the magnetization of a FM. It is demonstrated that in a FM/NM bilayer, when the current density is large enough, the STT generated by spin current is able to switch the perpendicularly magnetized FM[16,17,18]. The in-plane magnetic switching is also observed in a magnetic tunnel junction (MTJ) based device[19]. As shown in Fig. 1-1, a CoFeB/MgO/CoFeB tunnel junction is fabricated on top of a Ta film. A large current

passing through the Ta layer generates a vertical spin current, which switches the magnetization of the adjacent CoFeB free layer by STT. The MTJ is used for read out of the switching. This means SHE could solve the reliability problem of traditional MTJ devices and provide a new direction for future memory technologies.

1.3 Spin caloritronics

Spin caloritronics is a newly emerged area and has attracted intense research efforts recently. It focuses on the non-equilibrium coupling of spin, charge and heat flow in magnetic materials and structures. The interaction of heat current and spin current may help to develop energy efficient devices to reuse waste heat.

In a conducting ferromagnet, a temperature gradient can drive a spin current due to the spin dependent Seebeck effect[20]. If a NM is attached to a FM, a spin current will be injected into the NM due to the conservation of charge and spin currents. This heat driven spin injection is observed in a non-local lateral spin valve structure[21]. As shown in Fig. 1-2, a charge current in a FM strip (FM_1) generates heat. A NM is attached to one side of the FM strip acting as a heat sink. The heat current from FM_1 to the NM injects a pure spin current into the NM. The spin polarization follows the magnetization direction of the FM. The spins diffuse towards a second FM (FM_2) attached to one side of the NM, and generate an electrical potential between FM_2 and the NM, depending on its magnetization direction. This potential is measured by selectively switching the magnetization of the two FMs.

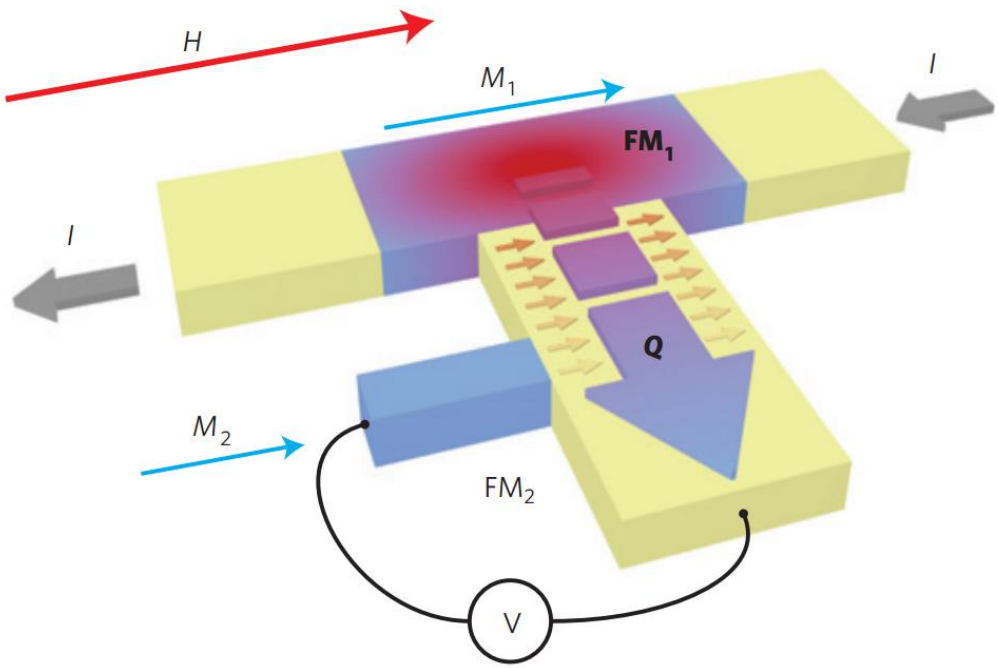

Figure 1-2 Schematic diagram of heat driven spin injection from a ferromagnetic into a normal metal. A charge current flows in a ferromagnet (FM_1) generate Joule heat which flows into the adjacent normal metal. The heat flow drives a spin current across the interface. Then an electric voltage builds up between the normal metal and a second ferromagnet (FM_2). Adapted from Slachter, *et al. Nature Phys.* **6,** 879–882 (2010).

The opposite process, a spin-dependent Peltier effect has also been observed in a dedicated spin-valve pillar nanostructure[22]. The spin-valve consists two FM layers separated by a non-ferromagnetic metal. In the spin valve, a spin current flowing in the vertical direction induces a heat current and associated temperature changes, which is detected by a thermocouple under the spin valve.

The discovery of spin Seebeck effect (SSE) greatly extends the scope of spin caloritronics. SSE has a completely different physical origin from the above spin-dependent Seebeck effect, because the conduction electrons contribution is negligible[20].

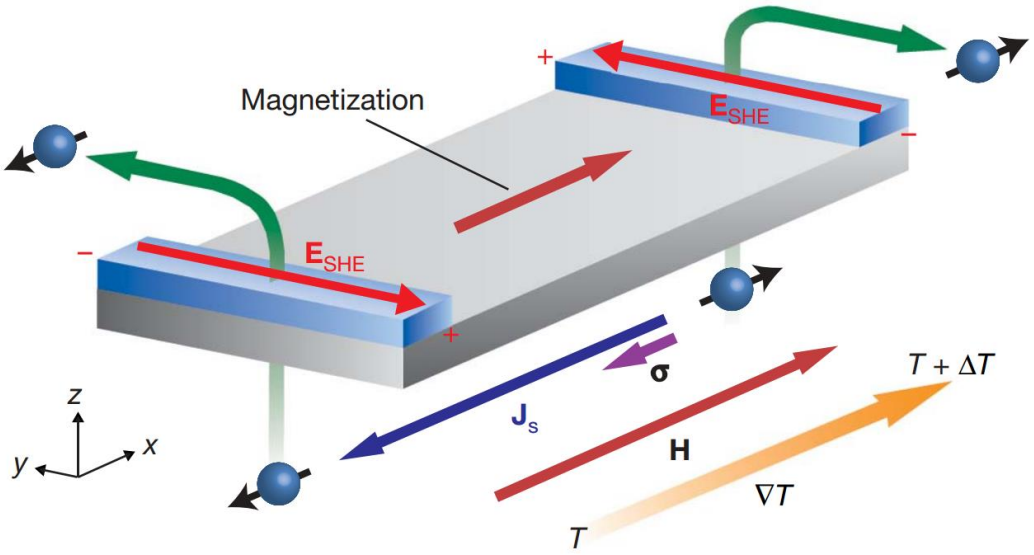

Figure 1-3 Schematic illustration of spin Seebeck effect detection. $\boldsymbol{\sigma}$, J_s and E_{SHE} respectively denote the spin polarization vector of the ferromagnet, the heat driven spin current direction in the ferromagnet and the electric voltage induced by the ISHE in the normal metal. Adapted from Uchida, et al. *Nature*, **455**, 778-781 (2008).

As shown in Fig. 1-3, SSE is detected by measuring the transverse electromotive force in a NM attached to the ferromagnet with a temperature gradient[23]. The ferromagnet has an unbalanced spin chemical potential along the temperature gradient and inject a spin current into the NM. The spin current is converted to an electric voltage by the ISHE. The generated voltage is relatively large because it scales linearly with the NM length, especially for heavy metals with strong spin-orbit coupling, such as Pt and Ta. The SSE has been demonstrated in different material systems including ferromagnetic metals (NiFe)[24], magnetic insulators (yttrium iron garnet)[25] and ferromagnetic semiconductors (GaMnAs)[26]. SSE is typically detected in a transverse configuration[23] and a longitudinal configuration[27]. In the transverse geometry, the SSE signal is easily contaminated by the anomalous Nernst effect due to a spurious out of plane temperature gradient[28]. The

longitudinal geometry is an ideal set up for SSE in magnetic insulators. The combination of longitudinal SSE and ISHE is a promising candidate for thermoelectric conversion technology, because it generates electric voltage directly from heat flow with a simple film structure. The voltage scales linearly with the film size, which makes it useful in large area heat driven electric power generation[29].

1.4 Magnon spintronics

Spin wave is collective excitations of the electron spins in ferromagnetic metals and insulators. Magnons are quantized spin wave, i.e., the dynamic eigen-excitations of a magnetic material[30]. Magnon spintronics utilize magnon carried spin currents to transmit and process information. Magnon currents have nanometer wavelength, are free from electron migration induced Joule heating, can convey spin information over macroscopic distances, can be manipulated by interference, so they have potentials for novel computing technologies.

Spin waves are usually excited in thin films of magnetic material, such as polycrystalline permalloy which is suitable to integrate in Si base electronic devices, and yttrium iron garnet (YIG) which has extremely low damping and long spin diffusion length. Traditionally, magnons are excited by the inductive microwave technique. A microwave current flowing in a nearby antenna induces an alternating Oersted field on the magnetic material and drives the magnetization to precess. This technique is easy to control the frequency, wavelength and phase of the injected magnons. As mentioned above, SSE exists in a magnetic insulator when it experiences a temperature gradient,

because heat current drives the flow of magnons. So, heat flow is also an import method to excite magnons[25]. SHE based STT is an important method to combine magnonic devices with DC electric current. One advantage is that a common charge current in a normal metal can generate a significant STT on an adjacent magnet since the spin current flows in an area much larger than the charge current. The other advantage of the SHE induced SST is that no electric current is required inside the magnetic layer, so the magnet can be a magnetic insulator with low damping constant and long magnon diffusion length. It is demonstrated that a SHE induced STT drives a spin wave in a YIG film and the spin wave propagates to a macroscopic distance[31]. In another work, the complete compensation of the spin wave damping by STT in a YIG/Pt microdisk is achieved[32]. In the experiment, a YIG/Pt film is etched to a 5 μm diameter disk and a DC current is applied in the Pt layer. A magnetic resonance force microscope is used to measure the FMR linewidth for various current density. The magnetic losses of spin-wave modes can be increased or decreased by a factor of 5 depending on the polarity and intensity of the DC current.

The conversion of magnon current into electron current is usually achieved by measuring the spin wave induced AC current inside a strip antenna or a coplanar antenna. The combination of spin pumping and ISHE is also a convenient way to detect magnon current electrically. It is first reported in a FM/NM structure, where the FM is driven to FMR state in a microwave cavity and a spin current flowing from the FM to NM is converted to an electrical voltage by ISHE[11]. Later, this magnon to electron conversion is reported in a YIG/Pt bilayer structure[31]. Intense research efforts have been made to

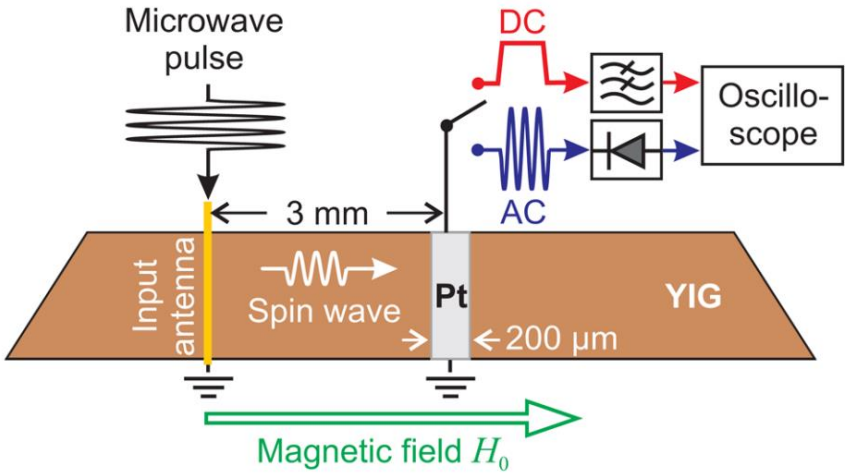

Figure 1-4 Schematic diagram of the detection of a propagating spin wave. The spin wave is excited by a strip antenna. It propagates along the YIG waveguide and is detected by a Pt strip 3 mm away from the antenna, due to spin pumping and ISHE. Adapted from Chumak, *et al. Appl. Phys. Lett.* **100**, 082405 (2012).

understand the phenomenon related to the thicknesses of the NM layer[33–35] and the YIG layer[36,37], the interface quality[38,39] and the spin-wave modes[40,41]. The detection of traveling spin waves is also demonstrated by this spin pumping and ISHE combination[42]. In the experiment, a long YIG strip acts as a waveguide and an antenna excites spin wave packet at one end of the waveguide. The spin wave propagates along the YIG strip and is detected at a 3 mm separated Pt line as an ISHE voltage signal. This indicates the possibility to use spin wave to transfer information over up to centimeter distances in magnonic devices. Furthermore, it is observed that exchange magnons of submicron wavelengths can still efficiently contribute to the spin pumping in YIG/Pt bilayers[43], which is not detectable by optical methods. This is important or further miniaturization of the magnonic spin devices, because only short-wavelength exchange magnons can be processed on the nanometer scale.

Chapter 2 Spin transport in ferromagnetic metal/non-magnetic heavy metal bilayers

2.1 Introduction to experimental observation of spin Hall effect

SHE was first proposed by Hirsch in a paramagnetic metal[2]. When a charge current is applied, spin up electrons are scattered preferentially in one direction perpendicular to both charge current and spin polarization, and spin down electrons in the opposite direction, thus a transverse pure spin current is generated. The electrons are scattered with the same mechanisms that account for anomalous Hall effect in a magnetic metal, which include skew scattering by impurities and phonons, and the "side jump" mechanism. The comparison of Hall effect and SHE is depicted in Fig. 2-1. In the Hall

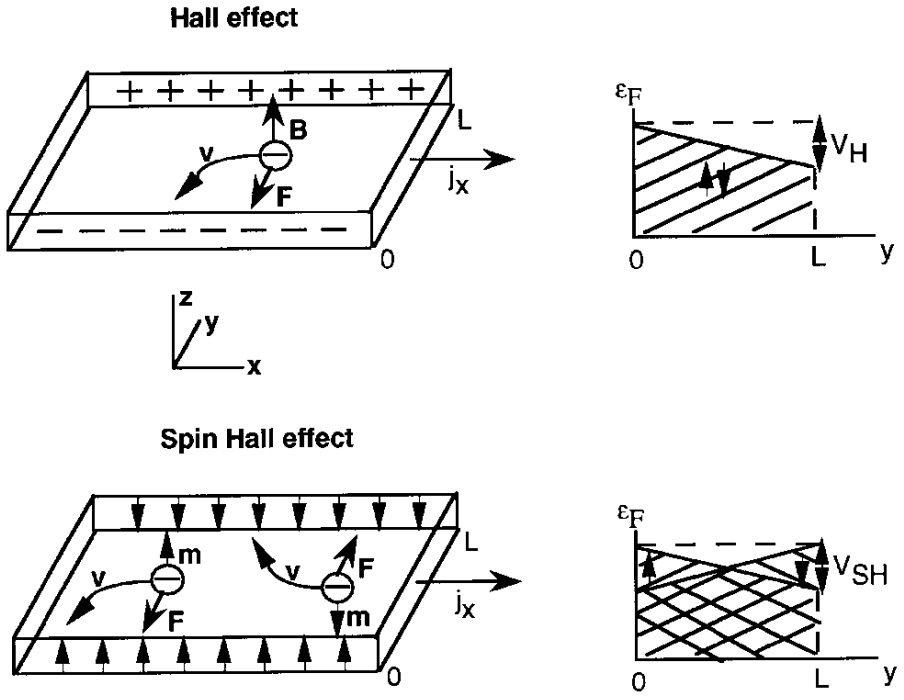

Figure 2-1 Comparison of Hall effect and spin Hall effect in a slab geometry. Adapted from Hirsch *Phys. Rev. Lett.* **83**, 1834-1837 (1999).

effect, electrons are deflected by Lorenz force and accumulate on the edges of the conductor. At a specific position along y direction, the Fermi levels of up and down spins are the same. The difference of Fermi levels on two sides of the sample results in the Hall voltage V_H. However, in the SHE, spin up electrons and spin down electrons are scattered to opposite direction and accumulate on opposite edges of the conductor. For spin up and spin down electrons, the difference in Fermi levels at two edges of the conductor are both V_{SH}, but have opposite sign.

This asymmetry scattering for up spins and down spins is called extrinsic mechanism[2,9,44]. An intrinsic mechanism due to topological band structures is also proposed to explain SHE[4,5]. Ultimately, both extrinsic and intrinsic mechanisms come from electron relativistic motion or spin orbit interaction.

SHE has been first observed in a semiconductor by optical method[6]. When a charge current is applied in a GaAs semiconductor channel, electrons accumulate near the two edges with opposite spin polarization. The out of plane spin polarization is imaged with Kerr rotation microscopy. Fig. 2-2 is a two-dimensional image of the entire sample. The red and blue colors denote the accumulated spin density with opposite signs. The polarization effect is homogeneous over almost entire semiconductor channel, consistent with the predictions of the SHE.

SHE has also been observed with direct electrical measurements[10] in a diffusive metal conductor[10]. As illustrated in Fig. 2-3(a), an aluminum (Al) Hall cross is oxidized to form a tunnel barrier and contacted with two ferromagnetic electrodes FM1 and FM2. An external magnetic field $B_\perp$ is applied perpendicular to the substrate to align the

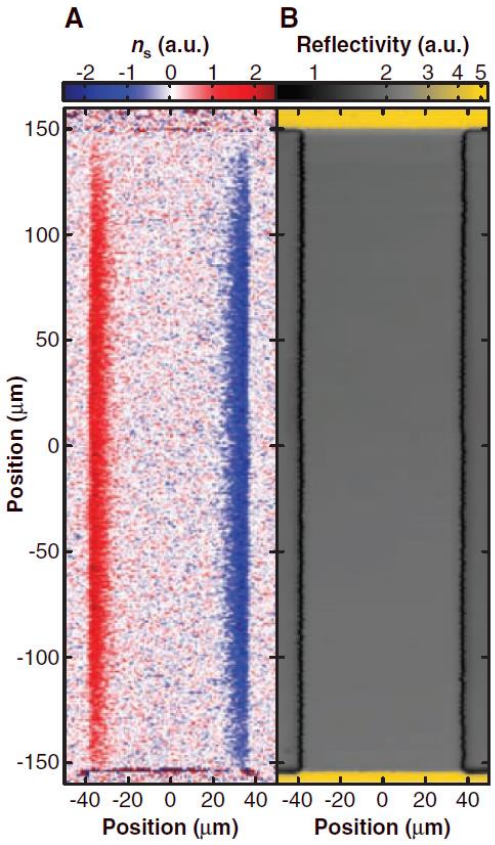

Figure 2-2 Two-dimension images of spin intensity, n_S, and reflectivity, for a GaAs sample measured at T=30K. Adapted from Kato, *et al*. *Science* **306**, 1910-1913 (2004).

magnetization M of FM1 with an angle θ. A spin-polarized charge current is injected from FM1 through the tunnel barrier into the Al and drained away from the Hall cross (Fig. 2-3(b)), resulting in a pure spin current diffusing from FM1 to the cross area. With SHE, the pure spin current induces an unbalanced charge accumulation at the Hall cross in the transverse direction, and a spin Hall voltage, V_{SH}, is measured between the two Hall probes. The spatial dependence of spin-up and spin-down electrochemical potential, $\mu_{\uparrow,\downarrow}$, and associated spin current, J_S, are depicted in Fig. 2-3(c).

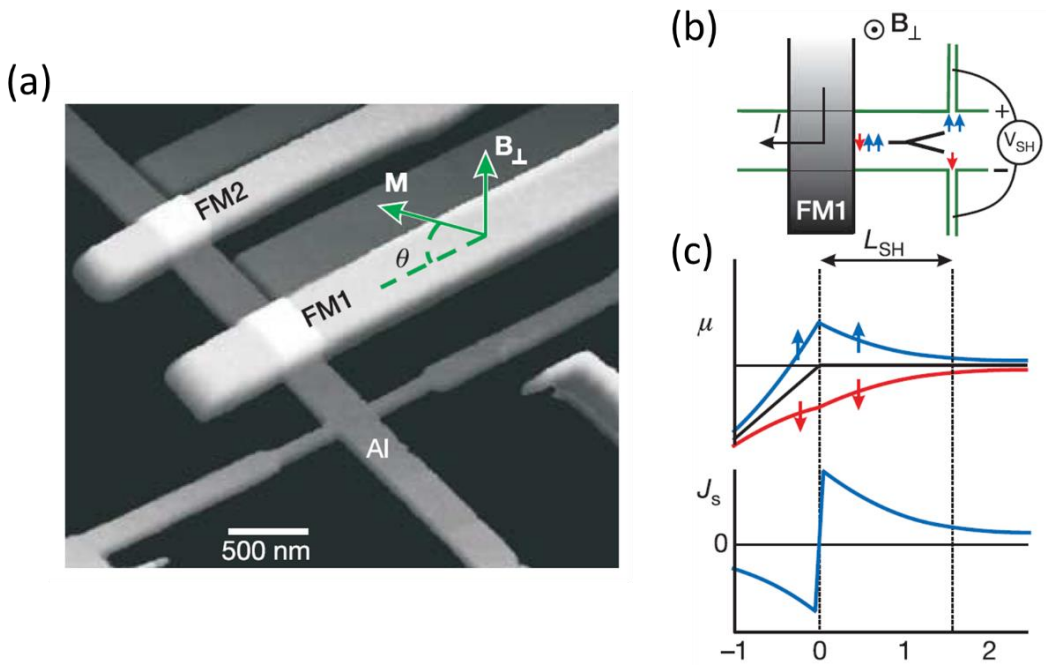

Figure 2-3 Device image and spin Hall effect measurement scheme. An out of plane magnetized ferromagnetic electrode FM1 and a tunnel barrier are utilized to inject polarized spins into a diffusive metal conductor, Al. An induced charge voltage results from spin to charge conversion through spin Hall effect is observed from the two electrodes of the Al Hall cross. Adapted from Valenzuela, *et al*. *Nature* **442**, 176-179 (2006).

Saitoh *et al*. utilized spin pumping to inject a pure spin current from a FM to a paramagnetic metal and observed the conversion of the spin current into a charge current, which is the inverse process of SHE (ISHE)[11]. In the setup illustrated in Fig. 2-4, a microwave and an external magnetic field H are applied to a NiFe film. Once H and microwave frequency fulfill the FMR condition, angular momentum transfers from the precessing local spins to the conduction electrons. The spin polarization diffuses to the adjacent paramagnetic metal Pt as a pure spin current, J_S. Inside Pt, J_S is converted to a transverse charge current J_C through ISHE, and charge accumulates at the two edges of the sample.

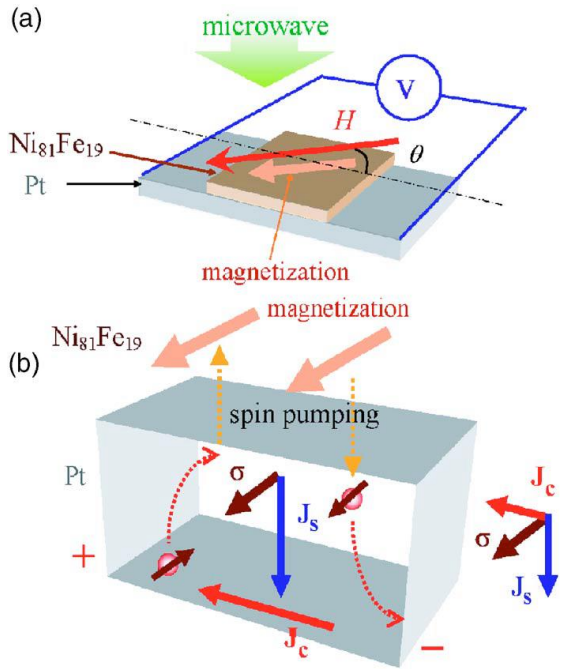

Figure 2-4 Schematic illustration of ISHE measurement by injecting a pure spin current from NiFe to Pt through FMR. J_S is the spin current defused from the interface of NiFe and Pt layers. J_C denote the charge current converted from J_S. $\boldsymbol{\sigma}$ is the spin polarization vector of the spin current. J_C, J_S and $\boldsymbol{\sigma}$ are perpendicular to each other. Adapted from Saitoh, *et al*. *Appl. Phys. Lett.* **88**, 182509 (2006).

2.2 Spin transport in NiFe/Pt bilayers driven by spin pumping

2.2.1 Sample preparation

We first use standard photolithography to define a 50 μm wide strip on a high resistance GaAs substrate. Then a 15 nm thick NiFe film and a 15 nm thick Pt film are consecutively deposited on it in a AJA sputter system without breaking the vacuum. After a lift-off process in Acetone, only the strip area of the NiFe/Pt stays on the substrate. A second photolithography process is used to define a coplanar wave guide (CPW) which consists three paralleled strips on the substrate. Each strip has a width of 100 μm and the gaps between strips are 80 μm. The CPW pattern is carefully aligned to make sure the

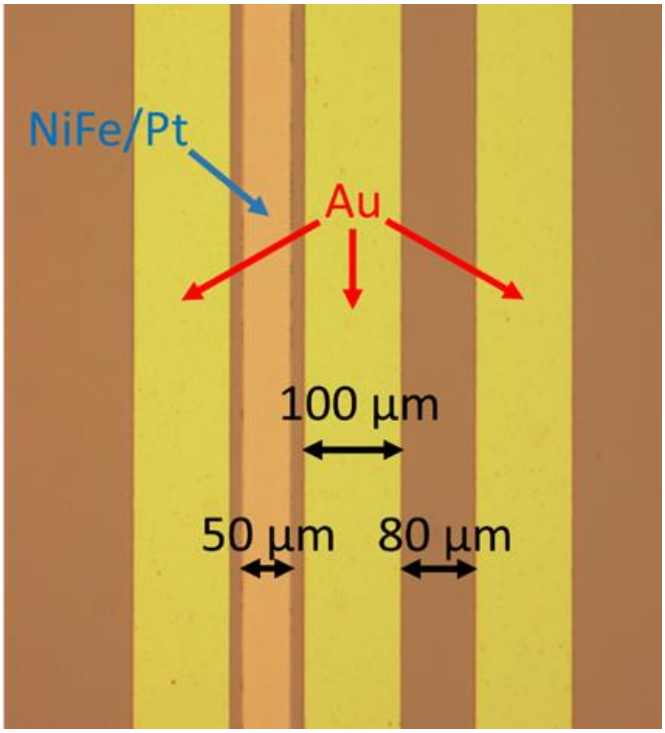

Figure 2-5 Image of a spin pumping sample consists of a long NiFe/Pt strip and an Au coplanar wave guide.

NiFe/Pt strip is exactly along the middle of two strips. Then a 100 nm thick Au film is deposited in an electron-beam evaporator. After a second lift-off process, Au stays on the CPW pattern area. Fig. 2-5 is an image of one sample.

2.2.2 Measurement setup

As illustrated in Fig. 2-6, a static external magnetic field, *H*, is applied by an electric-magnet in the sample plane along x-axis to align the magnetization of NiFe. The microwave, typically with a frequency of several GHz, comes out from a microwave generator. It is first modulated by an electric switch controlled by a TTL signal with a frequency of 1 kHz generated by a lock-in amplifier. The microwave is then sent into the

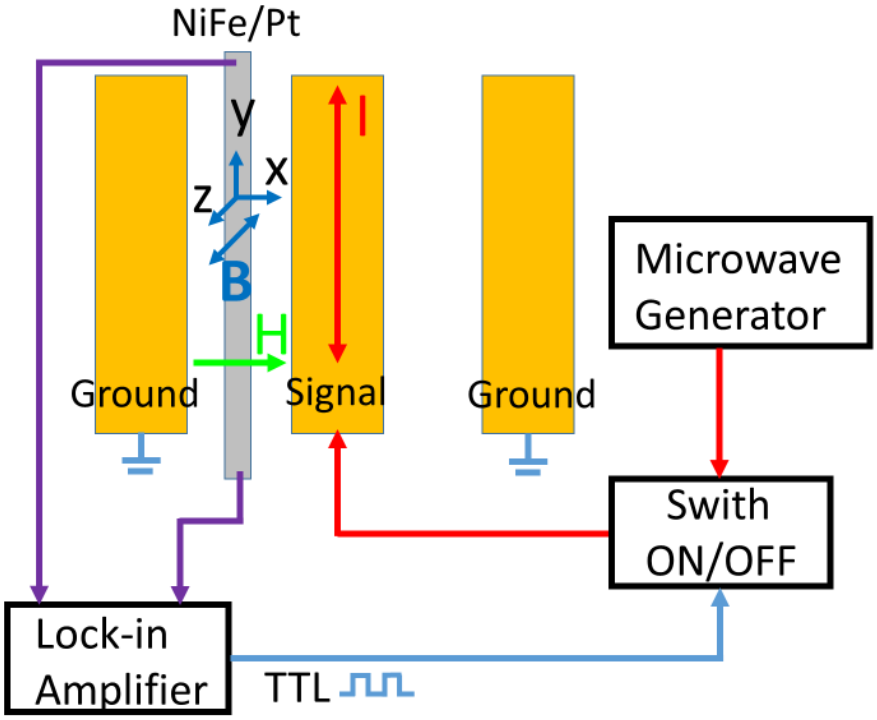

Figure 2-6 Schematic illustration of the spin pumping measurement setup.

signal line of the CPW through a SMA connector. The microwave current *I* in the signal line generates a small out of plane oscillating magnetic field *B* on the NiFe/Pt sample. The signal generated from the NiFe/Pt strip is monitored by the same lock-in amplifier.

2.2.3 Spin pumping results

As illustrated in Fig. 2-7, the magnetization of NiFe, *M*, is aligned by *H* along x-axis. The oscillating *B* is perpendicular to *M*, along z-axis. The generated torque by *B* drives *M* to precess in yz-plane. When *H* and the microwave frequency *f* reach resonance condition, a spin current J_S is pumped into Pt. The spin current is deflected along y-axis due to ISHE and generate a charge current J_C. Charge accumulates at the two ends of the

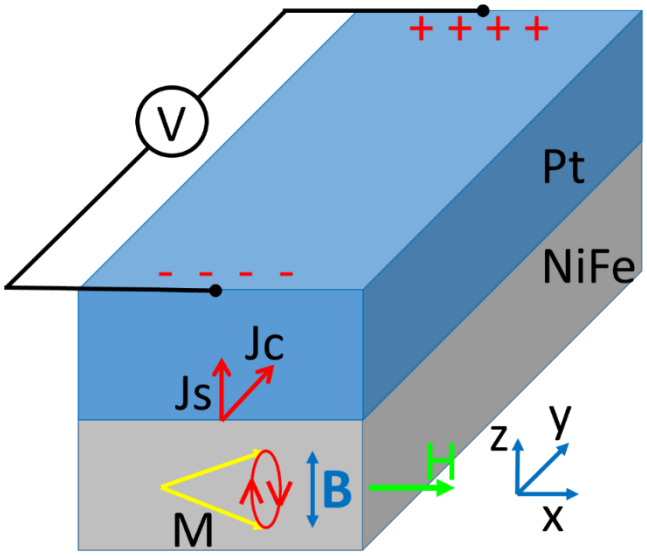

Figure 2-7 Schematic illustration of the DC voltage *V* generated from ISHE through spin pumping.

Pt strip to form a static DC voltage *V*. As the injected microwave is switched on and off with a modulation frequency of 1 kHz, *V* is also turned on and off at the same frequency and picked up by the lock-in amplifier.

Fig 2-8 shows three typical curves of *V* from the NiFe/Pt with different microwave power, *P*. *f* is fixed at 8 GHz. For a specific *P*, *V* has a peak at *H* = 900 Oe and a dip at *H* = -900 Oe, which correspond to the FMR states of NiFe. The magnitude of the peak and the dip are similar but with opposite sign. This sign difference of *V* at positive and negative *H* comes from the opposite spin polarization of the electrons injected into Pt when *M* is aligned by *H* to opposite direction. We notice that a small voltage step, ΔV, exists at *H* = 0 for each curve. These steps are more obvious for *f* = 4 GHz, as shown in Fig. 2-9. We take the peak height at FMR as the resonance signal V_{FMR}. It scales linearly with respect to microwave power *P*, which is plotted in Fig. 2-10.

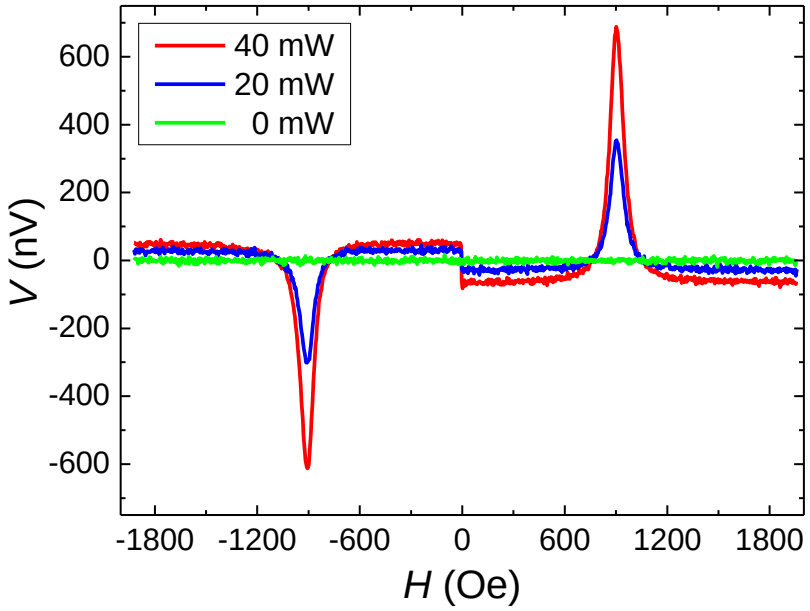

Figure 2-8 DC voltage *V* generated in the NiFe/Pt while sweeping H for three different microwave power. *f* is fixed at 8 GHz.

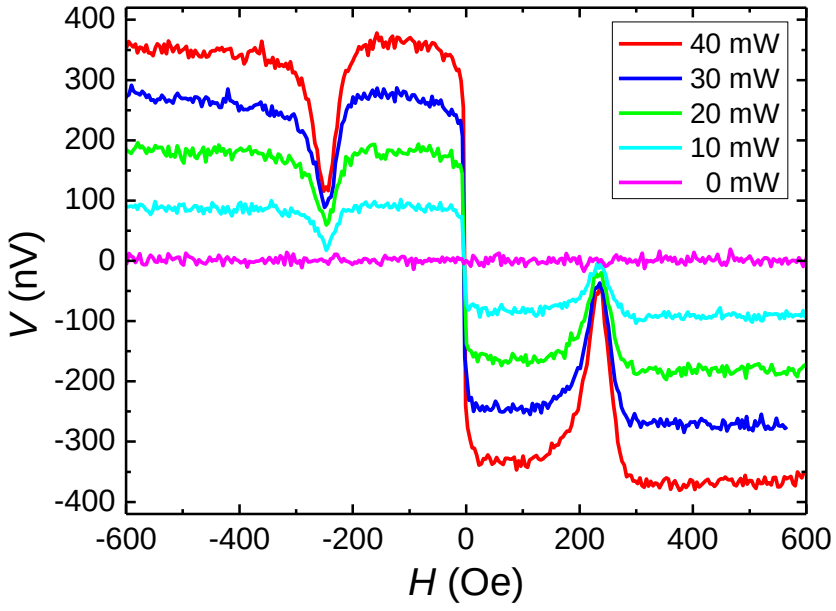

Figure 2-9 DC voltage curves for *f* fixed at 4 GHz. The voltage steps are more obvious than those when *f* is 8 GHz.

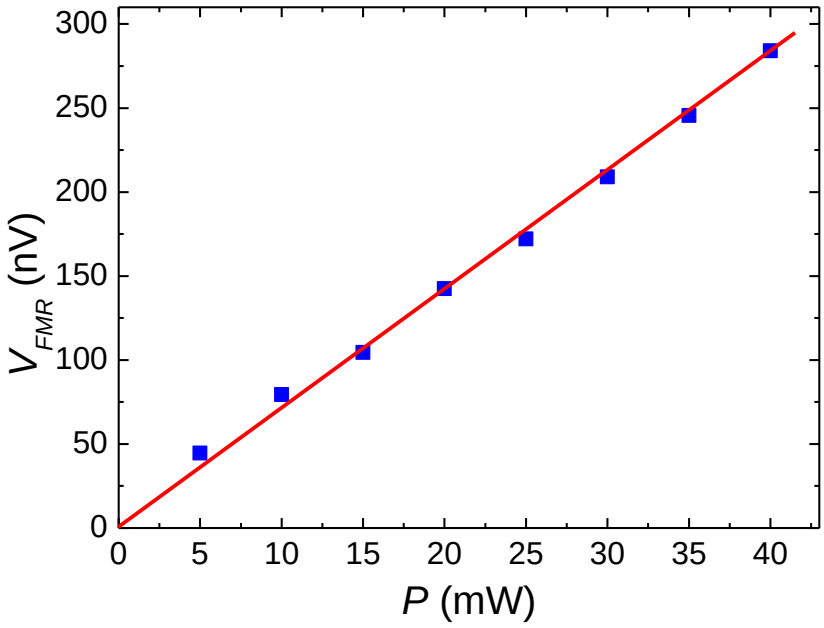

Figure 2-10 Resonance signal vs. microwave power with frequency of 4 GHz. The red line is a linear fit.

Similarly, the step height ΔV vs. P is plotted in Fig. 2-11. The linear fit indicates ΔV could be related to a thermal effect. Later we will come back to this phenomenon for detailed explanation. Fig. 2-12 shows the output voltage V vs. external field H for various microwave frequencies. The resonance signal V_{FMR} is different for each frequency f due to impedance matching of the microwave and the CPW. The resonance field, H_{FMR}, increases with f from 235 Oe for 4 GHz up to 1345 Oe for 10 GHz. Fig. 2-13 shows f as a function of H_{FMR}. It is well fitted by the Kittel formula:

$$f = \frac{\gamma}{2\pi}\sqrt{H_{FMR}(H_{FMR} + 4\pi M_s)}, \tag{2-1}$$

where γ is the gyromagnetic ratio and M_s is the saturation magnetization for NiFe.

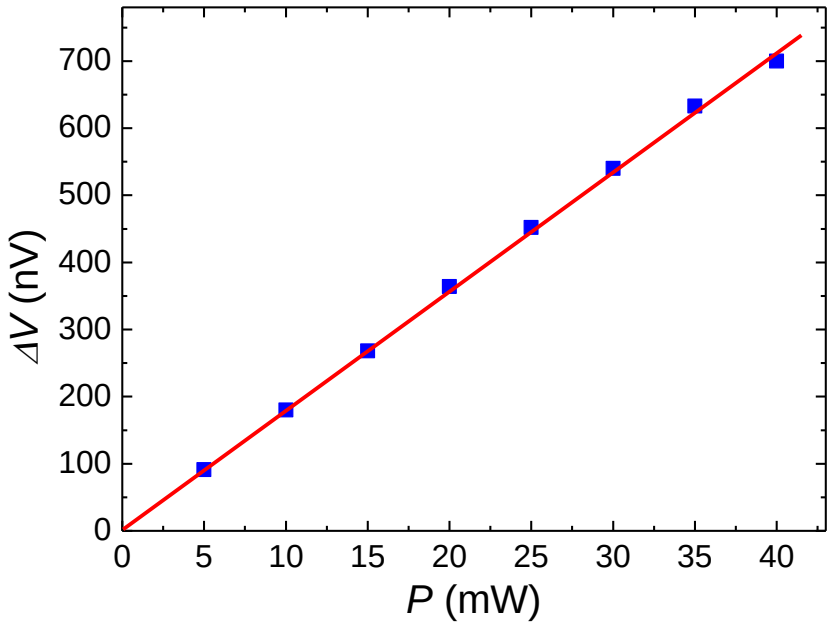

Figure 2-11 Voltage step at $H = 0$ vs. microwave power. The red line is a linear fit.

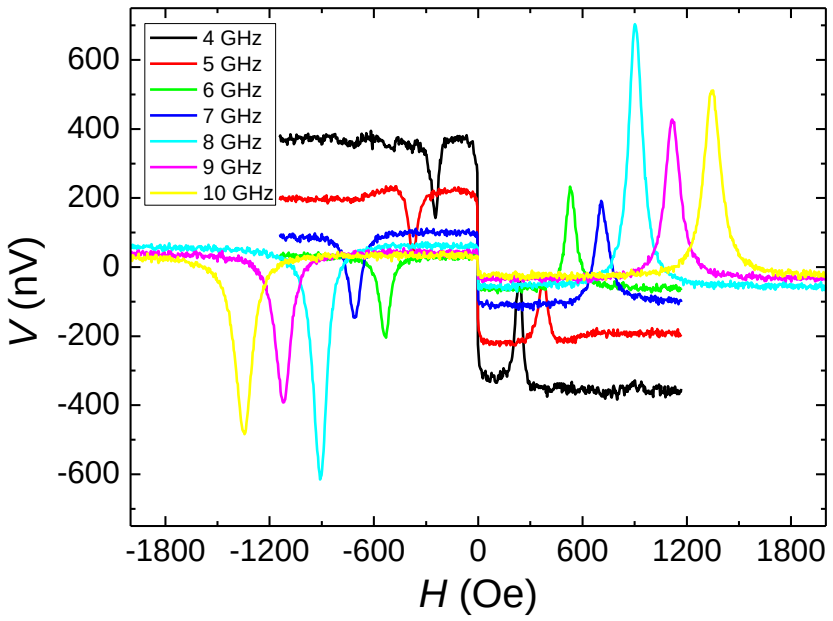

Figure 2-12 Spin pumping signal for frequencies ranging from 4 to 10 GHz. The microwave power is 40 mW for all frequencies.

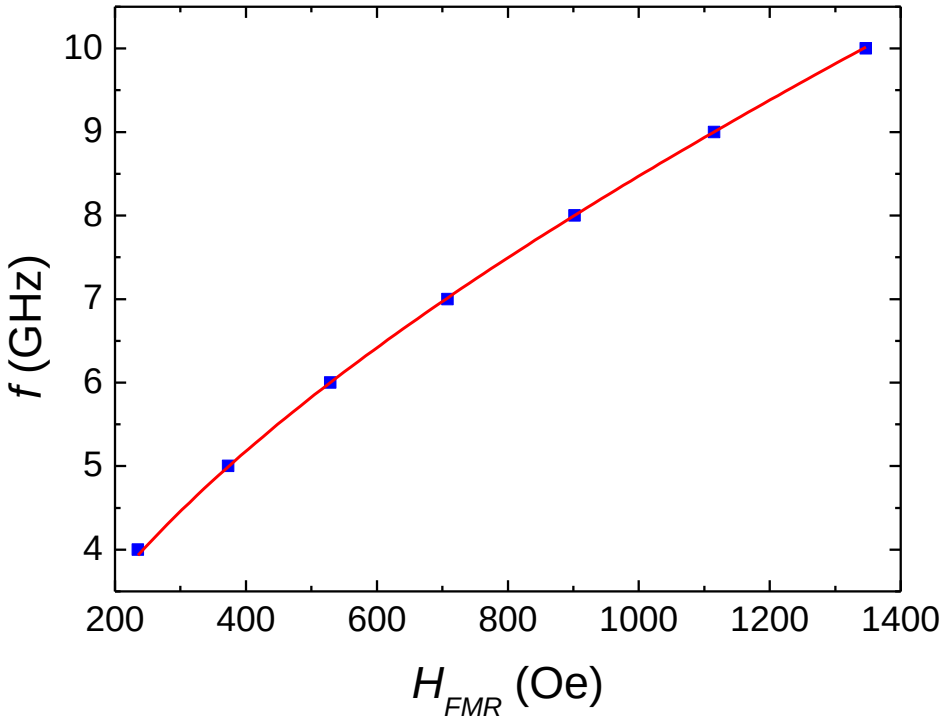

Figure 2-13 Microwave frequency f as a function of resonance field H_{FMR}. The red curve is a fit of the Kittel formula.

We further explore the spin pumping phenomenon by reversing the order of NiFe and Pt layers. In a Pt/NiFe sample, the spin current J_S moves to the opposite direction compared to in NiFe/Pt, while spin polarization direction is kept the same. So, the charge current J_C and the induced DC voltage V are expected to reverse sign. This is observed and shown in Fig. 2-14. On the positive H side, the resonance signal V_{FMR} has a negative sign, which is opposite to that of NiFe/Pt shown in Fig. 2-9. This confirms the ISHE mechanism of the observed voltage in such a spin pumping measurement.

We notice that while V_{FMR} of NiFe/Pt and Pt/NiFe samples have similar magnitude, the step height ΔV of them differ a lot. For the same power $P = 40$ mW, ΔV is

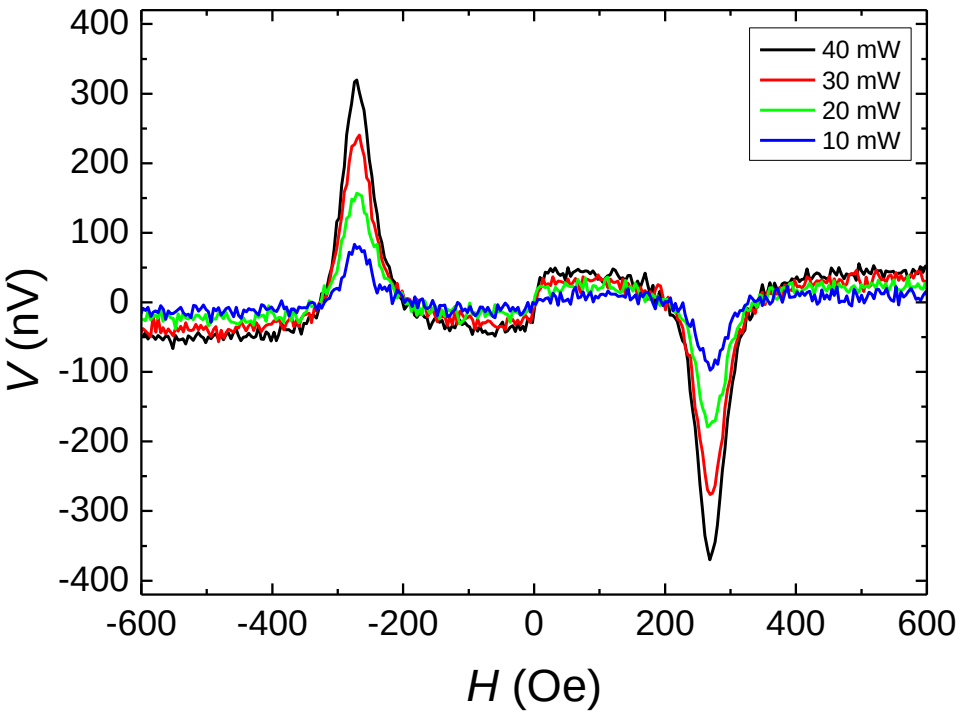

Figure 2-14 Output voltage V from a Pt/NiFe sample for four different microwave power. The microwave has a fixed frequency of 4 GHz.

-700 nV for NiFe/Pt and +80 nV for Pt/NiFe. Also, considering the linear relation of ΔV and microwave power P shown in Fig. 2-11, we come up with an explanation illustrated in Fig. 2-15. When a microwave is applied to the CPW, the AC current I in the signal line will induce a small current, I', in the parallel NiFe/Pt and Pt/NiFe strips. I' mainly distributes in Pt because its conductivity is much larger than NiFe. So, heat is mainly generated in Pt. In NiFe/Pt, heat flows through NiFe down to the substrate, while in Pt/NiFe, most of the heat dissipates directly to the substrate with only a small fraction goes up through NiFe to the air. So, the temperature gradient, ∇T, in NiFe of NiFe/Pt is

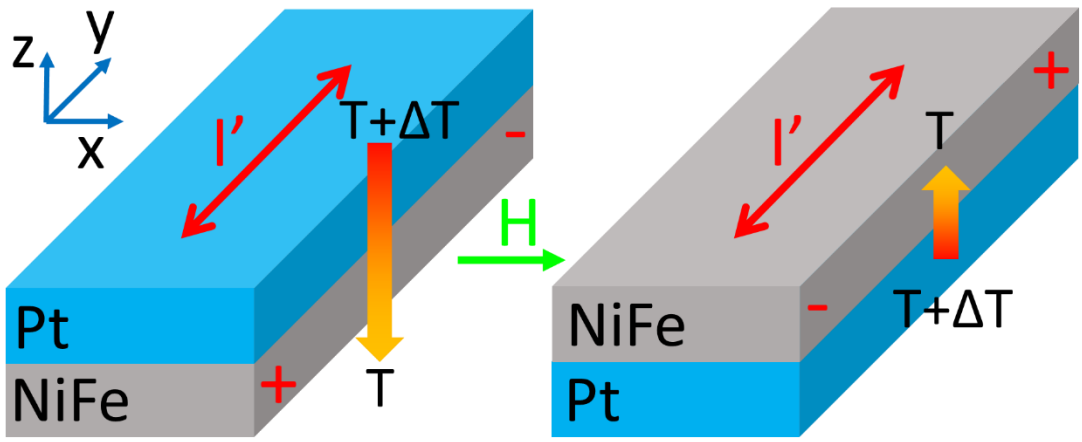

Figure 2-15 Schematic illustration of the voltage step ΔV generated in the NiFe/Pt and Pt/NiFe samples under a microwave. I' is inducted current by the microwave. The heat flow direction in the two geometry are opposite.

much larger than that of Pt/NiFe and they have opposite sign. Due to anomalous Nernst effect (ANE), a Nernst voltage, V_{ANE}, is generated in NiFe. So, the difference of the voltage step height in Fig. 2-9 and Fig. 2-14 can be explained, since $V_{ANE} \propto \hat{\boldsymbol{y}} \cdot (\nabla T \times \hat{\boldsymbol{m}})$, where $\hat{\boldsymbol{y}}$ is the unit vector along the strip, and $\hat{\boldsymbol{m}}$ is the unit vector of the magnetization which reverses direction when H is swept through 0. In principle, the signal we observed should also include a SSE contribution from the Pt layer.

2.3. Heat-driven spin transport in ferromagnetic metal/non-magnetic heavy metal bilayers

2.3.1 Introduction to longitudinal spin Seebeck effect

The spin Seebeck effect (SSE) is a process in which a spin voltage is generated in a magnetic material under a temperature gradient[23]. In a metallic magnet, spin-up and spin-down conduction electrons have different scattering rates and densities. When a temperature gradient is applied to a metallic magnet, it generates different driving force

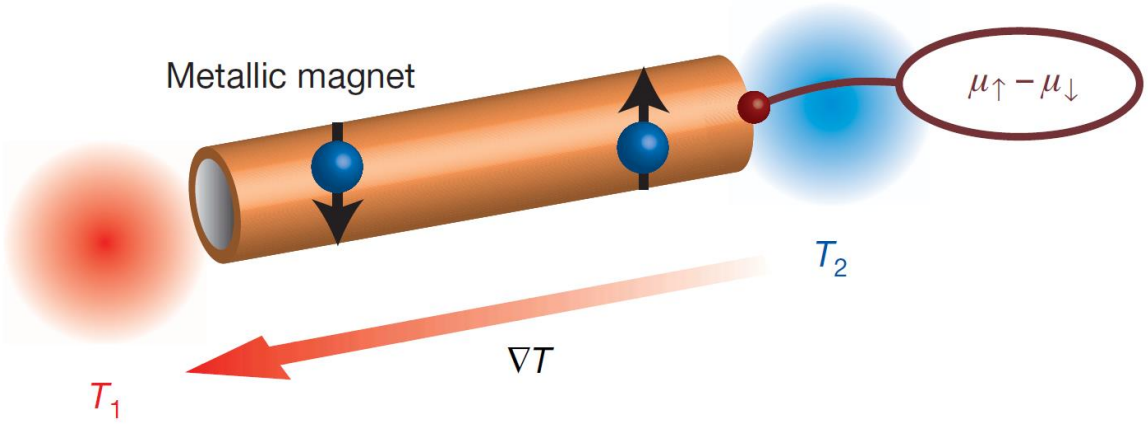

Figure 2-16 Illustration of the spin Seebeck effect in a metallic magnet. $\mu_\uparrow$ and $\mu_\downarrow$ are the electrochemical potentials for spin-up and spin-down electrons. Adapted from Uchida, *et al. Nature*, **455**, 778-781 (2008).

to spin-up and spin-down conduction electrons. Thus, a spin voltage, that is the difference of the electrochemical potentials for spin-up and spin-down electrons, is generated along the temperature gradient direction (Fig. 2-16).

Several experimental setups have been used to observe SSE[27]. In a transverse (conventional) setup (Fig. 2-17(a)), a temperature gradient, ∇T, is applied in the sample plane. A spin current, J_S, is injected upward into a normal metal (NM) strip. It generates an electric filed, E_{ISHE}, in the NM due to ISHE. So, SSE can be demonstrated by measuring E_{ISHE}. As J_S is transverse to ∇T in this measurement, it is called transverse SSE setup. In a longitudinal SSE setup (Fig. 2-17(b), (c) and (d)), the temperature gradient is applied perpendicular to the sample plane. The spin current is in the longitudinal direction of the temperature gradient. The longitudinal SSE setup consisting of a conducting ferromagnet such as NiFe and a non-magnetic heavy metal, has the identical

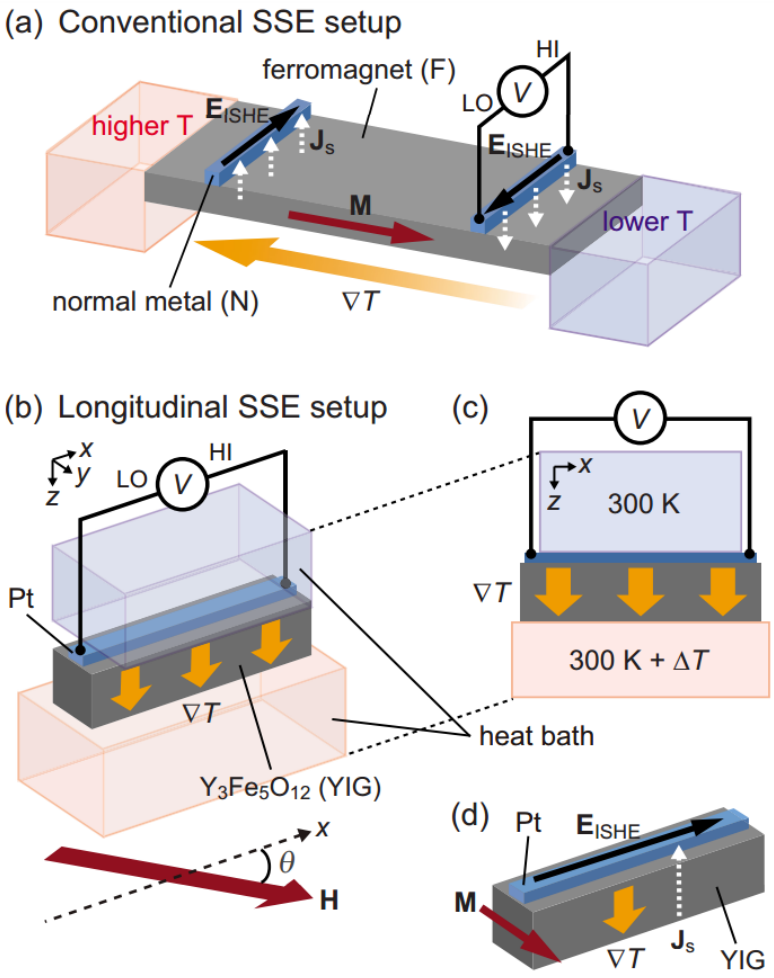

Figure 2-17 Schematics of the conventional (transverse) setup and longitudinal setup for measuring the SSE. Adapted from Uchida *et al. Appl. Phys. Lett*. **97,** 172505 (2010).

geometry for ANE measurement. The SSE is accompanied by ANE in both the ferromagnetic layer NiFe and the proximity-induced boundary layer in the non-magnetic heavy metal. As pointed out by Huang *et al.*[12,28], these two effects can overwhelm the SSE signal which was first reported in NiFe/Pt bilayer[23].

In metallic structures, separating the pure spin current effect from ANE generated by the ferromagnetic metal as well as proximity-induced ANE in the non-magnetic metal remains a serious challenge. Here, we attempt to isolate these effects and quantify the relative contributions in metallic structures.

2.3.2 Device structure and fabrication

Fig. 2-18 shows the device geometry we use for SSE and ANE measurements. We first spin coat a layer of photoresist on a GaAs substrate. A channel (0.2 mm wide and 3.8 mm long) and two side leads are patterned with standard photolithography technique. After manually covering one side leads with a strip of thermal tape, we deposit the metal films by sputtering. After peeling off the thermal tape and covering the other side leads (for electrodes connection purpose), the sample is transferred to an electron beam evaporation system. We consecutively deposit a 300 nm thick Al_2O_3 layer and a 50 nm thick Au layer. The Au layer acts as an electric heater and the Al_2O_3 layer electrically insulates the Au heater from the sample beneath. We put the sample into a beaker of PG remover and keep it on a hot plate for overnight to remove the photoresist. Then, a device with a self-aligned heater on top is left on the substrate. This device structure has a perfect aligned heater which can generates a more uniform and controllable vertical

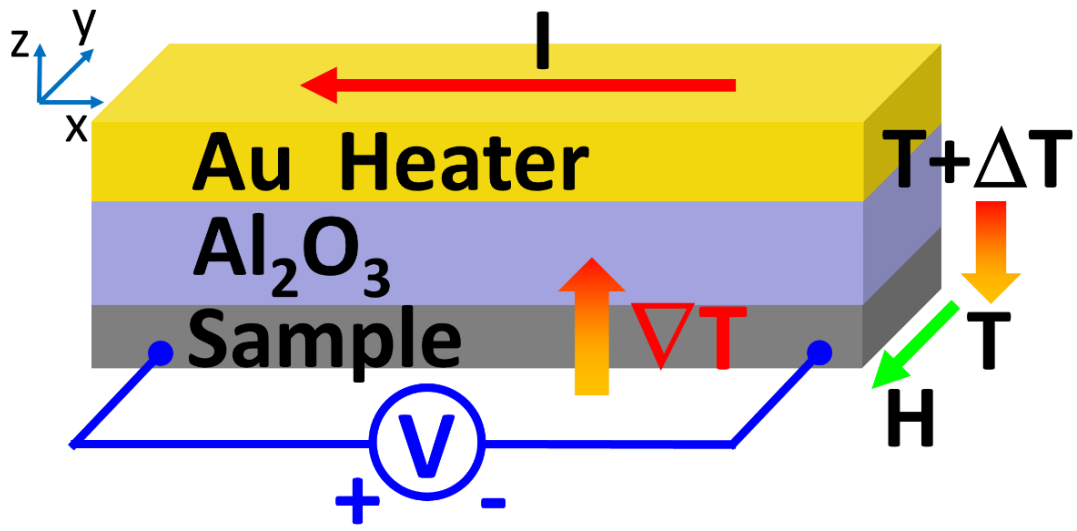

Figure 2-18 Schematic diagram of a device for SSE and ANE measurement. A vertical temperature gradient is generated by an Au heater. The Al_2O_3 insulating layer is 300 nm thick.

temperature gradient, ∇T, which is crucial to our study. Variations in deposition conditions can result in small but discernable variations in the voltage signal even with the same heater power. To avoid the source of this irreproducibility and therefore to resolve small differences in intrinsic properties, we only compare the results from devices that are deposited under the same conditions in one batch.

2.3.3 Anomalous Nernst effect of NiFe only samples

Fig. 2-19 shows two representative voltage hysteresis loops measured across two electrodes from a 15 nm thick NiFe under a vertical ∇T, generated by the same heater power but with opposite polarities in heater current ($\pm$80 mA). An external in-plane

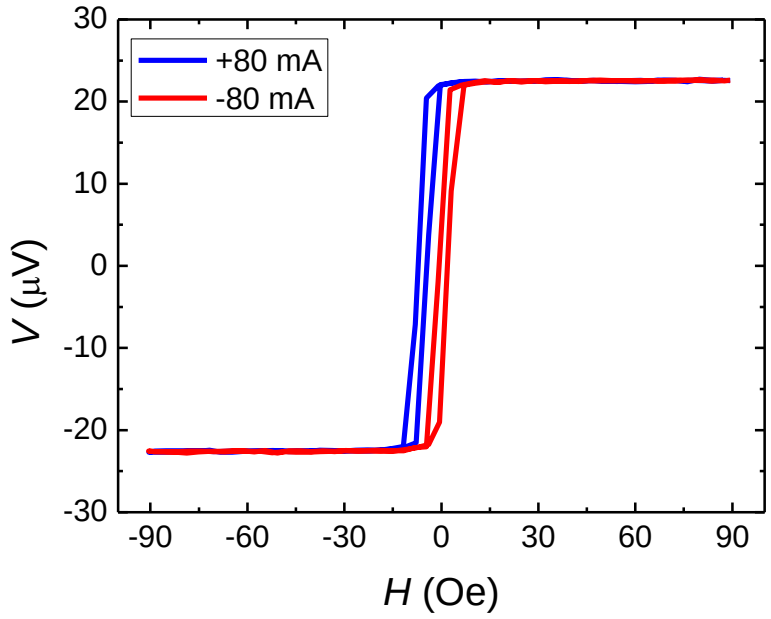

Figure 2-19 Room-temperature voltage loops of a 15nm thick NiFe film for two heater currents ($I = \pm 80$ mA).

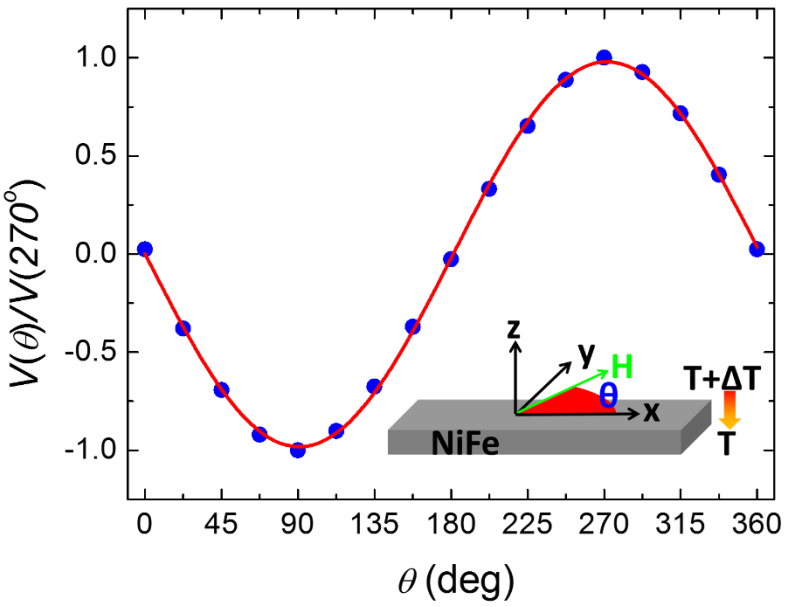

Figure 2-20 Normalized voltage under a 400 Oe in-plane field as a function of rotation angle θ. The red line is a sin θ fit.

magnetic field is swept perpendicular to the channel. The saturation level in both loops is exactly the same, indicating that the sample is well-insulated from the heater. The horizontal loop shift (~ ±3 Oe) is clearly caused by the Oersted field produced by the heater current.

In this geometry, ANE produces voltage hysteresis loops along the channel, since $V_{ANE} \propto \hat{\boldsymbol{x}} \cdot (\nabla T \times \hat{\boldsymbol{m}})$, where $\hat{\boldsymbol{x}}$ is the unit vector along the channel (x-axis), and $\hat{\boldsymbol{m}}$ is the unit vector of the magnetization which reverses the direction with hysteresis under a sweeping magnetic field (y-axis). To further verify the origin of the voltage, we apply a 400 Oe in plane rotating field which fully saturates and rotates the magnetization direction. As the field is rotated, we observe a $\sin\theta$-dependence in the voltage (Fig. 2-20). Furthermore, we find the magnitude of the voltage signal is proportional to the heater power (Fig. 2-21). Fig. 2-21(a) shows voltage loops for various heater currents. In Fig. 2-21(b) we plot the saturation voltage as a function of I^2. The linear relation indicates $V \propto \nabla T$, since I^2 is proportional to the heater power and ∇T. These facts are consistent with the properties of ANE in NiFe.

2.3.4 Spin Seebeck effect and proximity effect in NiFe/Pd

Under a fixed heater power, NiFe simply acts as a voltage source V_N with an internal resistance R_N. When a nonmagnetic layer such as Pd is deposited on top, two things will happen. First, the ANE voltage source will cause a current flow in the non-magnetic layer that reduces the voltage drop when measured in the open-circuit geometry. Second, since Pd has strong spin orbital coupling (SOC), ∇T also drives a

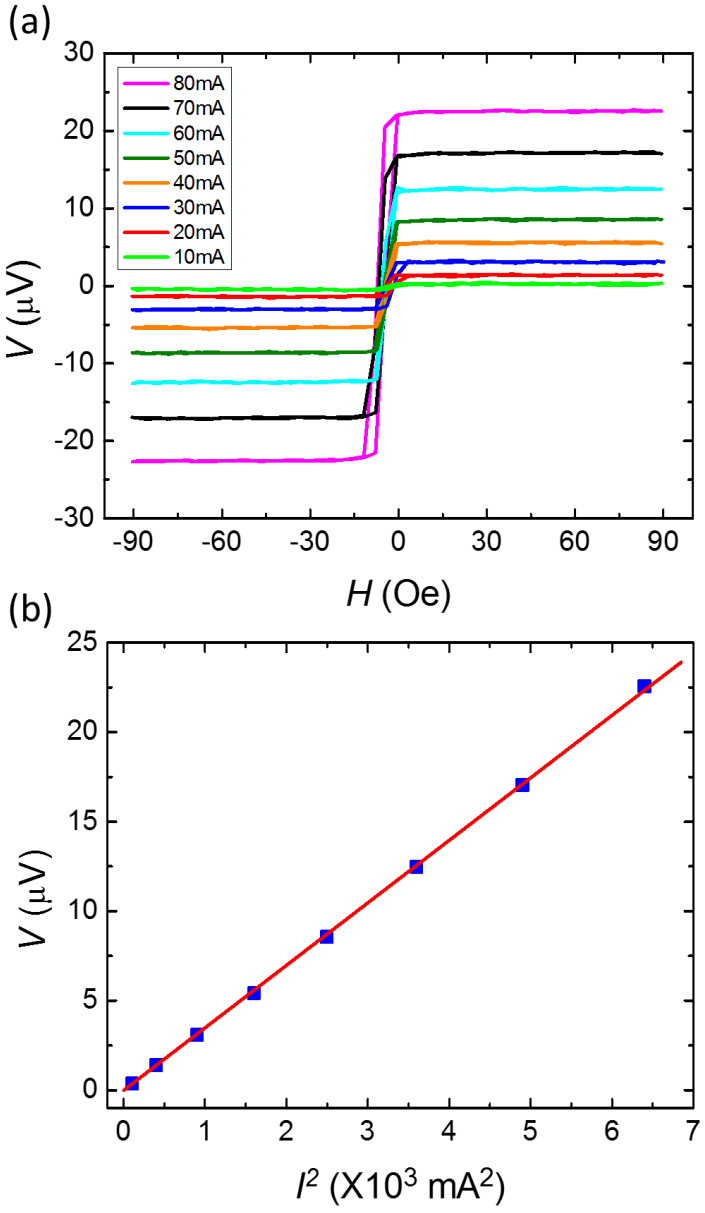

Figure 2-21 (a) Voltage loops for heater currents ranging from 10 to 80 mA. (b) Saturation voltage (half of the difference of voltage at positive and negative field) vs I^2, which is proportional to the heater power. The red line is a linear fit.

vertical spin current, J_S, into Pd which is converted to a charge current J_C due to ISHE. The SSE voltage, V_S, can be written as

$$V_S \propto R_S \theta_{SH} \lambda_S \tanh\left(\frac{t}{2\lambda_S}\right), \tag{2-2}$$

where R_S is the resistance of the SOC layer with thickness t, and θ_{SH} is its spin Hall angle[45]. In the large thickness limit $t > 2\lambda_S$, V_S is simply proportional to R_S, or inversely proportional to the film thickness. To simplify the analysis, we stay in the thick limit for all samples, i.e., V_S/R_S approaching constant. In the meantime, if the Pd is sufficiently thick, we can approximately treat it as an independent layer that is connected in parallel to the NiFe layer. Therefore, in the presence of both ANE and SSE voltage sources, the total measured voltage V is proportional to the total measured resistance R, i.e.,

$$V = \left(\frac{V_N}{R_N} + \frac{V_S}{R_S}\right) R, \tag{2-3}$$

where the first term represents ANE contribution and the second term represents SSE contribution. In our study, the NiFe thickness always keeps constant, so the ANE contribution V_N/R_N does not change. We also keep all Pd layers in the thick limit, so the SSE contribution V_S/R_S is also a constant which is independent of Pd layer thickness. So, if we plot V vs. R for samples with varied Pd thickness, the points should remain on a straight line. And this model also predicts a larger slope in a V vs. R plot for NiFe/Pd samples than a NiFe only sample because of the extra SSE signal.

However, when Pd or other metal with strong SOC is in direct contact with NiFe, the proximity effect will induce magnetic moment inside the SOC metal near the interface. This magnetized thin layer experiences the same ∇T and generates its own

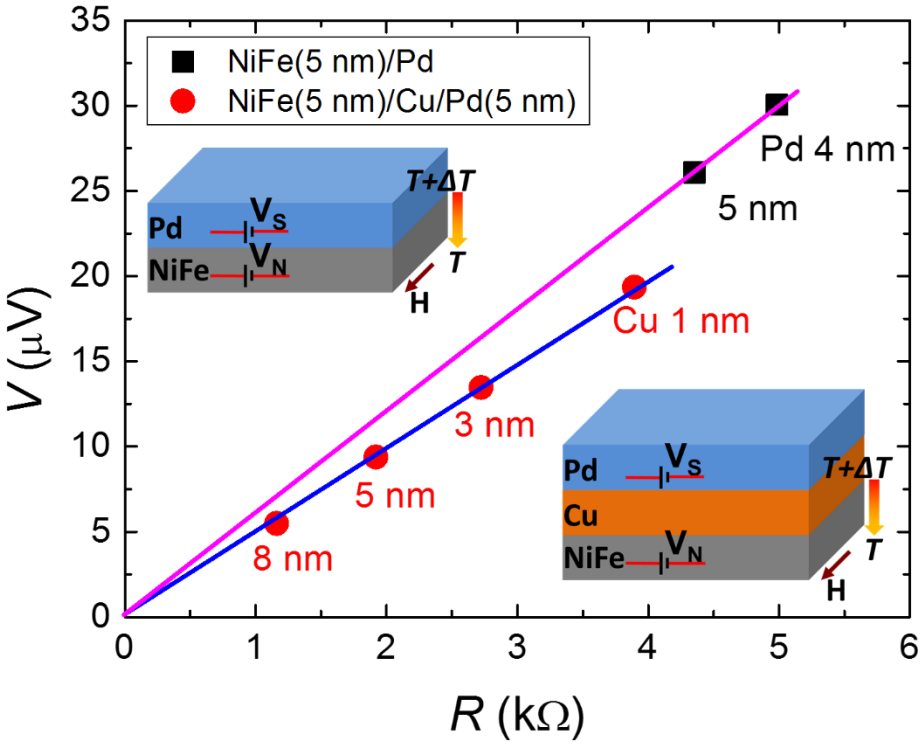

Figure 2-22 Measured total voltage V vs. total resistance R for two sets of samples. The actual resistance of the Au line of a fixed length is measured and V is scaled to exactly the same level of the heater power.

ANE, which is difficult to be separated out and has been a subject of debate[12,46,47]. The presence of this proximity effect is clearly demonstrated in Fig. 2-22. When a Pd layer of different thicknesses (4 and 5 nm) is placed on NiFe, V is indeed directly proportional to R. To remove this proximity effect, we insert a thin layer of Cu between NiFe and Pd. Cu is widely known for its small spin Hall angle and long spin diffusion length (λ_S), so it won't produce measurable voltage due to ISHE or effectively reduce J_S in Pd. In the thick limit, Cu acts as a parallel resistor without voltage output, so Eq. (2-3) also holds for this tri-layer structure. In Fig. 2-22, we show the measured total voltage V vs. total resistance

R for two sets of samples. NiFe thickness is fixed at 5 nm for all samples. For the NiFe/Pd set, Pd thickness is 4 and 5 nm. For the NiFe/Cu/Pd set, Pd thickness is fixed at 5 nm, and Cu thickness ranges from 1 to 8 nm. Clearly, for each set, all data points fall on a straight line. It suggests that the Cu layer in this thickness range works as a load resistor. To check the validity of the parallel resistor model, we plot the total conductance as a function of the Cu thickness and find that the relationship is approximately linear. The thinner Cu (1 nm) shows the largest deviation, indicating a possible breakdown of the model. Although the deviation for thin Cu layers is not obvious in the V vs. R plot, we will draw any conclusion only from the thick Cu layers. Compared with NiFe/Cu/Pd, the slope for NiFe/Pd is larger, which clearly demonstrates the presence of the proximity-induced ANE in Pd. Additionally, the two straight lines do not merge for small Cu thicknesses, suggesting good isolation between NiFe and Pd by the Cu layer. Fig. 2-23 shows the data from devices fabricated in a different batch which further confirms the role of the Cu layer regardless of its position in the structure and the importance of the proximity effect.

2.3.5 Compare SSE in NiFe/Cu/Pd and NiFe/Cu/Ta

In NiFe/Cu/Pd, we believe that the longitudinal SSE contribution from J_S transmitted through the Cu layer is contained in the slope. To further reveal the SSE contribution, we replace the Pd layer by a β-phase Ta layer, another strong SOC metal. It is known that the spin Hall angle θ_{SH} of the β-phase Ta is opposite to that of Pt[34]. To determine the sign of θ_{SH} of Pd relative to Ta, we have prepared YIG/Pd and YIG/Ta

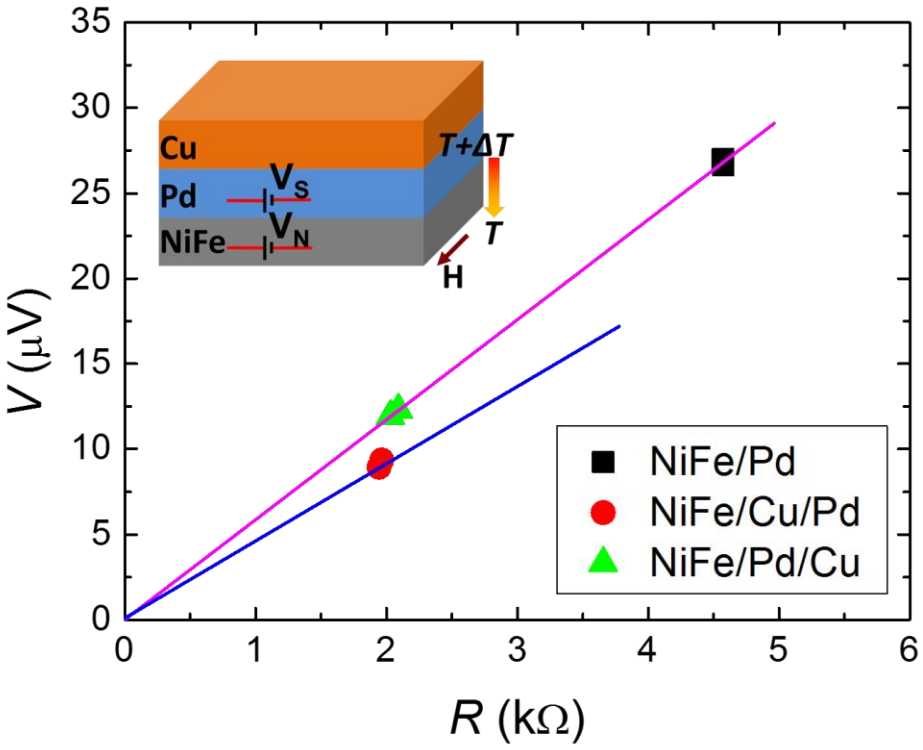

Figure 2-23 *V* vs. *R* for a batch of samples, in which NiFe, Cu and Pd thickness are all fixed at 5 nm. Each structure has two samples.

bilayer structures and conducted longitudinal SSE measurements. Here, the epitaxial YIG film (~50 nm thick) is grown on a gadolinium gallium garnet (110) substrate by pulsed laser deposition[48,49]. The 5 nm thick Pd and 5 nm thick Ta are deposited in different areas of the same YIG film using sputtering. Similar heater structure to Fig. 2-18 is used for the longitudinal SEE measurements. We observe two opposite hysteresis loops in these two devices as shown in Fig. 2-24, indicating opposite signs of θ_{SH} in Pd and Ta.

To focus on the magnitude of the SSE contribution, we compare the results in the following three sets of structures: NiFe(5 nm)/Cu(2 nm)/Pd(t_{Pd}), NiFe (5 nm)/Cu(2 nm)/

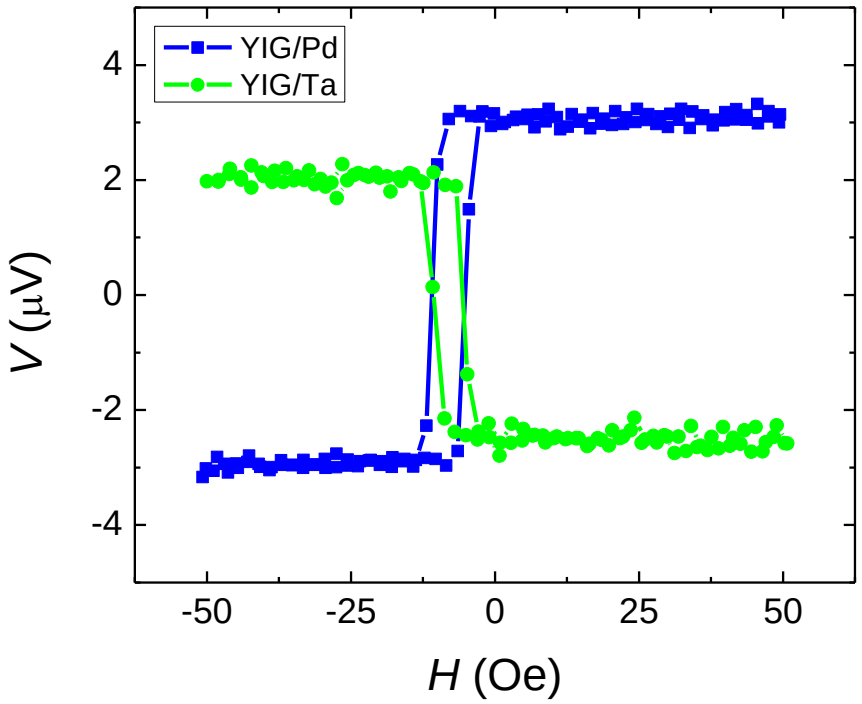

Figure 2-24 Longitudinal SSE voltage loops of YIG-based structures when the same heater power is applied. Pd and Ta layers are 5 nm thick and the devices are fabricated on the same piece of YIG.

Ta(t_{Ta}), and NiFe(5 nm)/Cu(t_{Cu}), all prepared in the same batch to avoid any irreproducibility. In the first two sets, we only vary the thickness of Pd (3-10 nm) or Ta (10-25 nm). The third set serves as a reference that only contains a NiFe ANE voltage source and a variable Cu (2-8 nm) resistor. The first set in Fig. 2-25 (squares) is similar to a set shown in Fig. 2-22 (circles), but the difference is in the actual layer of changing thickness: Pd in Fig. 2-25 but Cu in Fig. 2-22. In both cases, the proximity effect is eliminated by Cu. Despite the differences in thickness, both exhibit excellent linear dependence. Furthermore, even though they are fabricated in two batches, the slopes of the two lines are very close to each other, i.e., 4.92 μV/kΩ and 4.94 μV/kΩ, respectively.

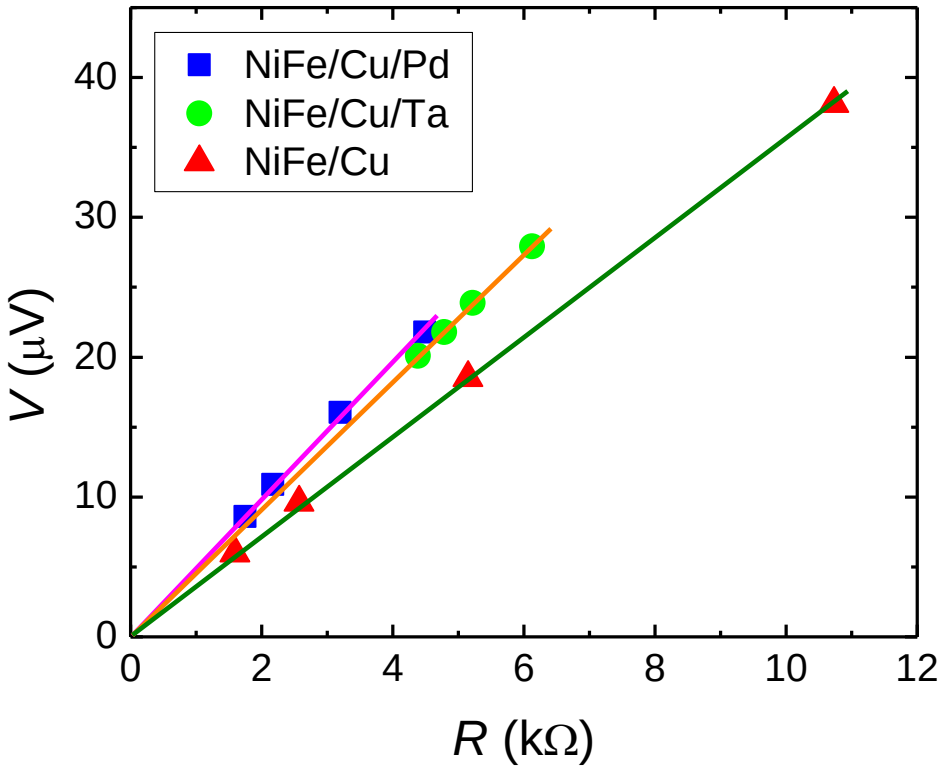

Figure 2-25 Measured *V* vs. the total resistance *R* for three series of samples. NiFe thickness is 5 nm in all samples, and Cu thickness is 2 nm in samples represented by blue squares and green circles. Straight lines are linear fits. NiFe/Cu/Pd and NiFe/Cu/Ta sets have higher slope than NiFe/Cu set.

In the reference set (triangles), the only voltage source is the ANE voltage from the 5 nm thick NiFe, common to other structures. The slope is 3.57 μV/kΩ, clearly smaller than that of the set with varying Pd thickness. When Ta replaces Pd, we expect the straight line to lie below the line for the reference sample set due to the negative SSE signal; however, it stays above that of the reference set. Moreover, the slope of the Ta set (4.57 μV/kΩ) is only slightly smaller than that of the Pd set, which immediately suggests that the SSE contribution is not the primary reason for the slope enhancement observed in

NiFe/Cu/Pd. The fact that both the Pd and Ta samples show significant enhancements relative to the reference indicates another more important mechanism present in both sample sets.

2.3.6 Spin current draining effect and ISHE in NiFe

In the reference samples, i.e., NiFe/Cu, NiFe generates spin accumulation in Cu under a vertical ∇T, but a negligible J_S since Cu has a much longer λ_S than its thickness. However, when a Pd (Ta) layer is placed on top, spin accumulation extends to Pd (Ta) on the scale of its λ_S (~2 nm). It consequently draws a finite J_S in Pd (Ta), which is exactly the source for the longitudinal SSE voltage from the layer. On the other hand, this J_S is continuous in the Cu layer and must extend to NiFe. The additional J_S in NiFe can generate an ISHE voltage by NiFe. The profile of spin-chemical potential, μ_S, can be described by Fig. 2-26. Since J_S is conserved when going through the Cu layer, our experimental results suggest that this additional ISHE voltage converted by NiFe is the main source of the enhanced slope in NiFe/Cu/Pd(Ta).

Now let us estimate the spin Hall angle of NiFe. In the simple current shunting model, the ISHE voltage source contributes to the slope of the straight line by V_S/R_S in Eq. (2-3), as discussed earlier. In fact, the total conductance vs. layer thickness shows excellent linear dependence for both Pd and Ta, justifying the parallel resistor model. Now we have two such terms, one from Pd (Ta) and the other from NiFe. Since R_S for Ta is an order of magnitude larger than that of Pd, the contribution to the slope from Pd is about an order of magnitude larger than that from Ta assuming similar ISHE voltages

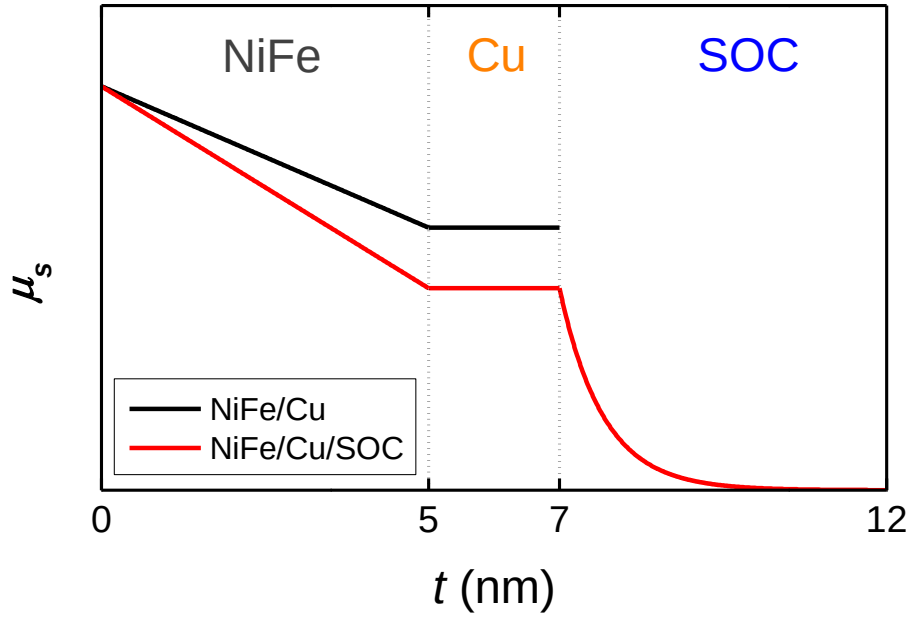

Figure 2-26 Spin-chemical potential, μ_S, in NiFe(5 nm)/Cu(2 nm) and NiFe(5 nm)/Cu(2 nm)/SOC(5 nm), where SOC represents Pd or Ta. The SOC metal behaves as a spin sink in which the spin density drops exponentially, resulting a lower μ_S in Cu. Consequently, inside NiFe, a sharper drop in μ_S creates an extra spin current that results in an ISHE voltage.

from the two. Therefore, if we draw a line to represent the additional ISHE contribution from NiFe, this line would be just slightly above the Ta line. With this new reference line, we can estimate the relative contributions from NiFe and Pd using the slope of these straight lines. The slope difference between the new and old reference lines is identified as V_S/R_S for NiFe due to ISHE in NiFe, which is about 30% of the slope of for the ANE of NiFe. Then the slope difference between the NiFe/Cu/Pd line and the new reference line defines V_S/R_S for Pd. We use Eq. (2-2) to relate V_S from NiFe and Pd to their spin Hall angles and λ_S. We take 2 and 5 nm (Refs. 50 and 51) for λ_S of Pd and NiFe,

respectively, and obtain the lower bound for the ratio of the spin Hall angle between these two materials: $\frac{\theta_{SH}^{NiFe}}{\theta_{SH}^{Pd}} \sim 2.5$.

The presence of an adjacent heavy metal as a spin current drain greatly influences J_S in the ferromagnet of thickness $\sim\lambda_S$, which in turn creates an additional ISHE voltage. A related effect reported by Costache *et al*.[52] also illustrates the importance of the J_S backflow in spin pumping devices. NiFe as an ISHE detector was previously proposed in NiFe/YIG[45], where the spin current effect is superimposed on the intrinsic ANE signal of NiFe. By destroying the spin current effect through Ar-ion beam bombardment or inserting a thin MgO layer in between, the remaining effect was attributed to the intrinsic ANE of NiFe. In our NiFe/Cu/Pd(Ta) devices, the proximity-induced ANE is completely eliminated; therefore, the spin current draining effect due to the SOC metal is unambiguously singled out.

In summary, we demonstrate that in this pure spin current circuit, an additional spin current is drawn by the heavy metal from the ferromagnet. When the relevant dimension of the ferromagnet is comparable with its own λ_S, this spin current generates a significant ISHE signal by the ferromagnetic metal itself, which is superimposed on the ANE signal of the ferromagnet. This effect should be present in all relevant experiments. Analogous to electric circuits, the spin current flow in the pure spin current circuits can be effectively controlled by adjusting its source (temperature gradient in ferromagnet), drain (heavy metals), and channel (light metals). Our results demonstrate the importance of the spin current manipulation in nano-scale devices.

Chapter 3 Interconversion of electronic and magnonic spin currents: magnon-mediated current drag in Pt/yttrium iron garnet/Pt(Ta) trilayers

3.1 Introduction to magnon-mediated current drag

The generation and detection of a pure spin current are usually realized in a bilayers system, which contains a magnetic layer (metal or insulator) and a non-magnetic layer[53–55]. It is very uncommon to achieve the whole process through all electrical methods. Kajiwara *et al.*[31] first demonstrated that an electrical signal can transmit by spin wave in an yttrium iron garnet (YIG) over macroscopic distances (~1 mm) in an all-electrical device (Fig 3-1(a)). The voltage response in the detecting Pt film is very small (~1 nV) and highly nonlinear (Fig 3-1(b)). The driving current density has a threshold,

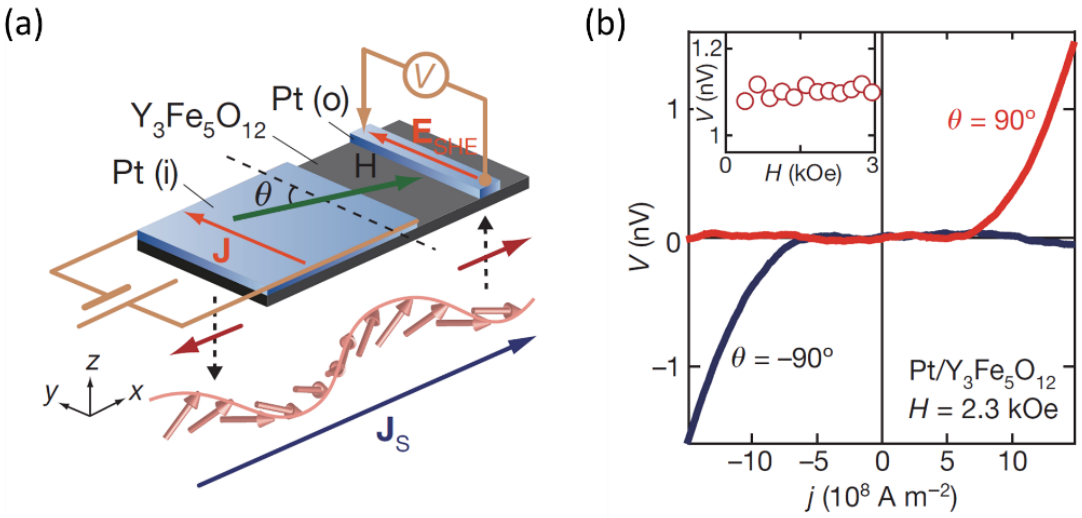

Figure 3-1 (a) A schematic illustration of the measurement setup for electrical signal transmission through spin-wave spin current. The distance between injection and detection Pt strips is 1 mm. (b) *V* vs. the current density, *j*, in the Pt film i at θ=90° and θ=−90°. Adapted from Kajiwara *et al. Nature* **464**, 262-266 (2010).

which was interpreted as the critical point for the spin transfer torque[56,57] to overcome the magnetization damping of YIG. Here, the spin wave inside YIG is a coherent precessing of magnetization. This effect suggests that electronic and magnonic spin currents are interconvertible at the interface of normal metal (NM) and magnetic insulator (MI).

Zhang *et al*.[58,59] proposed a sandwich geometry in which the magnon current flows perpendicular to the plane of the layers with a different origin, analogous to the conventional Coulomb drag effect in 2D electron gases separated by an insulator. Rather than exciting a coherent precession of magnetization (spin wave), the electronic spins in the NM create magnons in the MI. The individual magnon creation doesn't have any threshold; therefore, the conversion takes place at any driving current density. Due to the long magnon decay length in MI, this effect induces an electrical current in a remote metal film, which is called the magnon-mediated current drag. Cornelissen *et al*.[60] reported an AC current measurement in a lateral geometry similar to that of Kajiwara's. They monitor both ω and 2ω nonlocal voltage responses (ω is the frequency of the AC current) and discover that the ω signal has a linear relation to the applied current density, which indicates a different origin to the effect reported by Kajiwara.

We try to experimentally realize the sandwich geometry proposed by Zhang *et al*. and observe the magnon-mediated current drag effect.

3.2 Nonlocal Device structure

Fig. 3-2 schematically shows the NM/MI/NM trilayer device structure. The MI is a thin YIG film that electrically isolates the two NM layers. An in-plane charge current

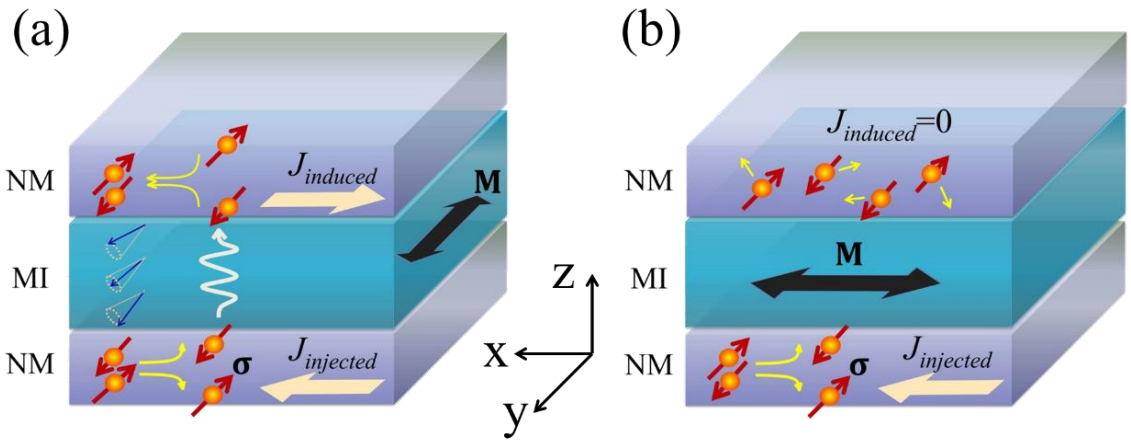

Figure 3-2 Schematic illustration of the magnon-mediated current drag effect. (a) The transmission of spin current is switched on. Magnetization (***M***) of magnetic insulator (MI) oriented collinearly with the spin polarization ***σ***(∥y) of the pure spin current in the bottom normal metal (NM) layer generated by the spin Hall effect with an electric current $J_{injected}$. The spin-flip scattering of conduction electrons at the bottom NM/MI interface can create magnons. A non-equilibrium magnon population extends to the top MI/NM interface, and the spin angular momentum carried by magnons is transferred to conduction electrons in the top NM layer. The pure spin current flowing perpendicular to the NM layer is then converted to a charge current ($J_{induced}$) via the inverse spin Hall effect. (b) The transmission of spin current is switched off. ***M*** is perpendicular to the spin polarization ***σ*** of the spin current. In this geometry, the *s-d* exchange interaction between conduction electrons and local magnetic moments does not excite magnons in the MI. Consequently, there is no spin accumulation at the top MI/NM interface or induced charge current in the top NM layer.

($J_{injected}$) flowing in the bottom NM induces a pure spin current via SHE along z-axis with the spin polarization ($\boldsymbol{\sigma}$) parallel to y-axis. The conduction electrons in the bottom NM couple with the localized moments of the MI via the *s-d* exchange interaction at the interface, creating magnons in the MI with spin-flips of conduction electrons in the bottom NM layer. Due to the nature of the *s-d* exchange interaction[59,61], i.e., $H_{sd} = -J_{sd} \sum \boldsymbol{\sigma} \cdot \boldsymbol{M}$, where J_{sd} is exchange coupling strength, when $\boldsymbol{M}$ is collinear with $\boldsymbol{\sigma}$, magnons are created (Fig. 3-2(a)). The interaction creates a non-equilibrium magnon population in the MI, and the magnons diffuse to the top interface. The excess magnons are then converted to a spin polarization in the top NM layer by the reverse process. The diffusion of the electronic spin is converted to a charge current ($J_{induced}$) again in the top NM layer via the ISHE. When $\boldsymbol{\sigma} \perp \boldsymbol{M}$, there is no non-equilibrium magnon population and the spin current is absorbed by the MI. Consequently, there is no induced spin or charge current in the top NM layer (Fig. 3-2(b)). The magnon creation process can be switched on and off by controlling the relative orientation of $\boldsymbol{M}$ and $\boldsymbol{\sigma}$. This structure can be used as a valve for pure spin current.

3.3 Device fabrication

We first spin coat a layer of photoresist on a (110)-oriented single crystalline $Gd_3Ga_5O_{12}$ (GGG) substrate and then use standard photolithography to pattern a Hall bar with the channel width of 20 μm and the distance between two electrodes of 300 μm. Then the bottom Pt layer is deposited on the patterned Hall bar area by DC magnetron sputtering. During sputtering, argon pressure is 5 mTorr, substrate temperature is 300 K,

and the DC sputtering power is 37.5 W. The deposition rate of Pt is 0.77 Å s^{-1} and the Pt layer thickness is 5 nm. After lift-off, an 80 nm thick YIG film is deposited at 450℃ with O_2 pressure of 1.5 mTorr in a pulsed laser deposition system to cover the entire surface of the sample. The as-grown YIG film becomes crystallized and magnetized after rapid thermal annealing between 800 and 850 ℃ for 200 s. To develop the right recipe, we have explored a range of growth temperatures, different annealing conditions, various pulsed laser deposition rates and YIG film thicknesses. Many difficulties appear, such as YIG film cracking, thicker YIG films peeling off, current leaking, no magnetization and so on, before we obtain the suitable method. Fig. 3-3 shows the magnetization hysteresis loops of an unpatterned GGG/Pt(5 nm)/YIG(80 nm) sample characterized by vibrating sample magnetometer (VSM). The surface morphology of YIG film grown on Pt is monitored by atomic force microscopy. As shown in Fig. 3-4(a), the YIG surface is very flat with clear atomic terraces. The root-mean-square roughness on the terraces is ~0.14 nm. We use standard e-beam lithography to define the top Pt and Ta patterns right on top of the bottom Pt Hall bar channel. The sample is then transferred into the sputtering system. A 60 s Ar ion milling is performed to remove any organic resist residues from the patterned area and then the Pt (or Ta) is deposited on top. The deposition conditions for top Pt and Ta are the same as those for bottom Pt. The top Pt and Ta strips are 2 μm in width, and 90 and 60 μm in length, respectively. After the nonlocal measurements, we deposit a 300 nm thick Al_2O_3 layer and a Cr (5 nm)/Au (50 nm) heater on top of the devices, to generate a vertical temperature gradient for a separate longitudinal SSE measurement.

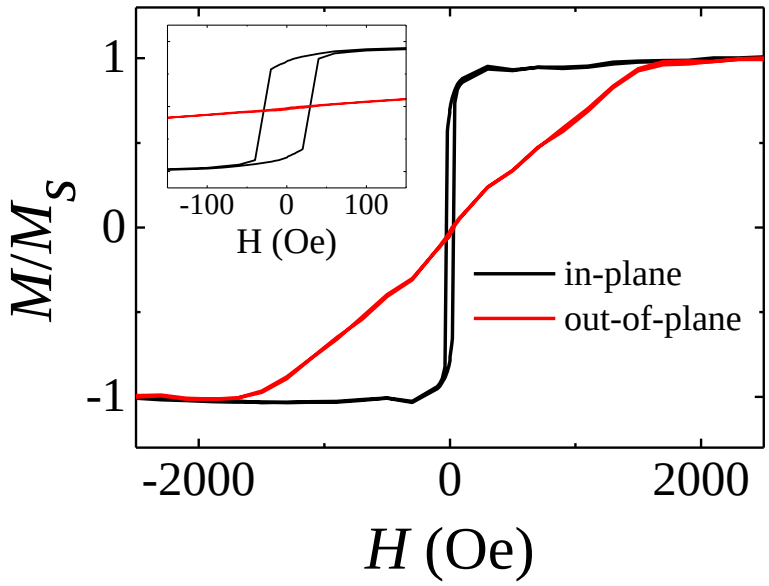

Figure 3-3 Magnetic property of a YIG film. Room temperature magnetic hysteresis loops of an unpatterned GGG/Pt(5 nm)/YIG(80 nm) film measured by vibrating sample magnetometry (VSM). Inset shows the zoom-in low field hysteresis loops.

3.4 Transport measurement

For all transport measurements, we use a Keithley 2400 current source to apply DC current and a Keithley 2182A nano-voltmeter to measure voltage signal. The magnetic field dependence measurements are performed with a closed-cycle refrigerator system, while the angular dependent measurements are carried using a physical property measurement system equipped with a rotatory sample holder. For the nonlocal measurements, the applied current in the bottom Pt is no more than 2 mA; for the local magnetoresistance measurements, the current applied in top Pt and Ta is 1 μA, while the current in bottom Pt is 10 μA. For the SSE measurements, the heating current applied in the top Au layer is 30 mA. In all the measurements, we pay extra attention to ensure correct polarity of the currents and voltages.

3.5 Field-dependent nonlocal response in trilayer devices

As both Pt and Ta have strong spin-orbit coupling with opposite signs in their spin Hall angle[19,62,63], we have fabricated three Pt (5 nm)/YIG (80 nm)/Pt (5 nm) devices and two Pt (5 nm)/YIG (80 nm)/Ta (5 nm) reference samples. The inset of Fig. 3-4(c) shows an optical image for a GGG/Pt/YIG/Pt device. As illustrated in Fig. 3-4(b), the bottom Pt layer is used to inject a current I_b, while the top layer, either Pt or Ta, measures the induced current or the nonlocal voltage V_{nl}. An in-plane H is either swept in a fixed direction or rotated with an angle θ with respect to y-axis. We find that the high-quality YIG/Pt interface is essential to the observation of the spin current transmission. As shown in Fig. 3-4(a), the morphology of a YIG film tracks the atomically flat terraces of the GGG (110) surface[49] despite a layer of Pt in between. The 80 nm thick YIG films are nearly insulating but have small leakage at high temperature. However, the resistance between top and bottom NM layers increases exponentially as the temperature decreases, and exceeds 20 GΩ at and below 220 K. Therefore, we perform all the nonlocal measurements below 220 K to avoid any spurious signal from the small leaking current. In V_{nl}, we remove a non-zero background signal that exists even at $I_b = 0$. Fig. 3-4(c), (d) show the field dependence of V_{nl} at 220 K. When H is swept along I_b, i.e., $\theta = 90°$ (Fig. 3-4(c)), V_{nl} is a constant at $I_b = 0$ (red). At $I_b = +1.5$ mA, V_{nl} shows a clear hysteresis with two positive peaks tracking the coercive fields of the YIG film, indicating that V_{nl} is closely related to the magnetization state of YIG. As I_b is reversed, V_{nl} also reverses sign. In principle, a sign reversal can occur if there is a finite leaking current flowing in the top layer. Through the magnetoresistance, this current can produce a hysteretic voltage

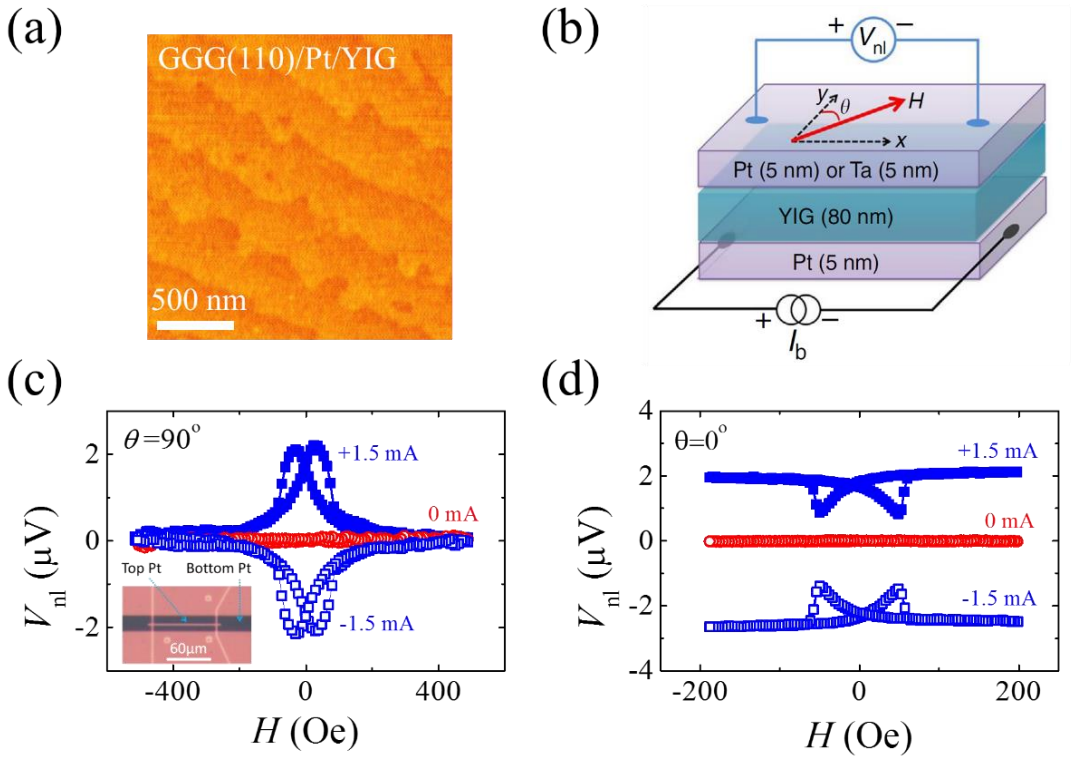

Figure 3-4 Measurement geometry and field dependent nonlocal signal. (a) Atomic force microscopy image of an 80 nm YIG film grown on a 5 nm Pt. (b) Schematic illustration of the experimental set-up. I_b is the current applied to the bottom Pt layer, and V_{nl} is the nonlocal voltage measured at the top layer along the I_b direction. The applied in plane magnetic field H makes an angle θ with the y-axis which is in plane and perpendicular to the current direction (x-axis). (c) The field dependence of the nonlocal signal for H along I_b, i.e., θ =90°. The inset shows the optical image of the GGG/Pt/YIG/Pt device. (d) The field dependent nonlocal signal with H perpendicular to I_b, i.e., θ =0°. In both (c) and (d), solid (empty) blue squares and empty red circles represent V_{nl} for +1.5 mA (−1.5 mA) and 0 mA bottom current, respectively.

signal. Estimating from the leaking current, we find that the relative change in V_{nl} due to this effect is at least three orders of magnitude smaller than the observed nonlocal voltage signal. Therefore, we exclude the leaking current as the source of the nonlocal signal. Note that V_{nl} ($\pm$1.5 mA) is the same as V_{nl} (0 mA) at the saturation state ($H > 200$ Oe) when $\boldsymbol{\sigma} \perp \boldsymbol{M}$, suggesting that magnon creation is totally suppressed. For the field swept with $\theta = 0°$ (Fig. 3-4(d)), $\boldsymbol{\sigma}$ is collinear with $\boldsymbol{M}$ at high fields, so interface magnon creation results in a full current drag signal. Clearly, V_{nl} ($+$1.5 mA) is different from V_{nl} (0 mA) at the saturation fields and reverses sign when I_b reverses. It is interesting to note that V_{nl} ($\pm$1.5 mA) differ from V_{nl} (0 mA) at the coercive fields. One would expect them to be the same since the average magnetization should point along the x-axis at the coercive fields, which would correspond to the saturation states for $\theta = 90°$ in Fig. 3-4(c). This discrepancy can be explained by the multi-domain state of YIG in which the actual $\boldsymbol{M}$ is distributed over a range of angles around $\theta = 90°$, and the collinear components of $\boldsymbol{M}$ turn on the magnon channel and result in a nonzero V_{nl}. To investigate the phenomenon in the single domain state, we perform the following experiments.

3.6 Angle dependent nonlocal response of single domain YIG

Fig. 3-5(a) shows V_{nl} in GGG/Pt/YIG/Pt as a function of θ between $\boldsymbol{M}$ and $\boldsymbol{\sigma}$ at 220 K, as illustrated in Fig. 3-4(b). The 80 nm (110)-oriented YIG grown on Pt has a well-defined uniaxial anisotropy with an anisotropy field <200 Oe. The applied magnetic field (1,000 Oe) is sufficiently strong not only to set YIG into a single domain state, but also to rotate $\boldsymbol{M}$ with it. For all positive I_b (solid symbols), V_{nl} exhibits maximum at

$\theta = 0°$ and 180° ($\boldsymbol{M}$ collinear with $\boldsymbol{\sigma}$), and minimum at $\theta = 90°$ and 270° ($\boldsymbol{M} \perp \boldsymbol{\sigma}$). V_{nl} changes sign as I_b is reversed (empty symbols). At $\theta = 90°$ and 270°, the nonlocal signal for $\pm I_b$ coincides with V_{nl} (0 mA), further confirming that the spin current is in the off state when $\boldsymbol{M} \perp \boldsymbol{\sigma}$. Similar angular dependent measurements are also performed on a GGG/Pt/YIG/Ta device and the results are plotted in Fig. 3-5(d). For the same measurement geometry and the same polarity of I_b, we find that V_{nl} of GGG/Pt/YIG/Ta has opposite sign to that of GGG/Pt/YIG/Pt, which is just expected from the opposite sign of their spin Hall angle. The V_{nl} sign difference here is another important evidence for the magnon mediated mechanism, rather than for other extrinsic ones such as current leakage.

We notice an interesting feature that V_{nl} at $\theta = 0°$ and 180° show a small but reproducible difference that is independent of the current polarity but increases with the magnitude of I_b. We attribute this phenomenon to the SSE contribution since the joule heating in the bottom Pt layer unavoidably generates a small vertical temperature gradient, which drives an upward spin current from YIG to the top Pt (or Ta) layer. As $\boldsymbol{M}$ reverses, so does the spin polarization, which consequently produces two different SSE signal levels at $\theta = 0°$ and 180°. Combining these two effects, we can fit the angular dependence data using:

$$V_{nl} = V_0 + V_{SSE}\cos\theta + V_{Drag}\cos^2\theta, \tag{3-1}$$

where V_0 is an offset voltage not dependent on the magnetization direction, V_{SSE} represents the SSE voltage amplitude and V_{Drag} is the amplitude of the current drag signal. The solid red curves in Fig. 3-5(a), (d) fit the experimental data remarkably well,

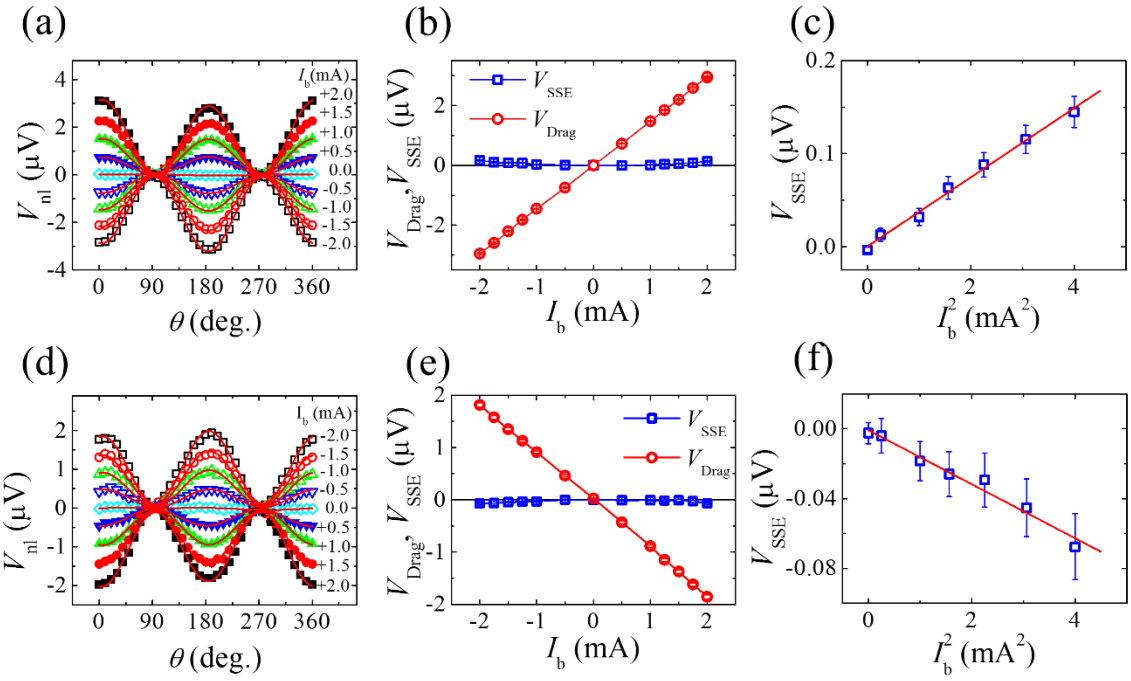

Figure 3-5 Angular and current dependence of nonlocal signal. ((a), (d)) Angular dependence of nonlocal signal at different currents in the bottom Pt layer for GGG/Pt/YIG/Pt and GGG/Pt/YIG/Ta, respectively. The magnetic field is fixed at 1,000 Oe and rotated in plane. In (a) and (d), solid symbols indicate positive I_b, and empty symbols indicate negative I_b. The red curves are least squares fits using Eq. (3-1). ((b), (e)) The I_b dependence of the current drag signal (V_{Drag}) and the spin Seebeck signal (V_{SSE}) for GGG/Pt/YIG/Pt and GGG/Pt/YIG/Ta, respectively. (c, f) The spin Seebeck signal as a function of I_b^2 for GGG/Pt/YIG/Pt and GGG/Pt/YIG/Ta, respectively. The red curves are the linear fits. The error bars are from fitting using Eq. (3-1) in (a) and (d).

and the extracted fitting results are plotted in Fig. 3-5(b), (e) for GGG/Pt/YIG/Pt and GGG/Pt/YIG/Ta devices, respectively. We can draw two conclusions from these results. First, the magnitude of the current drag signal (red circles) scales linearly with the driving current, i.e., $V_{\mathrm{Drag}} \propto I_{\mathrm{b}}$. This is in sharp contrast to the highly nonlinear behavior in Kajiwara's experiment[31]. Second, the SSE contribution has weak current dependence and follows $V_{\mathrm{SSE}} \sim I_{\mathrm{b}}^2$ (as shown in Fig. 3-5(c), (f)), which is a characteristic of thermoelectric effects. Compared with YIG/Pt bilayers, trilayer structures may have an enhanced SSE signal due to the presence of the second heavy metal layer which draws an extra spin current. Carefully designed experiments are needed to demonstrate this effect.

3.7 Temperature dependence of nonlocal responses

According to Zhang *et al.*[59], the temperature dependence of the spin convertance at the injection interface (G_{em}) is $\left(\frac{T}{T_{\mathrm{c}}}\right)^{3/2}$, where T_{c} is the Curie temperature of the MI; the spin convertance at the detection interface (G_{me}) is proportional to $\frac{T}{T_{\mathrm{F}}}$, where T_{F} is the Fermi temperature of the NM layer. In the most simplified scheme, which is applicable only for very thick films, the current drag signal should be proportional to the product of the two spin convertances, i.e., $V_{\mathrm{Drag}} \propto G_{\mathrm{em}} \cdot G_{\mathrm{me}} \propto T^{5/2}$. The representative angular dependence signal for temperatures at and below 220 K are shown in Fig. 3-6(a), (c) for GGG/Pt/YIG/Pt and GGG/Pt/YIG/Ta devices, respectively. For both the samples, I_{b} is fixed at $+2$ mA and H is held at 1,000 Oe. The magnitude of the current drag signal gradually decreases with temperature for both the devices. By fitting V_{nl} with Eq. (3-1),

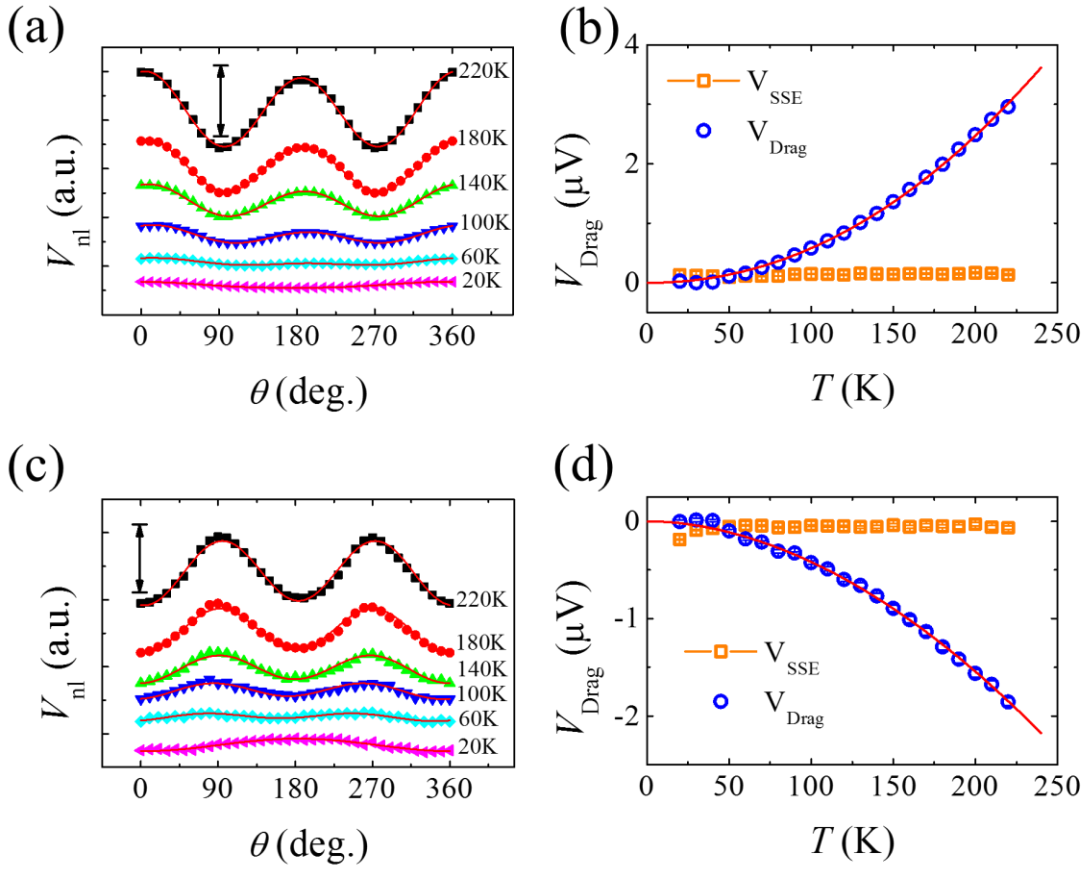

Figure 3-6 Temperature dependence of nonlocal signal. (a), (c) Angular dependence of the nonlocal signal at different temperatures for GGG/Pt/YIG/Pt and GGG/Pt/YIG/Ta, respectively. For all the measurements, I_b is fixed at +2 mA. The curves are vertically shifted for clarity, the black arrows in (a) and (c) represent the magnitude scale of 2.80 and 1.98 μV, respectively. Red solid curves in (a) and (c) are the fits using equation (3-1). (b), (d) The temperature dependence of the extracted current drag signal (V_{Drag}) and spin Seebeck signal (V_{SSE}) for GGG/Pt/YIG/Pt and GGG/Pt/YIG/Ta, respectively. Red solid curves in (b) and (d) are the fits using $V_{Drag} = V_{Drag}^{0} T^{n}$, here, n = 2.21 for the GGG/Pt/YIG/Pt device, and n = 1.88 for the GGG/Pt/YIG/Ta device.

the magnitude of V_{Drag} and V_{SSE} are extracted and plotted in Fig. 3-6(b), (d). Besides the expected difference of sign, the magnitude of V_{Drag} in both devices monotonically decreases with temperature. In fact, both data sets can be well fitted by a power-law $V_{\mathrm{Drag}} = V_{\mathrm{Drag}}^{0} T^{n}$ (red solid curves in Fig. 3-6(b), (d)), where V_{Drag}^{0} is a pre-factor. The extracted exponent *n* is 2.21 for GGG/Pt/YIG/Pt and 1.88 for GGG/Pt/YIG/Ta. It should be emphasized that the full picture described by Zhang *et al.*[59] contains other quantities that have weak temperature dependence. The deviation of the exponents from 2.5 is fully expected considering these factors. However, the V_{SSE} is found to have very weak dependence on temperature, suggesting a totally different mechanism.

3.8 Leakage test of the sandwich device

In the sandwich structures, we measured the resistance between top and bottom NM at different temperatures. As illustrated in the inset of Fig. 3-7, we measured the resistance by applying a voltage between the top and bottom NMs and detecting the leaking current as a function of temperature. The applied bias voltage must be adjusted in different temperature ranges because of the dramatic resistance change. The junction resistance increases rapidly with decreasing *T* and exceeds 20 GΩ for $T \leq 220$ K, which is larger than the input impedance of the nano-voltmeter (> 10 GΩ for Keithley 2182A), indicating that the leaking current produces a negligible voltage change in the top NM layer via the magnetoresistance during the nonlocal measurements. In Fig. 3-7, we show the resistance vs. 1/*T* on a semi-log plot for a constant bias voltage. It clearly shows an activated behavior with an effective barrier height of 0.42 eV for this temperature range.

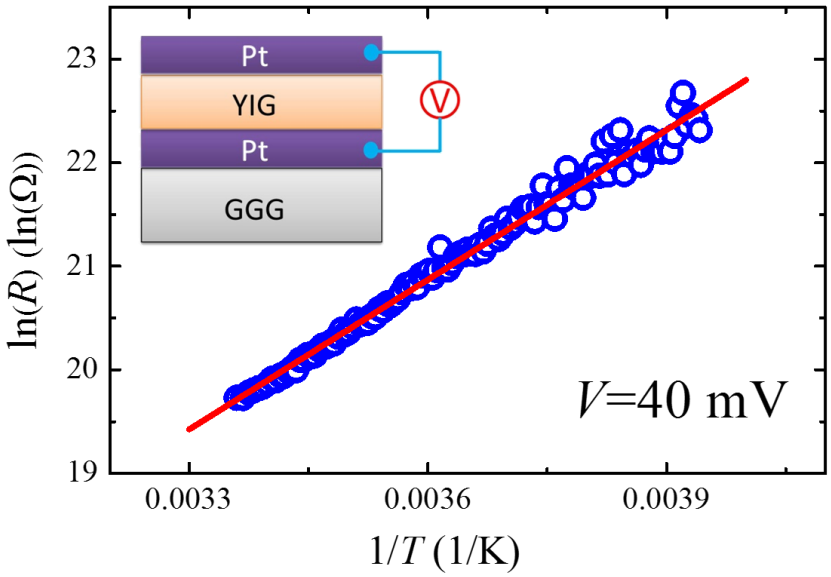

Figure 3-7 Leakage test of the device. Resistance between the top and bottom Pt layers vs. $1/T$ for a fixed bias voltage of 40 mV as shown in the inset. The thickness of YIG is 80 nm. The temperature range is from 300 to 250 K, in which the corresponding resistance increases from 0.3 to 6 GΩ. The redline is a fit which gives an effective barrier height of 0.42 eV over this temperature range. Below this temperature range, the resistance keeps increasing exponentially, but the voltage must be adjusted to higher values, which results in a slightly different barrier height due to some bias voltage dependence.

For different bias voltages, the extracted barrier height varies. This effective barrier height is much smaller than the band gap of an ideal YIG. We know that the YIG film is uniform in thickness and atomically flat. In addition, the film is insulating laterally. We believe that the observed activated behavior could be due to microscopic regions with relatively lower energy barriers. As the temperature is lowered, the whole film becomes highly insulating.

3.9 Spin Hall magnetoresistance of normal metal layers

Spin Hall magnetoresistance (SMR) is a unique transport phenomenon in a NM which is in direct contact with a MI[13]. A charge current flowing in the NM with strong spin-orbit coupling is converted to a spin current via SHE. The reflection and absorption of this spin current at the interface of the NM/MI depends on the orientation of the magnetization ($\boldsymbol{M}$) of the MI. When $\boldsymbol{M}$ is collinear to the spin polarization $\boldsymbol{\sigma}$, most of the spin current is reflected; in contrast, when $\boldsymbol{M}$ is perpendicular to $\boldsymbol{\sigma}$, most of the spin current is absorbed by the insulator. The absorption behaves as a dissipation channel; therefore, the resistance of the NM is larger than that for $\boldsymbol{M} \parallel \boldsymbol{\sigma}$. Thus, the degree of reflection or absorption of the spin current at the NM/MI interface can be monitored by SMR. To characterize the quality of the interface in the sandwich device, we perform the MR measurements. As illustrated in Fig. 3-8(a), we carry out local MR measurements by applying a magnetic field (1,000 Oe) in the film plane at an angle θ with the y-axis, while the current flows along the x-axis. The angular dependence of the MR ratios for top Pt, top Ta, and bottom Pt at room temperature are summarized in Fig. 3-8(b). According to the SMR theory[64], the longitudinal resistivity has the form

$$\rho = \rho_0 + \rho_1 m_y^2, \tag{3-2}$$

where ρ_0 is a constant insensitive to the magnetization orientation, ρ_1 represents the SMR magnitude which depends on film thickness, spin Hall angle and spin diffusion length of the NM, and interface spin-mixing conductance; and m_y is the y component of the magnetization unit vector. As shown by the red solid curves in Fig. 3-8(b), the experimental data can be well fitted by Eq. (3-2). Besides SMR, the induced

magnetization in the NM due to the magnetic proximity effect (MPE)[12,65,66] can also generate similar MR. The MPE induced MR should increase monotonically with decreasing temperature[66], since both the induced magnetic moment and the spin diffusion length increase at low temperatures. However, SMR has a broad peak as a function of temperature[49]. To better understand the nature of the MR we observed, we perform the temperature dependent measurements, and the results are summarized in Fig. 3-8(c). For both top Pt and Ta, the MR ratio has a broad peak, as expected from the SMR theory, suggesting the SMR mechanism dominates the transport property of the top NM. However, the MR ratio of the bottom Pt is one order smaller than that of the top Pt and is relatively insensitive to temperature. Recently, Goennenwein *et al*.[67] reported a monotonically decreasing SMR signal with temperature. Those results suggest that the temperature dependence of SMR may be very sensitive to the interface quality. The lack of clear temperature dependence of SMR in the bottom Pt can be attributed to the less ideal quality of the bottom interface, possibly due to oxidation occurred in rapid thermal annealing at high temperature. Based on the temperature dependence of the MR results, we demonstrate that the SMR mechanism dominates in our devices. Therefore, the anisotropic reflection and absorption of the spin current at the YIG/NM interfaces indicate excellent interface quality for spin currents interconversion.

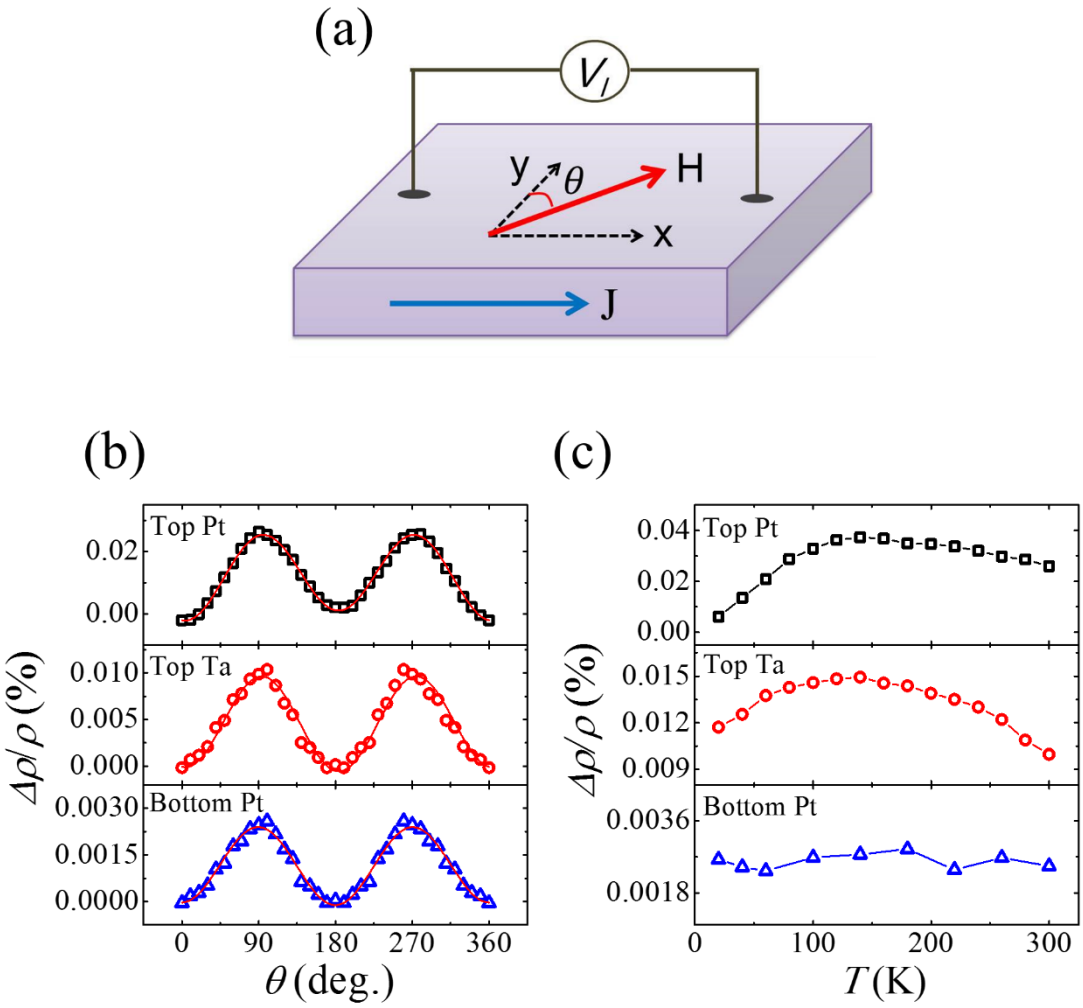

Figure 3-8 Spin Hall magnetoresistance of normal metal. (a) Schematic illustration of local MR measurement geometry. A magnetic field is applied in the film plane at an angle θ with the y-axis. (b) Room-temperature angular dependence of the MR in the top Pt, top Ta, and bottom Pt layers with a magnetic field of 1,000 Oe. Continuous red curves are the fitting results using Eq. (3-2). (c) Temperature dependence of the MR ratio for the top and bottom NM.

3.10 Nonlocal current drag signal versus local MR signal

Here, we demonstrate that the nonlocal voltage we observed in sandwich structures cannot be produced by a local SMR signal of the top Pt due to the leaking current. Fig. 3-9(a), (c) show the field dependence of the raw nonlocal signal in the Pt/YIG/Pt sandwich structure and that of the resistivity of the top Pt layer, respectively. For the nonlocal signal, V_{nl} for zero bottom current is constant which defines a reference. V_{nl} for $+1.5$ mA (-1.5 mA) shows clear hysteresis behavior and reaches the minimum (maximum) values around the coercivity field of YIG. The relative change of the nonlocal signal, $\left(\frac{V(I)-V(0)}{|V(0)|}\right)_{\mathrm{nl}} = \left(\frac{\Delta V}{V}\right)_{\mathrm{nl}}$, is shown in Fig. 3-9(b), where $V(0)$ is the nonlocal signal in the absence of the bottom current. In contrast, we show the MR ratio of the top Pt in the same device in Fig. 3-9(d). Remarkably, the magnitude of $\left(\frac{\Delta V}{V}\right)_{\mathrm{nl}}$ at 1.5 mA (~20%) is about four orders of magnitude larger than that of the MR ratio in the top Pt layer (~0.02%). Similar conclusion can also be obtained from the angular dependence of both the nonlocal signal and local MR of the top Pt layer, as shown in Fig. 3-10. The $\left(\frac{\Delta V}{V}\right)_{\mathrm{nl}}$ at 2.0 mA (~240%) is almost five order larger than MR ratio in the top Pt (~0.03%). The above comparison between the nonlocal voltage signal and the local MR signal in the top Pt strongly suggests that the nonlocal signal can't come from the SMR effect of the top layer due to the leaking current.

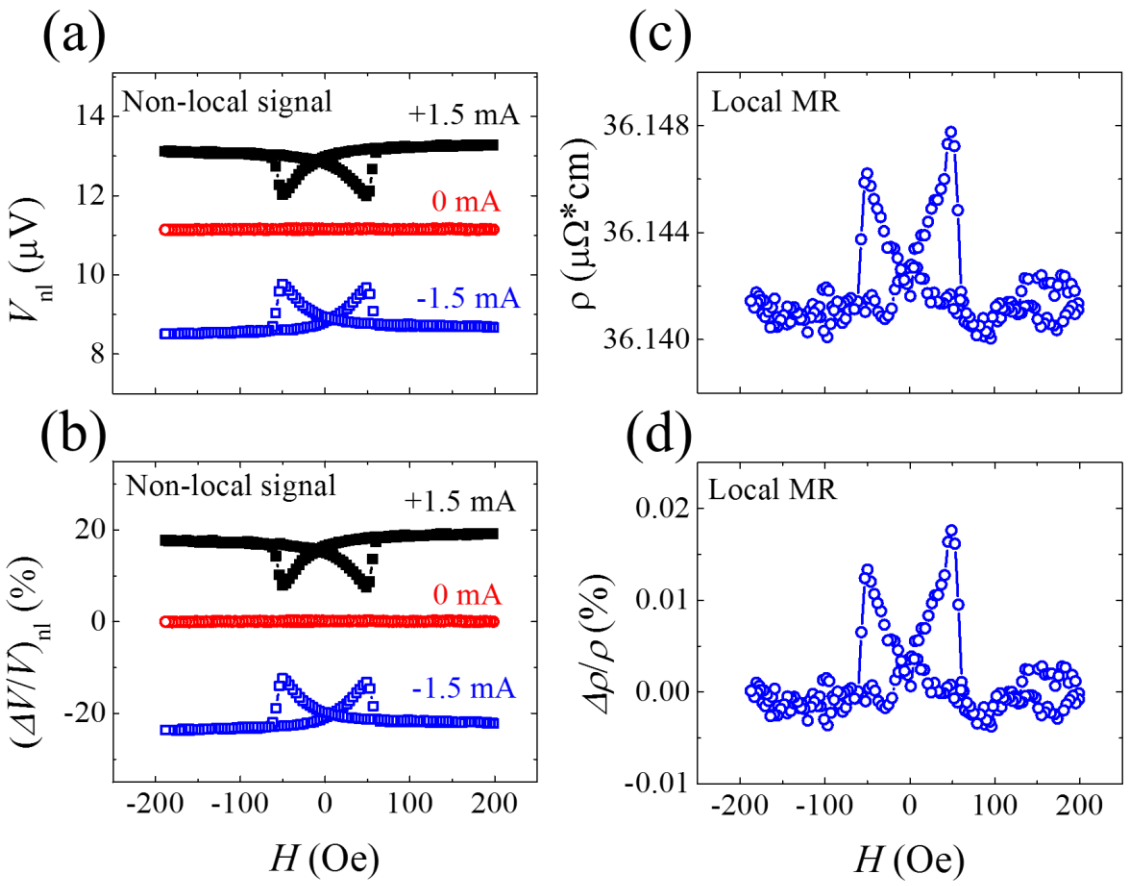

Figure 3-9 Field-dependent nonlocal and local signals. (a) and (b) are raw nonlocal data and the relative change of the nonlocal signal with respect to V_{nl} (0 mA), respectively, in Pt/YIG/Pt device at 220 K; black, red, and blue symbols represents V_{nl} for the bottom layer current of +1.5 mA, 0 mA and −1.5 mA. (c) and (d) are the local resistivity and MR ratio for the top Pt layer in Pt/YIG/Pt device at 220 K.

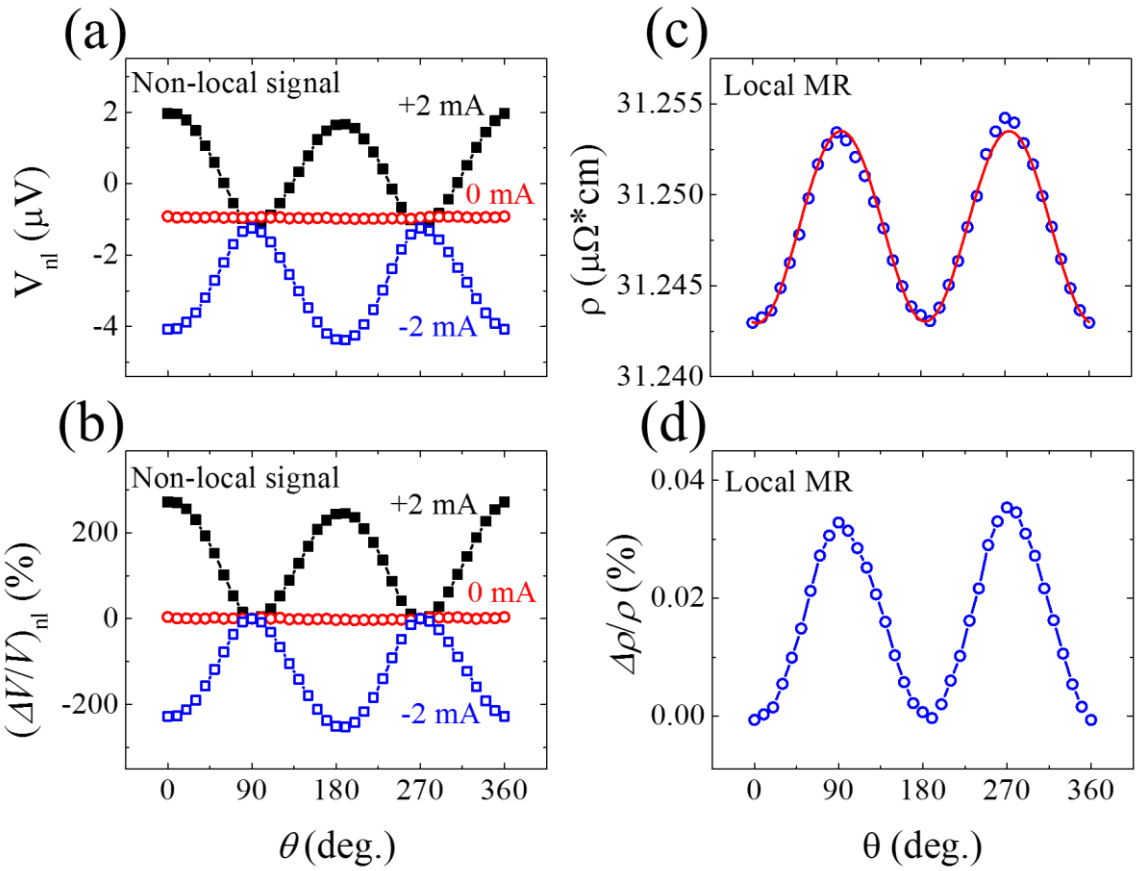

Figure 3-10 Angular dependence of nonlocal and local signals. (a) and (b) are the raw nonlocal signal and the relative change of the nonlocal signal with respect to V_{nl} (0 mA), respectively, in Pt/YIG/Pt device at 220 K; black, red and blue symbols represent V_{nl} with the bottom current of +2 mA, 0 mA, and −2 mA. (c) and (d) are the local resistivity and the MR ratio for the top Pt layer in Pt/YIG/Pt device at 220 K. The red solid curve in (c) is the fitting result using Eq. (3-2).

3.11 Longitudinal spin Seebeck effect

We confirm the transmission of thermally excited spin currents through the YIG/NM interface by performing the longitudinal SSE in our sandwich structures. On top of the sandwich structures, we deposit a 300 nm thick Al_2O_3 layer and a heater consists of 5 nm Cr and 50 nm Au. When a charge current (30 mA) is applied to the Cr/Au layer, a temperature gradient is established along the z-axis by joule heating, as shown in Fig. 3-11(a). During the SSE measurements, a magnetic field is swept along y-axis while the voltages along x-axis are monitored. In Fig. 3-11(b), we plot the field dependence of the longitudinal SSE signal at 220 K, which is normalized to the device length. First, all three metal layers show strong SSE signal. Second, we find that the magnitude of the SSE

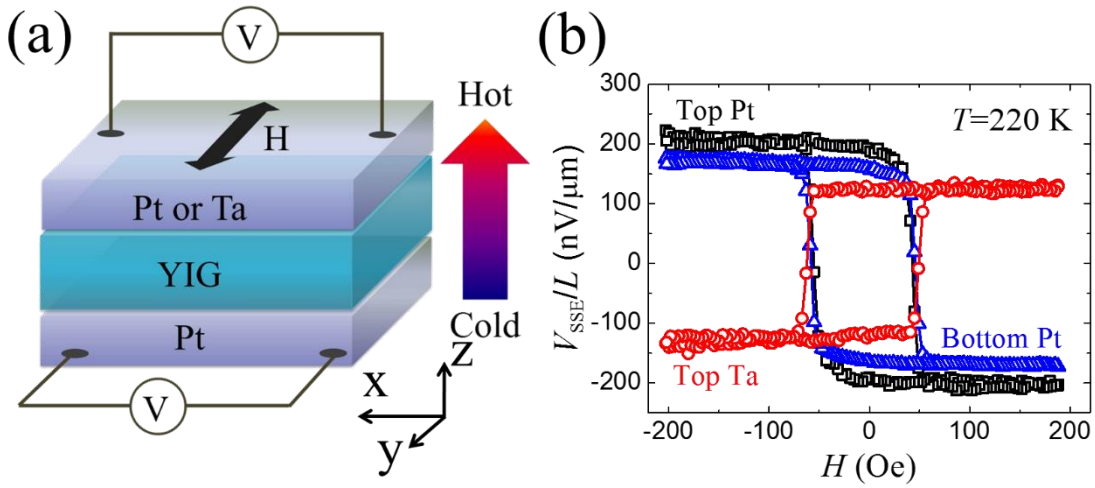

Figure 3-11 Longitudinal spin Seebeck effect in sandwich devices. (a) Schematic illustration of the longitudinal spin Seebeck effect measurement setup. A temperature gradient is generated along z-axis by a heater on top. Voltages of the top and bottom layers are measured along x-axis with the magnetic field sweeping along y-axis. (b) SSE signals divided by the detecting stripe length L as a function of the magnetic field at T =220 K, for top Pt, top Ta, and bottom Pt.

signal from bottom Pt is on the same order of that from top Pt, which is different from the SMR results shown in Fig. 3-8(c). The different behavior of SMR and SSE signals indicates that the interface change has different effect on the anisotropic reflection (or absorption) of a spin current due to spin transfer torque, and on the transmission of thermally excited spin current. Third, we notice that the SSE signal from the top Ta shows opposite sign to that from Pt, which is expected since Pt and Ta have opposite spin Hall angles. Therefore, we have confirmed the excellent interface quality for transmitting thermally excited spin currents.

3.12 Summary

We have achieved electronic and magnonic spin currents interconversion at the metal and magnetic insulator interfaces by demonstrating the magnon-mediated current drag effect in NM/MI/NM trilayer structures. Such structures have potential application as spin valves since the spin current can be switched on/off by rotating the in-plane magnetization of the MI by 90°. Furthermore, such structures also provide analogue functionality since rotating the in-plane magnetization of the MI provides analogue sinusoidal modulation of the spin current. Due to the extremely low damping in the MI, transmission of the pure spin currents can occur over relatively long distances, so these structures can also be used as pure spin interconnects.

Chapter 4 Spin to charge conversion in YIG/topological insulator heterostructures

4.1 Introduction to topological insulators

Topological insulators (TIs) are a new type of electronic materials that have a bulk band gap, which means its interior is insulating like an ordinary insulator, but possess gapless edge or surface states which are protected by time-reversal symmetry[68,69]. For a three-dimensional (3D) TI, in the topologically nontrivial phase, the bulk states are fully gapped, while the surface states have a single Dirac cone. The surface states with a single Dirac cone is observed by angle-resolved photoemission spectroscopy (ARPES) in 3D topological insulators[70–72].

Due to strong spin-momentum coupling, the conducting electrons of the surface states have a spin-momentum locking character. The electron spin direction and its motion direction are perpendicular to each other. As shown in Fig. 4-1, at the Fermi level, electrons moving in $+\mathrm{x}$ direction have spin pointing to $+\mathrm{y}$ (or $-\mathrm{y}$) direction, and electrons moving in $-\mathrm{x}$ direction have spin pointing to $-\mathrm{y}$ (or $+\mathrm{y}$) direction, depending on the Fermi level position relative to the Dirac point. If a spin imbalance is generated in the surface state, a charge current $\boldsymbol{J_C}$ will be induced along the direction defined by $\boldsymbol{J_C} \parallel (\hat{\boldsymbol{z}} \times \boldsymbol{\sigma})$, where $\boldsymbol{\sigma}$ is the direction of the spin polarization and $\hat{\boldsymbol{z}}$ is the unit vector perpendicular to the surface plane[73]. Unlike the 3D nature of the ISHE, where the spin-charge conversion happens within a finite depth of the SOC material, the 2D character of surface state in TI determines that the spins cannot diffuse into bulk, but convert to a charge current only on the sample surface. Thus, the efficiency of spin-charge conversion could be very high on the surface of a good bulk insulating TI sample.

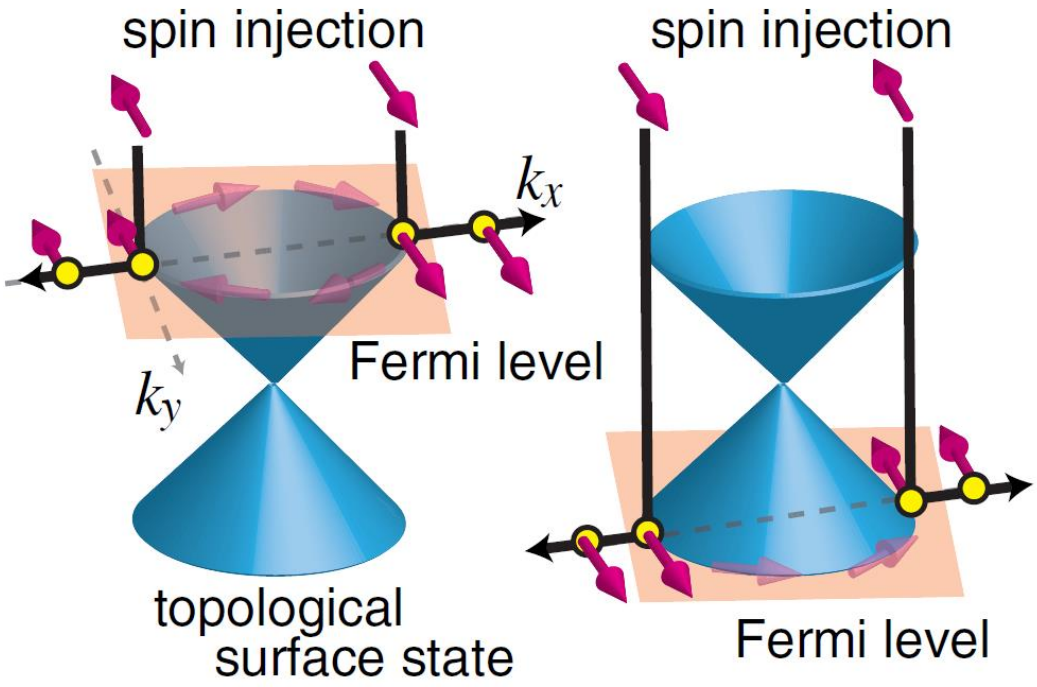

Figure 4-1 Schematic illustrations of spin-charge conversion effects on the spin-momentum locked surface state of a topological insulator. Adapted from Shiomi *et al*. *Phys. Rev. Lett*. **113**, 196601 (2014).

The helical spin texture of TI surface state has attracted high research interests recently. It has been demonstrated in spin transport experiments, including spin-torque FMR[74–76], spin pumping effect[73,77–79], magnetic tunnel junction[80], spin valve device[81–84] and spin-torque induced magnetization switching[85,86], that spin-charge conversion efficiency in TI surface state is one to two orders higher than heavy metals.

Although TIs are believed to offer an obvious advantage over traditional conductors in generating and detecting pure spin current according to those experiments, several fundamental important questions are still not fully understood. In most of the experiments, the bulk of TI are not perfectly insulating due to a metallic bulk conduction

channel or unavoidable doping from crystalline defects. The observed large spin torques and spin-charge conversion signals in the ferromagnet/TI heterostructures could also come from the bulk states, besides the spin textured surface states, because usually the TI bulk states also possess strong SOC. In a structure TI and ferromagnet have direct contact, the surface states of TI will be changed by the magnet through band bending, and the surface of TI can be magnetized through the magnetic proximity effect[87–89]. Proper experiments are needed to address these important questions for further TI spintronics study.

4.2 Topological spin Seebeck effect

SSE is an effective heat driven pure spin current generation method which has been widely utilized in ferromagnet/heavy metal bilayers. The efficiency of spin detection in TI topological surface states has not been demonstrated in a heat driven magnon transport measurement. In this work, we try to establish the topological SSE, which combines the ease of magnon generation of SSE and the efficient spin detection of TI surface states. In a SSE device consisting a ferromagnetic metal, it is hard to avoid an ANE effect that results from the flow of spin-polarized electrons inside the ferromagnetic metal. To exclude the ANE induced voltage signal from our measurement, we choose YIG, an insulating ferrimagnet, as the source of magnons. In the longitudinal SSE configuration, a vertical temperature gradient drives magnons to flow towards the YIG/TI interface. In the steady state, the excess magnons are balanced by decay via magnon-phonon scattering inside YIG or by interactions of magnons with electrons near the Fermi

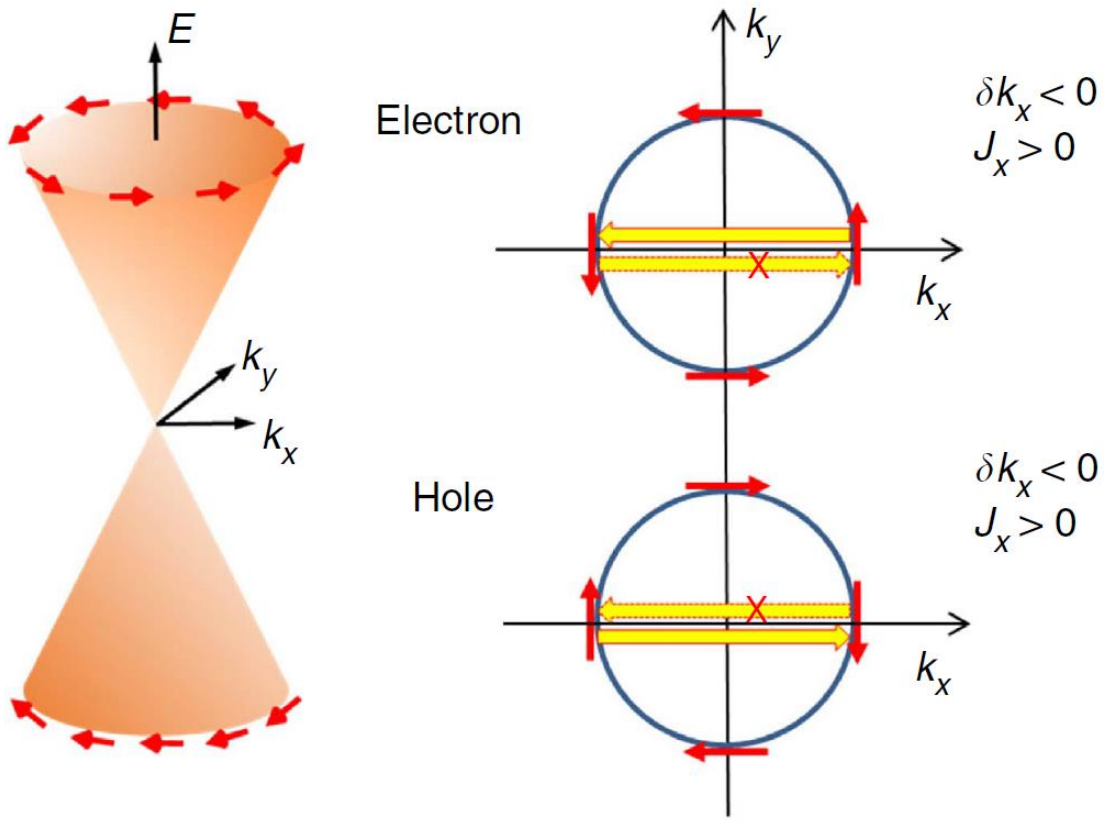

Figure 4-2 Schematic illustration of magnon induced spin flips of electrons and holes in topological surface states. Magnon relaxation on TI surface generates charge currents of the same sign for n type or p type charge carriers in the surface states.

energy of the TI. When this magnon-electron interaction decay channel is made active by tuning TI Fermi level into the bulk band gap, a large electromotive force emerges in the direction perpendicular to the in-plane magnetization of YIG.

Fig. 4-2 is a schematic illustration of magnon induced electron spin flips in topological surface states. Assuming YIG and TI surface states have isotropic exchange interactions, when a magnon is annihilated, an electron flips from majority to minority spin-orientation to conserve the total spin. When the YIG magnetization is in the y-direction, spin-momentum locking induces electrons in the conduction band near the Fermi surface moving from k_x to $-k_x$ direction but not from $-k_x$ to k_x, resulting in a net flow of electrons along $-k_x$ or a positive current J_x. While in the valence band, magnon annihilation induces a positive momentum transfer δk_x to holes, through which holes are scattered from $-k_x$ to k_x. As a result, the induced J_x is also positive. Thus, magnon relaxation in TI surface generates charge currents of the same sign for n type or p type charge carriers in the surface states.

4.3 YIG/TI heterojunction preparation and longitudinal SSE geometry

We grow 20 nm thick YIG films on gadolinium gallium garnet (GGG) (111) substrates by pulsed laser deposition (PLD) at ~700 ℃ as reported previously[48,49,87,90]. Fig. 4-3 is an atomic force microscopy image of a representative YIG sample. It has an atomically flat surface with a root mean square roughness around 0.12 nm. The GGG/YIG sample is then transferred into an ultrahigh vacuum molecular beam epitaxy (MBE) system. It is first annealed at 600 ℃ for 30 min, then a 5 quintuple layer (QL)

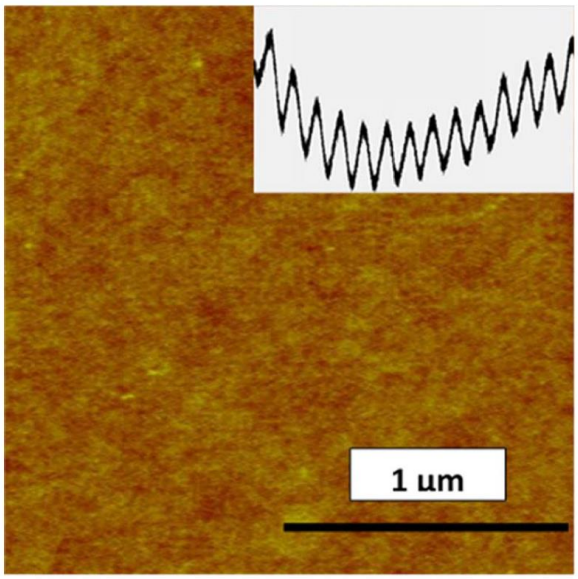

Figure 4-3 Atomic force microscopy image of a representative GGG(111)/YIG sample. The inset shows the RHEED intensity oscillations during YIG growth, which indicates the atomic layer-by-layer deposition.

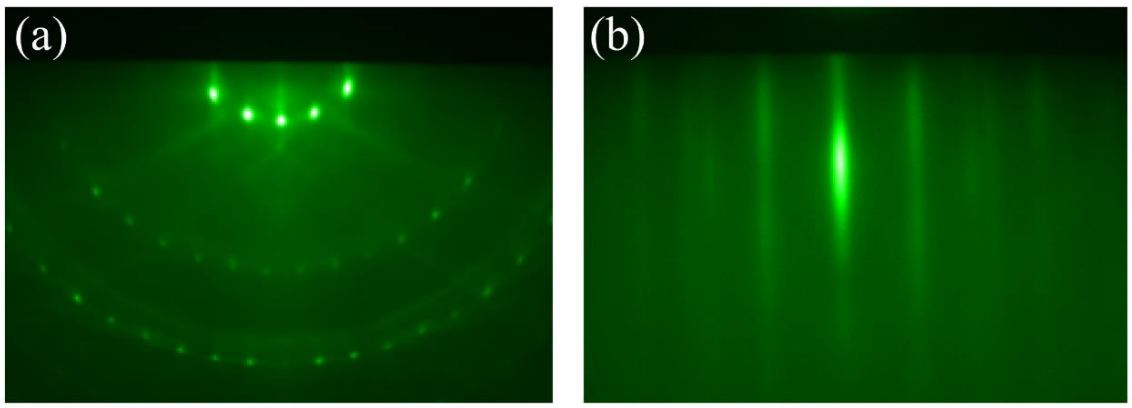

Figure 4-4 RHEED patterns of YIG and TI film. (a) RHEED pattern taken on YIG in the MBE chamber before TI growth. (b) RHEED pattern of a 5 QL $(Bi_{0.24}Sb_{0.76})Te_3$ film grown on YIG.

thick $(Bi_xSb_{1-x})_2Te_3$ film is grown on top at ~250℃ followed by a 5 nm thick Te capping layer. $(Bi_xSb_{1-x})_2Te_3$ is a 3D TI in which the Fermi level can be tuned between valence and conduction bands by changing Bi/Sb ratio[91]. Fig. 4-4 shows reflection high-energy electron diffraction (RHEED) patterns of a sample before and after TI growth. The sharp and streaky pattern indicates its high crystalline quality and very flat surface.

As shown in Fig. 4-5, the YIG/TI heterostructure is patterned into a 100 μm wide, 900 μm long Hall bar with standard photolithography and Ar plasma etching. The resist baking temperature is 110 ℃ and the Ar plasma etching time is divided into several 1-min sessions to avoid overheating, which could degrade the TI film quality. Metal

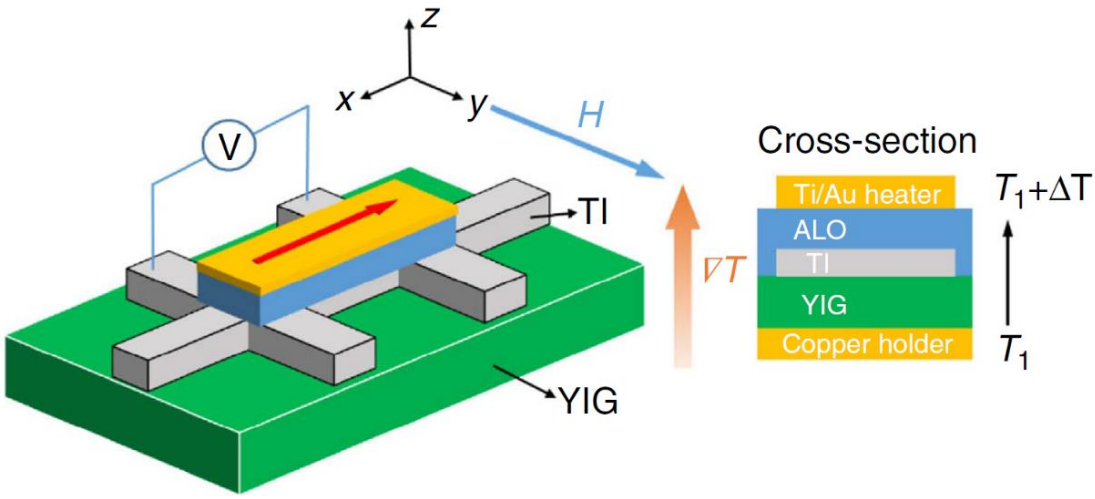

Figure 4-5 Device schematics for longitudinal SSE measurement. The TI layer of the YIG/TI heterostructure is etched to a Hall bar. An insulating Al_2O_3 layer covers the entire surface. The top Ti/Au layer behaves as a heater. A current in the heater generate a vertical temperature gradient ∇T. An in-plane magnetic field is applied along y axis. The voltage signal is measured from two TI leads along x axis. The side view shows the layered structure of the device.

contacts of Ti(5 nm)/Au(80 nm) are deposited on the Hall bar leads by electron-beam evaporation. The sample is then transferred into an atomic layer deposition (ALD) chamber for a 150 nm Al_2O_3 insulating layer growth. Finally, a 100 μm wide Ti(5 nm)/Au(45 nm) heater is deposited on the Al_2O_3 layer aligned with the TI Hall bar channel. In the measurement, we send a DC current in the heater with various magnitude, to generate a controllable temperature gradient ∇T. The real temperature of the TI sample is monitored by measuring the longitudinal resistance of the Hall bar. In measurements with different heating power, the real temperature is always kept the same by cooling the sample holder in a closed-cycle refrigerator. With the heater turned on, the ∇T driven non-equilibrium magnons decay on the TI surface due to spin-momentum locking, which generates a voltage signal along the TI channel direction. By sweeping the in-plane magnetic field along y-axis, a hysteresis voltage loop is expected.

4.4 Elimination of proximity induced anomalous Nernst contribution

In a longitudinal SSE geometry consisting of a magnetic insulator and a heavy metal with strong spin-orbit coupling, there is a magnetic proximity induced magnetic layer which can generate anomalous Nernst voltage to contaminate the SSE signal[46,47]. For our YIG/TI heterostructure, the proximity effect could also exist and the anomalous Nernst voltage may contribute to the measured voltage. We take anomalous Hall measurement to have an insight of the strength of the induced ferromagnetism in the TI. Fig. 4-6 (a) shows the anomalous Hall curve of a 5 QL $(Bi_{0.24}Sb_{0.76})_2Te_3$ on YIG sample measured at 13 K, which comes from removing the linear ordinary Hall background of

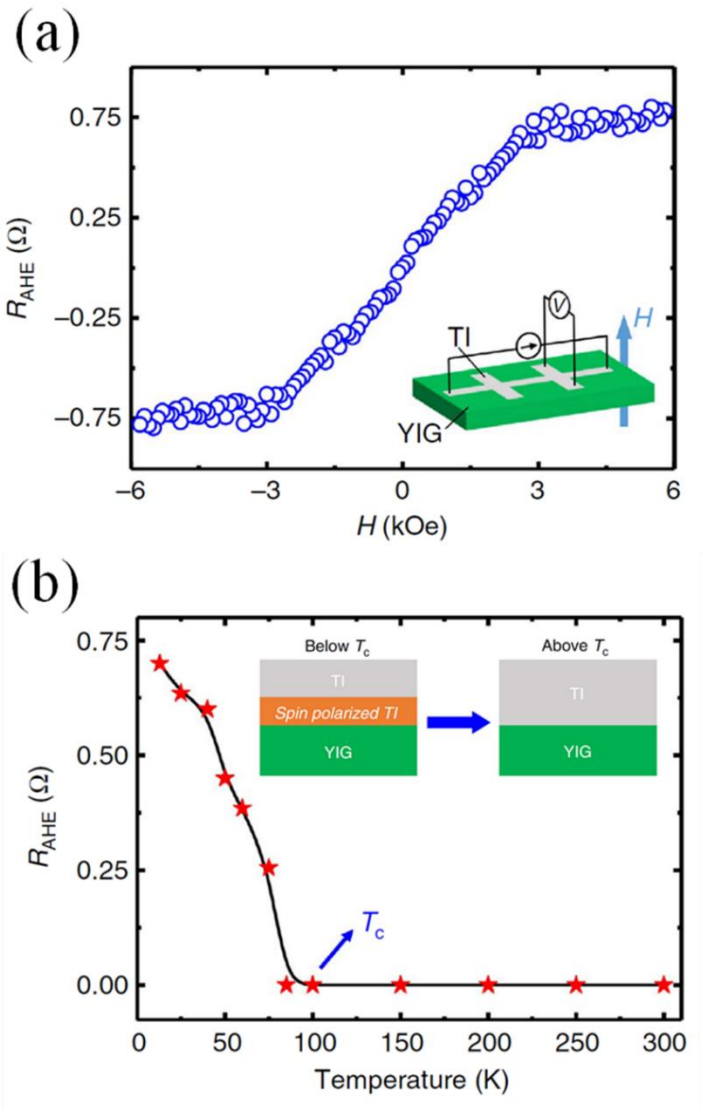

Figure 4-6 Proximity-induced magnetism in TI at low temperatures. (a) A typical anomalous Hall curve for a 5 QL $(Bi_{0.24}Sb_{0.76})_2Te_3$ on YIG sample measured at 13 K. The inset is a schematic illustration of the Hall measurement. (b) The anomalous Hall resistance as a function of temperature for the same sample. It shows that the proximity-induced surface state magnetization exists below 100 K. The inset is a schematic illustration of the proximity-induced magnetization below and above T_c. Below T_c, the TI interface layer is spin polarized, which may produce an anomalous Nernst voltage to contaminate the SSE signal. Above T_c, there is no magnetized layer.

the total Hall signal. A schematic illustration of the Hall measurement setup is shown in the inset. The shape of the nonlinear Hall curve follows the YIG out of plane magnetization hysteresis loop, indicating that the magnetic order participates strongly in the conducting states on the YIG/TI interface. Fig. 4-6 (b) shows the anomalous Hall resistance R_{AHE} as a function of temperature for the same sample. R_{AHE} decreases with temperature going up and becomes zero above a critical temperature $T_c \sim 100$ K. It suggests that proximity-induced surface state magnetization exists up to 100 K. The inset is a schematic illustration of the proximity-induced magnetization below and above T_c. Below T_c, the TI interface layer is spin polarized, which may produce an anomalous Nernst voltage to contaminate the SSE signal. Above T_c, the interface of YIG/TI has no magnetized layer. We have observed anomalous Hall signal from other YIG/TI samples with T_c ranging from 20 K up to 150 K. For each YIG/TI sample, we carry out longitudinal SSE measurement at temperature above its T_c. We conclude that the mean exchange energy experienced by the TI surface states is negligible, and that the SSE voltage we measured is free from contamination of proximity induced anomalous Nernst effect.

4.5 SSE results for YIG/$(Bi_xSb_{1-x})_2Te_3$ samples with various x

Fig. 4-7 shows typical SSE voltage V_{SSE} as a function of applied in-plane magnetic field for a YIG/$(Bi_xSb_{1-x})_2Te_3$ sample with $x = 0.24$ at 300 K. When the magnetic field H is swept along y-axis ($\theta = 0°$), V_{SSE} exhibits a hysteresis loop resembles the in-plane magnetic hysteresis loop of the YIG film measured by VSM. For H

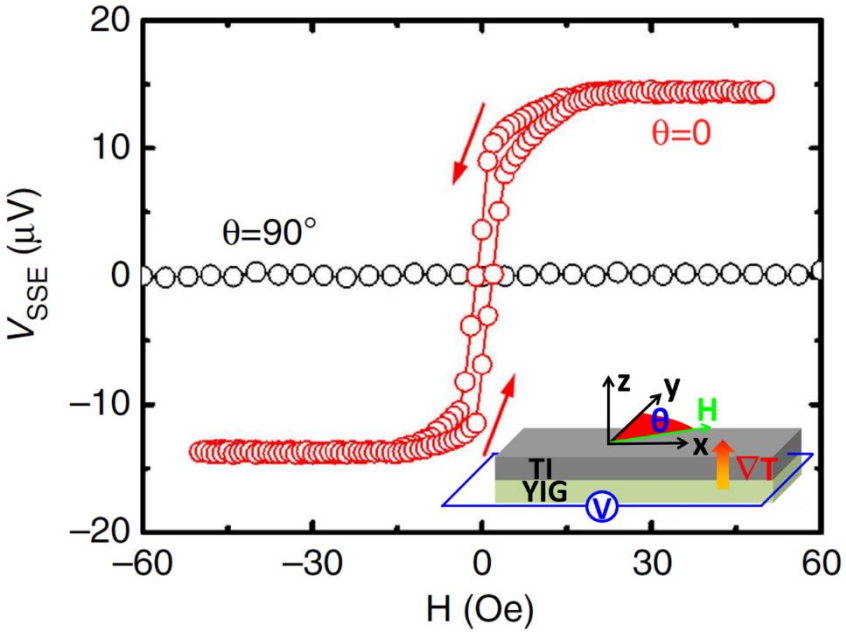

Figure 4-7 V_{SSE} hysteresis loops of a 5 QL $(Bi_{0.24}Sb_{0.76})_2Te_3$ on YIG sample at room temperature for magnetic field swept along two different directions. The applied heater current is 80 mA. The inset shows the measurement geometry.

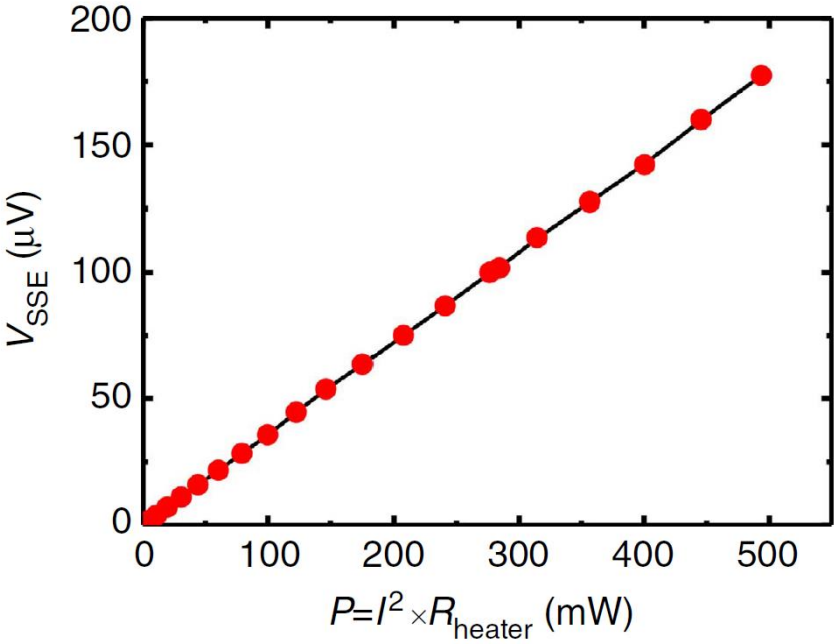

Figure 4-8 Spin Seebeck voltage as a function of the heater power for the YIG/$(Bi_{0.24}Sb_{0.76})_2Te_3$ sample. The black line is linear fit.

sweeping along x-axis (θ =90°), there is no observable V_{SSE}, which is consistent with the prediction in Fig. 4-2. Since the temperature gradient ∇T is proportional to the heater power $P=I^2R_{heater}$, we can conveniently control ∇T by adjusting the heater current I and monitor the heater resistance R_{heater}. Fig. 4-8 shows V_{SSE} as a function of the heater power for the YIG/$(Bi_{0.24}Sb_{0.76})_2Te_3$ sample. The linear relation indicates $V_{SSE} \propto \nabla T$, which is consistent with the theory for heat driven magnon transport in YIG.

In a TI sample, both surface states and bulk states have strong spin-orbit coupling, so both can contribute to the measured V_{SSE}. We need to systematically tune the Fermi level, either by change Bi ratio or by applying a gate voltage, to investigate the relative contribution from surface and bulk states. Here, we measure 5 different YIG/$(Bi_xSb_{1-x})_2Te_3$ samples with x=0, 0.23, 0.24, 0.36 and 1. In Fig. 4-9 we show the sheet resistance R_{xx} as a function of temperature for the 5 different samples. For samples with x=0 and 1, R_{xx} goes down as temperature decreases, indicating a metallic behavior. Compared with x=0 and 1 samples, the x=0.36 one has a larger R_{xx} and an insulator-like temperature dependence. For the x=0.23 and 0.24 samples, R_{xx} increases with decreasing T for the entire temperature range, indicating a stronger insulator-like behavior, which means the bulk states are mostly suppressed. With charge carrier type and density determined by ordinary Hall measurement, in the insets of Fig. 4-9, we depict Fermi level position relative to the Dirac point of surface states for different values of x.

The five samples have been fabricated to the same dimension and structure with the exactly same process, so it is reasonable to quantitatively compare their V_{SSE}. Fig. 4-10 shows the field dependence of V_{SSE} in the five different YIG/$(Bi_xSb_{1-x})_2Te_3$ samples at

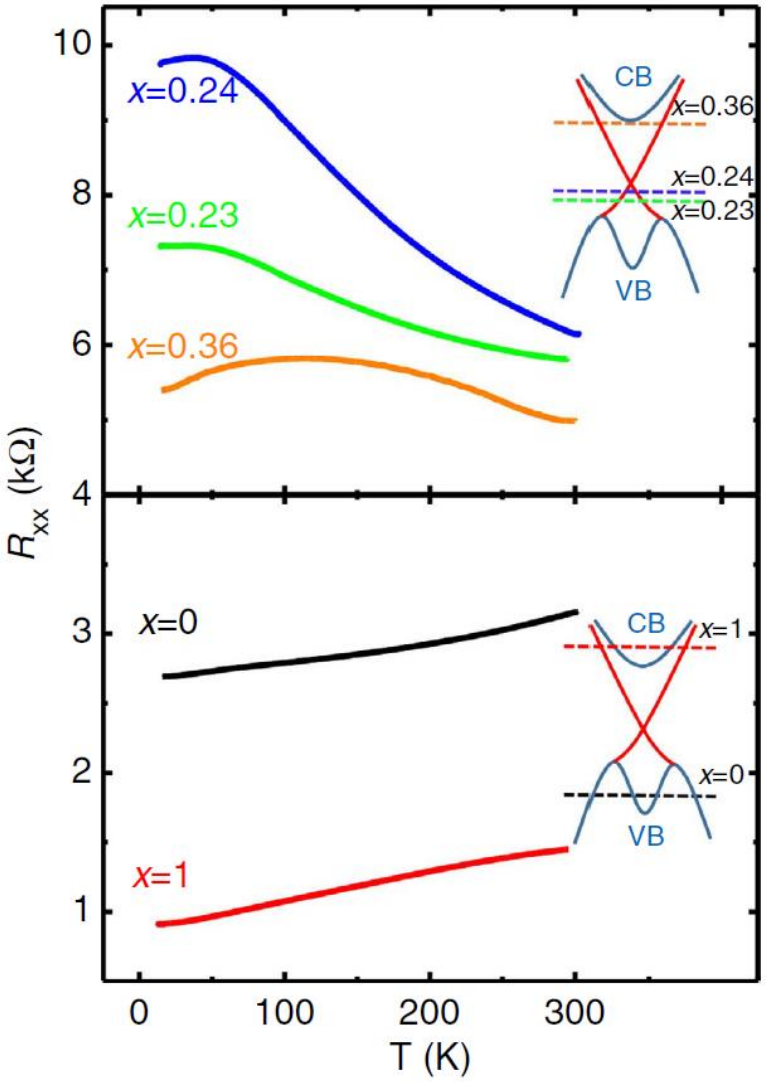

Figure 4-9 Longitudinal sheet resistance R_{xx} vs. temperature for 5 different YIG/$(Bi_xSb_{1-x})_2Te_3$ samples with x ranging from 0 to 1. The insets schematically show the Fermi level in the band structure for different values of x.

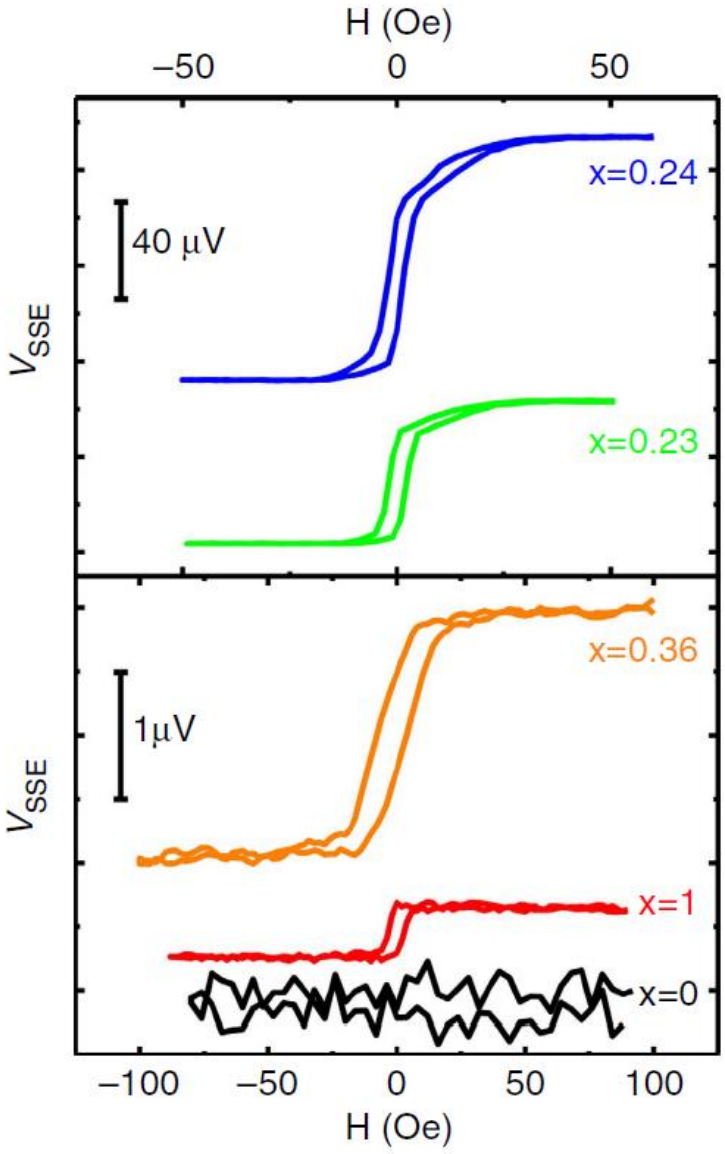

Figure 4-10 Field dependence of V_{SSE} in 5 different YIG/$(Bi_xSb_{1-x})_2Te_3$ samples. The heater power is kept the same for all samples.

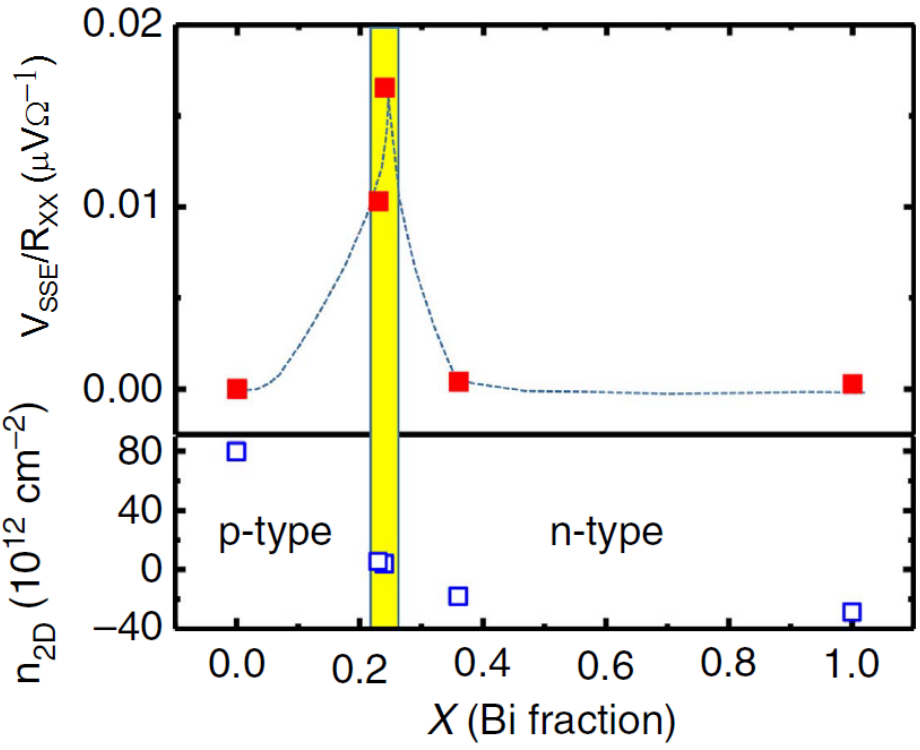

Figure 4-11 V_{SSE}/R_{xx} and two-dimensional carrier density for various x values. The charge current induced by magnon decay at YIG/TI interface is much larger for insulating samples (x=0.23 and 0.24) than for metallic samples (x=0 and 1), which further demonstrates the dominant role of TI surface states in converting magnons to an electrical voltage signal.

300 K. The heater power is fixed at 283 mW for all samples. For x=0, there is no detectable V_{SSE} and its Fermi level lies inside bulk valence band (Fig. 4-9 inset) with a high hole density of 8×10^{13} cm^{-2}. V_{SSE} goes up to 60 μV for x=0.23, and continues going up to 100 μV for x=0.24. At x=0.24, the Fermi level is very close to Dirac point and the electronic density of states is dominated by topological surface states. It has a quite low carrier density, n_{2D} =4×10^{12} cm^{-2}. V_{SSE} decreases significantly to 1.94 μV for x=0.36, and further goes down to 0.41 μV for x=1. The huge difference of V_{SSE} between metallic

and insulating samples indicates the dominant role of the topological surface states in converting magnons to an electrical voltage signal. To exclude the current shunting effect from conducting channels of TI bulk and top surface, we plot V_{SSE}/R_{xx} vs. x in Fig. 4-11. It shows that the charge current induced by magnon decay on YIG/TI interface is also greatly enhanced when surface states dominate.

4.6 Exploring the topological SSE by electrostatic gating

Although we have demonstrated the dominant role of topological surface states in converting magnons to electrical voltage, we cannot continuously tune the Fermi level by changing the Bi/Sb ratio of $(Bi_xSb_{1-x})_2Te_3$, and the band structure in samples with different x wouldn't be exactly the same. To have a better understanding of the topological SSE of TI surface states, especially at the unique Dirac point, we try to tune the Fermi level continuously with electrostatic gating on a single TI sample.

Fig. 4-12 schematically shows the device structure and measurement setup for the longitudinal SSE measurement with top gating. Here, we use a 100 nm thick HfO_2 as the insulating layer, instead of the 150 nm thick Al_2O_3 in previous samples. HfO_2 has a dielectric constant κ of 25, which is much higher than that of 9 for Al_2O_3[92]. The thickness reduction also helps to make the top gate more effective. A top gate voltage V_g is applied between the top Au layer and the bottom TI layer, which can tune the Fermin level of TI surface states without changing the sample's band structure. At the same time, we send a DC current in the Au layer to provide a temperature gradient ∇T, just like in previous measurements.

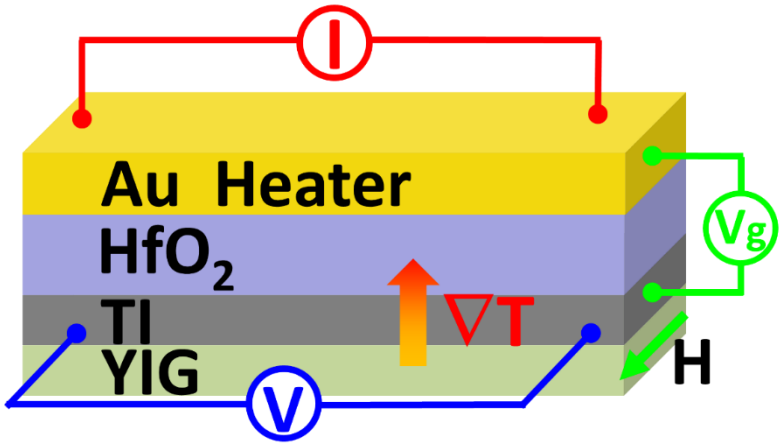

Figure 4-12 Schematic illustration of the longitudinal SSE measurement with top gating. The 100 nm thick HfO_2 is used as a dielectric layer. A gate voltage *V*g is applied between the top Au layer and the TI layer.

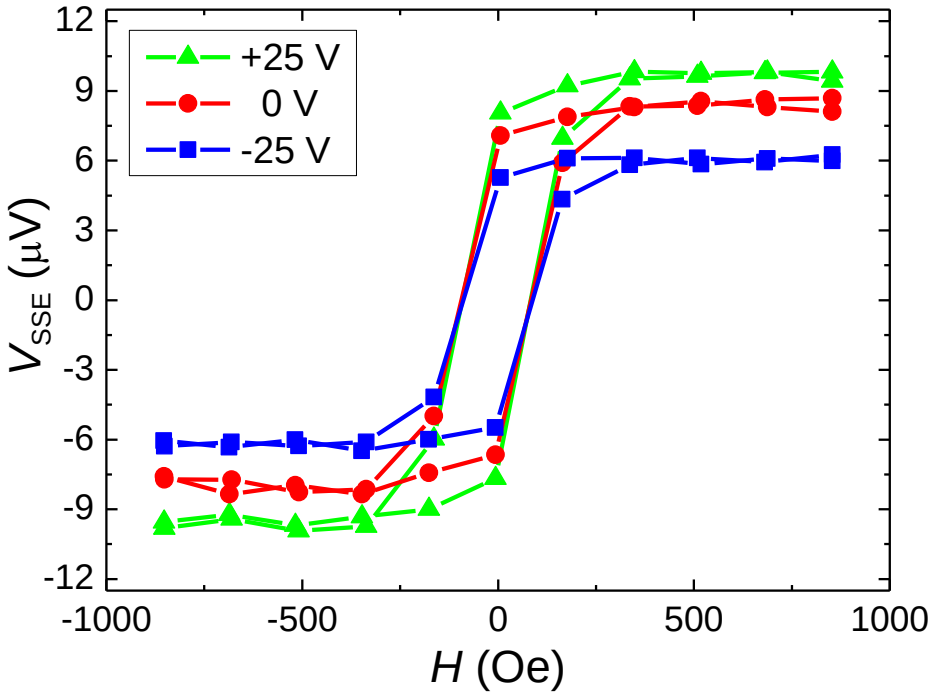

Figure 4-13 Field dependence of longitudinal SSE voltage of a 5 QL $(Bi_{0.3}Sb_{0.7})_2Te_3$ on YIG sample at 3 different top gate voltages at 20 K. V_{SSE} has obvious response to *V*g. V_{SSE} is 6, 8.3, 9.7 μV for *V*g at -25, 0 and +25 V respectively.

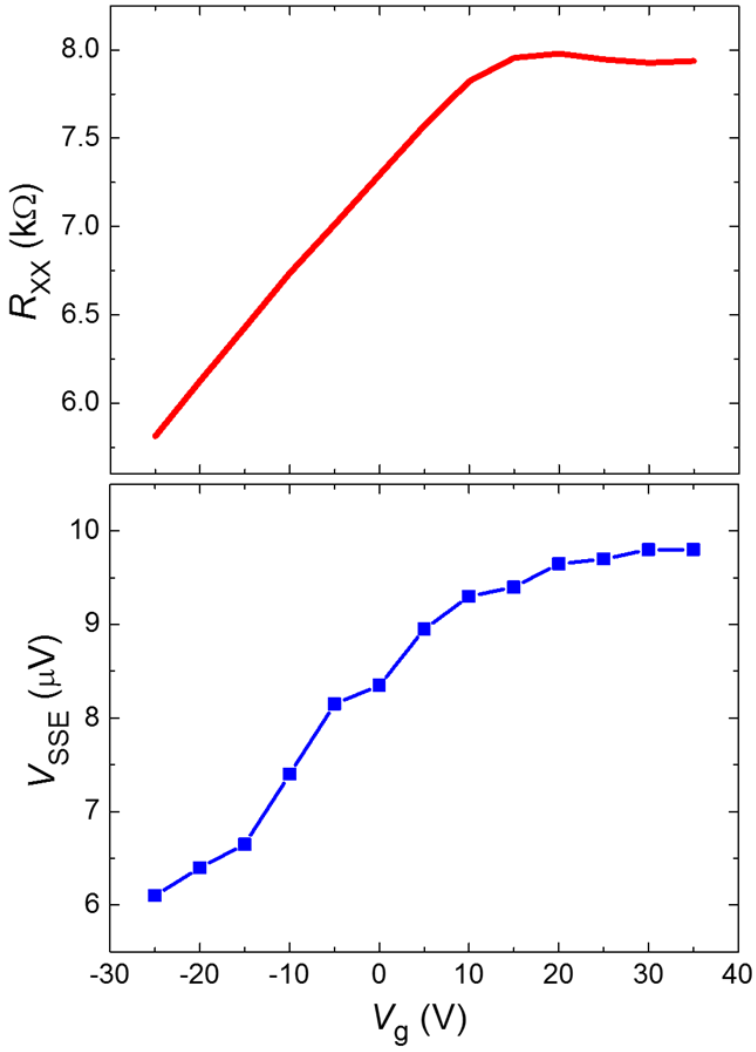

Figure 4-14 Gate voltage dependence of the sheet resistance R_{xx} and the spin Seebeck voltage V_{SSE}. The two curves share a similar shape.

In Fig. 4-13, we show the longitudinal SSE voltage V_{SSE} vs. H of a 5 QL $(Bi_{0.3}Sb_{0.7})_2Te_3$ on YIG sample (Sample 1) at 3 different top gate voltages at 20 K. V_{SSE} has higher value at higher Vg, i.e., V_{SSE} is 6, 8.3 and 9.7 μV for Vg at -25, 0 and +25 V respectively. Fig. 4-14 shows the gate voltage V_g dependence of the sheet resistance R_{xx} and corresponding V_{SSE}. With V_g sweeping from negative to positive value, R_{xx} first increases rapidly from 5.8 kΩ at −25 V to 8.0 kΩ at +20 V, and then slowly decreases to 7.9 kΩ at +35 V. The behavior of resistance increase and decrease with V_g suggests that the Fermi level rises from valence band, approaches Dirac point and may just cross Dirac point. V_{SSE} is measured with a 5 V step size of V_g. The V_{SSE} vs. V_g curve shows a similar

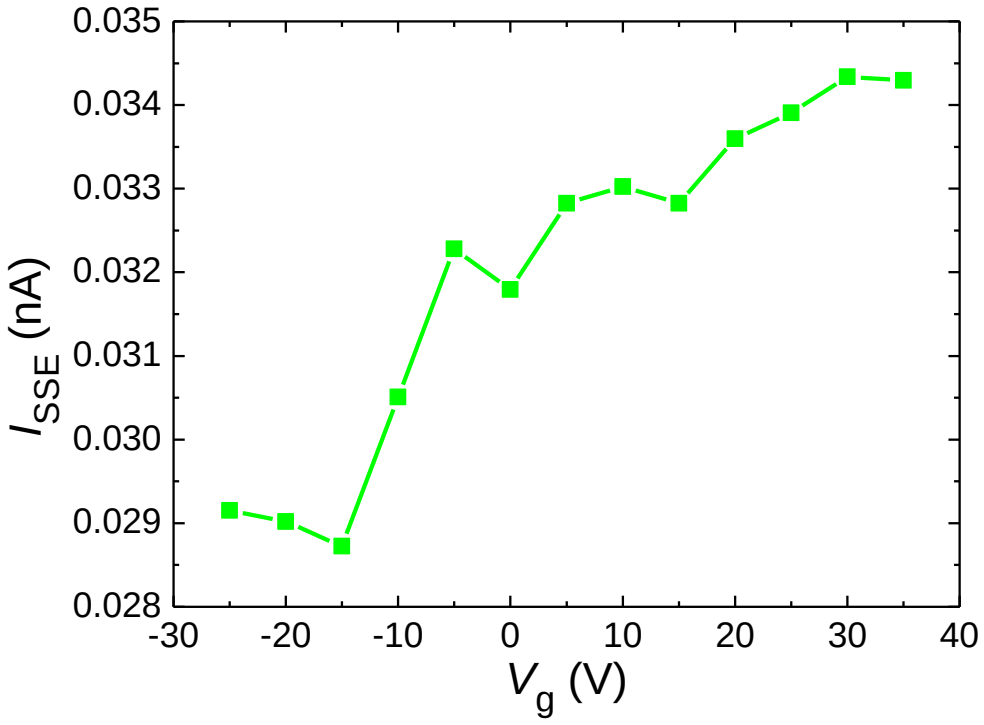

Figure 4-15 Gate voltage dependence of the SSE induced charge current I_{SSE} in the TI sample. The curve has a general increasing trend on the whole gate voltage range with a relative change of about 20%.

trend with R_{xx} vs. V_g. It may indicate a higher magnon-charge convert efficiency when Fermi level approaches Dirac point. We calculate the induced charge current I_{SSE}, i.e., divide V_{SSE} by the total resistance at each gate voltage, and plot it vs. Vg in Fig. 4-15. The curve has a general increasing trend on the whole gate voltage range. The relative change from -25 V to $+35$ V is about 20%, much smaller than that shown in Fig. 4-11 by tuning the Bi/Sb ratio.

To confirm the observed phenomenon, we repeat the measurement on another YIG/$(Bi_xSb_{1-x})_2Te_3$ sample with a nominally the same value of x (Sample 2). As shown in Fig. 4-16, the R_{xx} vs V_g has a clear peak at $V_g = -15$ V, indicating the Fermi level successfully crosses Dirac point of the surface states for this sample. The right side of the peak is obviously higher than the left. In Fig. 4-16, V_{SSE} vs. V_g follows a similar trend of R_{xx}, just like Sample 1, and exhibits a peak at the same gate voltage. But the right side of the peak doesn't show a higher level than the left. The calculated charge current I_{SSE} is shown in Fig. 4-17. I_{SSE} shows a decreasing trend as gate voltage V_g increases, which only resembles the behavior of R_{xx} to the right of the peak, shown in Fig. 4-16.

To tune the Fermi level of TI by top gating, we get a much smaller response of I_{SSE}, compared with varying Bi/Sb ratio as shown in Fig. 4-11. A 3D TI can be viewed to have three parallel conduction channels: top surface, bulk and bottom surface. In the YIG/TI samples, the magnon-charge conversion happens at the YIG/TI interface, i.e., the bottom surface of TI. The R_{xx} vs. V_g response indicates that the top gate can tune the carrier density, but maybe with different effectiveness on the three channels. The top surface should be affected most and the bottom surface least, because of electric

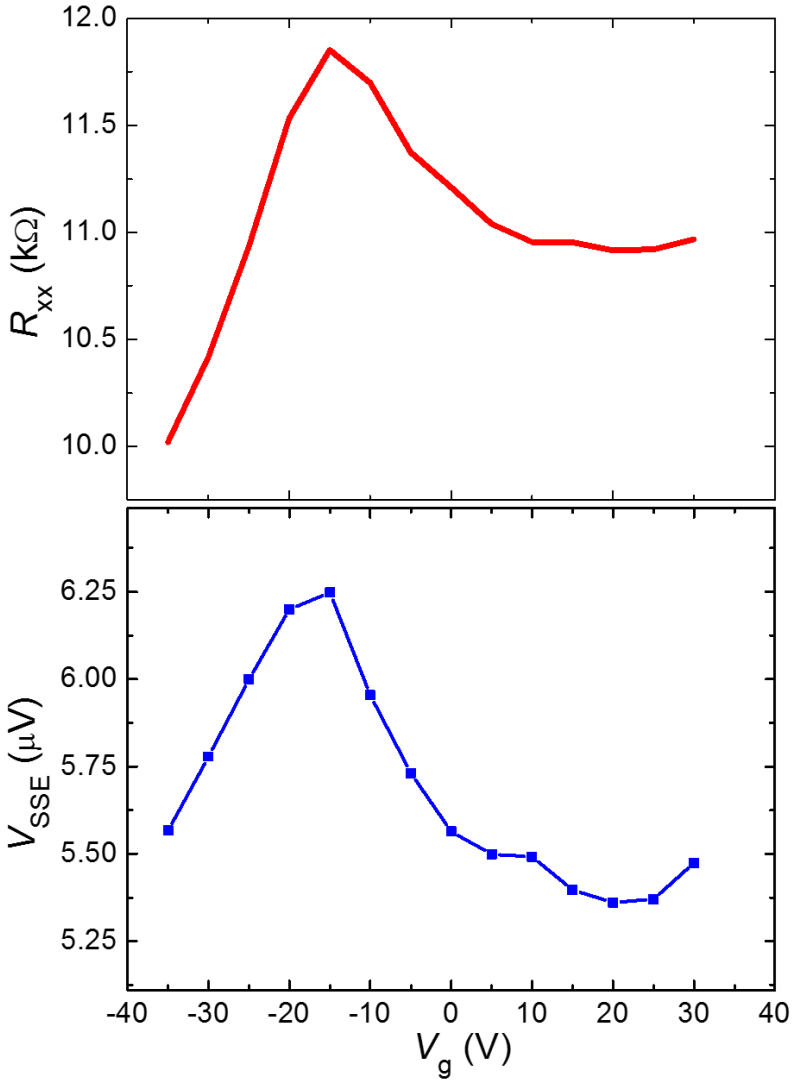

Figure 4-16 Gate voltage dependence of the sheet resistance R_{xx} and the spin Seebeck voltage V_{SSE} of another YIG/TI sample (Sample 2).

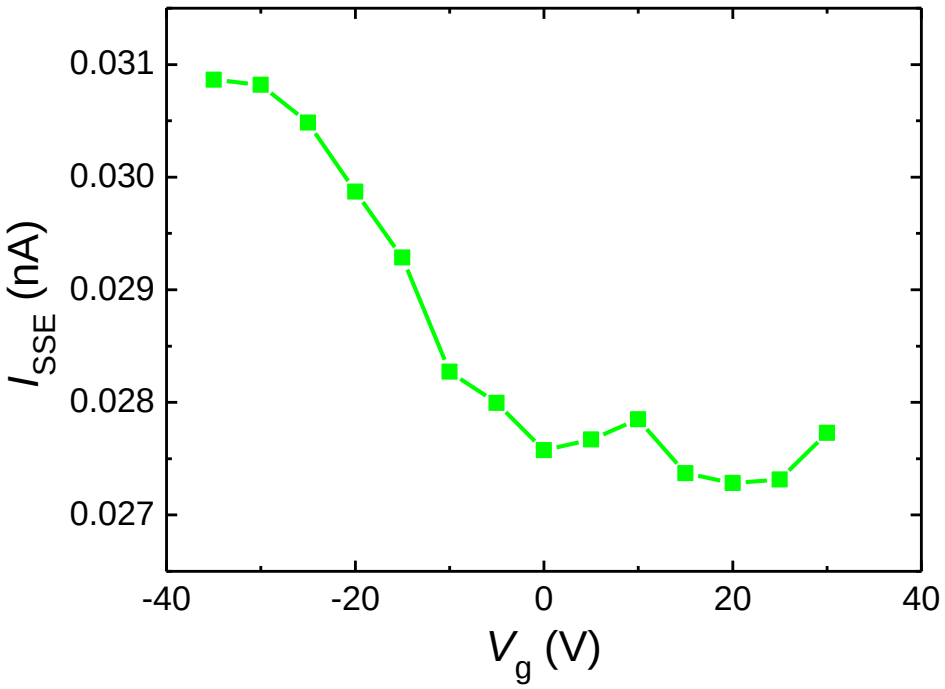

Figure 4-17 Gate voltage dependence of the SSE induced charge current I_{SSE} in Sample 2. With V_g increasing, the current first decreases rapidly and then kind of saturates above 0 V, with a relative change of 12%.

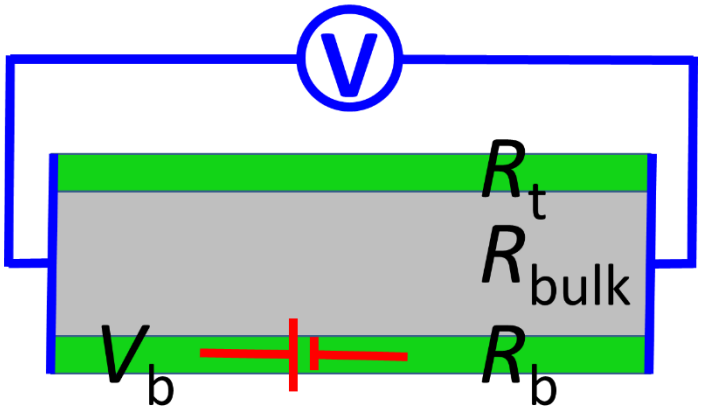

Figure 4-18 Schematic illustration of the paralleled conduction channels of a TI in longitudinal SSE measurement. Only the bottom surface contributes an electrical voltage due to magnon-charge conversion.

screening effect. As illustrated in Fig. 4-18, only the bottom surface generates an electric voltage V_b due to magnon decay, while the bulk and top surface act as two current shunting channels. The total measured SSE voltage can be expressed as $V_{SSE} = R\frac{V_b}{R_b}$, where R is the total resistance of the TI sample and R_b is the resistance of the bottom surface. If the top gate only has a small effect on the Fermi level of bottom surface, then the change of $\frac{V_b}{R_b}$ will be very small. The measured SSE voltage V_{SSE} will generally follow the trend of the total resistance R, and the induced charge current will have limited variation, as $I_{SSE} = \frac{V_{SSE}}{R} = \frac{V_b}{R_b}$. These assumptions match quite well with what we observed from the two samples.

For further exploration of magnon-charge conversion on TI surface states, a YIG/TI sample with a back gate for Fermi level tuning is necessary. To achieve back gating through YIG, one possible way is depositing YIG films on a thin layer of Pt, as described in Chapter 3. The YIG insulating property needs improvement to stand a high gate voltage without current leaking. Another possible way is depositing YIG on $SrTiO_3$ (STO) substrates. STO has very large dielectric constant ($\sim 10^4$) at low temperature, so a reasonable gate voltage can provide significant electric field through a thin STO substrate. However, the lattice constant mismatch could make it very challenging to grow high quality YIG films on STO substrates.

References

1. Baibich, M. N. *et al.* Giant magnetoresistance of (001)Fe/(001)Cr magnetic superlattices. *Phys. Rev. Lett.* **61**, 2472 (1988).

2. Hirsch, J. E. Spin Hall effect. *Phys. Rev. Lett.* **83**, 1834–1837 (1999).

3. Dyakonov, M. I. & Perel, V. I. Possibility of orienting electron spins with current. *JETP Lett.* **13**, 467–469 (1971).

4. Murakami, S., Nagaosa, N. & Zhang, S. C. Dissipationless quantum spin current at room temperature. *Science* **301**, 1348–1351 (2003).

5. Sinova, J. *et al.* Universal intrinsic spin Hall effect. *Phys. Rev. Lett.* **92**, 126603 (2004).

6. Kato, Y. K., Myers, R. C., Gossard, A. C. & Awschalom, D. D. Observation of the spin Hall effect in semiconductors. *Science* **306**, 1910–1913 (2004).

7. Wunderlich, J., Kaestner, B., Sinova, J. & Jungwirth, T. Experimental observation of the spin Hall effect in a two-dimensional spin-orbit coupled semiconductor system. *Phys. Rev. Lett.* **94**, 047204 (2005).

8. Ando, K. *et al.* Photoinduced inverse spin-Hall effect: Conversion of light-polarization information into electric voltage. *Appl. Phys. Lett.* **96**, 082502 (2010).

9. Zhang, S. Spin Hall effect in the presence of spin diffusion. *Phys. Rev. Lett.* **85**, 393–396 (2000).

10. Valenzuela, S. O. & Tinkham, M. Direct electronic measurement of the spin Hall effect. *Nature* **442,** 176–179 (2006).

11. Saitoh, E., Ueda, M., Miyajima, H. & Tatara, G. Conversion of spin current into charge current at room temperature: inverse spin-Hall effect. *Appl. Phys. Lett*. **88,** 182509 (2006).

12. Huang, S. Y. *et al.* Transport magnetic proximity effects in platinum. *Phys. Rev. Lett.* **109**, 107204 (2012).

13. Nakayama, H. *et al*. Spin Hall magnetoresistance induced by a nonequilibrium proximity effect. *Phys. Rev. Lett.* **110**, 206601 (2013).

14. Ando, K. *et al.* Electric manipulation of spin relaxation using the spin Hall effect. *Phys. Rev. Lett.* **101**, 036601 (2008).

15. Liu, L., Moriyama, T., Ralph, D. C. & Buhrman, R. A. Spin-torque ferromagnetic resonance induced by the spin Hall effect. *Phys. Rev. Lett.* **106**, 036601 (2011).

16. Miron, I. M. *et al.* Perpendicular switching of a single ferromagnetic layer induced by in-plane current injection. *Nature* **476**, 189–193 (2011)

17. Liu, L., Lee, O. J., Gudmundsen, T. J., Ralph, D. C. & Buhrman, R. A. Current-induced switching of perpendicularly magnetized magnetic layers using spin torque from the spin Hall effect. *Phys. Rev. Lett.* **109**, 096602 (2012).

18. Li, J. *et al.* Deficiency of the bulk spin Hall effect model for spin-orbit torques in magnetic insulator/heavy metal heterostructures. arXiv:1705.08919

19. Liu, L. *et al.* Spin-torque switching with the giant spin Hall effect of tantalum. *Science* **336**, 555–558 (2012).

20. Bauer, G. E.W., Saitoh, E. & vanWees, B. J. Spin caloritronics. *Nature Mater.* **11,** 391–399 (2012).

21. Slachter, A., Bakker, F. L., Adam, J. P. & van Wees, B. J. Thermally driven spin injection from a ferromagnet into a non-magnetic metal. *Nature Phys*. **6,** 879–882 (2010).

22. Flipse, J., Bakker, F. L., Slachter, A., Dejene, F. K. & van Wees, B. J. Direct observation of the spin-dependent Peltier effect. *Nature Nanotech*. **7,** 166–168 (2012).

23. Uchida, K. *et al.* Observation of the spin Seebeck effect. *Nature* **455**, 778–781 (2008).

24. Uchida, K. *et al.* Spin-Seebeck effects in NiFe/Pt films. *Solid State Commun*. **150,** 524–528 (2010).

25. Uchida, K. *et al.* Spin Seebeck insulator. *Nature Mater*. **9,** 894–897 (2010).

26. Jaworski, C. M. *et al.* Observation of the spin-Seebeck effect in a ferromagnetic semiconductor. *Nature Mater*. **9,** 898–903 (2010).

27. Uchida, K., Nonaka, T, Ota, T. & Saitoh, E. Observation of longitudinal spin-Seebeck effect in magnetic insulators. *Appl. Phys. Lett*. **97,** 172505 (2010).

28. Huang, S. Y., Wang, W. G., Lee, S. F., Kwo, J. & Chien, C. L. Intrinsic spin-dependent thermal transport. *Phys. Rev. Lett*. **107,** 216604 (2011).

29. Kirihara, A. *et al*. Spin-current-driven thermoelectric coating. *Nature Mater*. **11**, 686–689 (2012).

30. Chumak, A. V., Vasyuchka, V. I., Serga, A. A. & Hillebrands, B. Magnon spintronics. *Nature Phys.* **11**, 453–461 (2015).

31. Kajiwara, Y. *et al*. Transmission of electrical signals by spin-wave interconversion in a magnetic insulator. *Nature* **464,** 262–266 (2010).

32. Hamadeh, A. *et al*. Full control of the spin-wave damping in a magnetic insulator using spin orbit torque. *Phys. Rev. Lett.* **113,** 197203 (2014).

33. Castel, V., Vlietstra, N., Ben Youssef, J. & vanWees, B. J. Platinum thickness dependence of the inverse spin-Hall voltage from spin pumping in a hybrid yttrium iron garnet/platinum system. *Appl. Phys. Lett.* **101,** 132414 (2012).

34. Hahn, C. *et al*. Comparative measurements of inverse spin Hall effects and magnetoresistance in YIG/Pt and YIG/Ta. *Phys. Rev. B* **87,** 174417 (2013).

35. Weiler, M. *et al.* Experimental test of the spin mixing interface conductivity concept. *Phys. Rev. Lett.* **111,** 176601 (2013).

36. Castel, V., Vlietstra, N., vanWees, B. J. & Ben Youssef, J. Yttrium iron garnet thickness and frequency dependence of the spin-charge current conversion in YIG/Pt systems. *Phys. Rev. B* **90,** 214434 (2014).

37. Jungfleisch, M. B. *et al.* Thickness and power dependence of the spin-pumping effect in $Y_3Fe_5O_{12}$/Pt heterostructures measured by the inverse spin Hall effect. *Phys. Rev. B* **91,** 134407 (2015).

38. Burrowes, C. *et al.* Enhanced spin pumping at yttrium iron garnet/Au interfaces. *Appl. Phys. Lett.* **100,** 092403 (2012).

39. Jungfleisch, M. B., Lauer, V., Neb, R., Chumak, A. V. & Hillebrands, B. Improvement of the yttrium iron garnet/platinum interface for spin pumping-based applications. *Appl. Phys. Lett.* **103,** 022411 (2013).

40. Xiao, J. & Bauer, G. E.W. Spin-wave excitation in magnetic insulators by spin-transfer torque. *Phys. Rev. Lett.* **108,** 217204 (2012).

41. Kapelrud, A. & Brataas, A. Spin pumping and enhanced Gilbert damping in thin magnetic insulator films. *Phys. Rev. Lett.* **111,** 097602 (2013).

42. Chumak, A. V. *et al.* Direct detection of magnon spin transport by the inverse spin Hall effect. *Appl. Phys. Lett.* **100**, 082405 (2012).

43. Sandweg, C.W. *et al.* Spin pumping by parametrically excited exchange magnons. *Phys. Rev. Lett.* **106,** 216601 (2011).

44. Dyakonov, M. I. & Perel, V. I. Current-induced spin orientation of electrons in semiconductors. *Phys. Lett. A* **35**, 459–460 (1971).

45. Miao, B. F., Huang, S. Y., Qu, D. & Chien, C. L. Inverse spin Hall effect in a ferromagnetic metal. *Phys. Rev. Lett.* **111**, 066602 (2013).

46. Qu, D. Huang, S. Y. Hu, J. Wu, R. & Chien, C. L. Intrinsic Spin Seebeck Effect in Au/YIG. *Phys. Rev. Lett.* **110**, 067206 (2013).

47. Kikkawa, T. *et al*. Longitudinal spin Seebeck effect free from the proximity Nernst effect. *Phys. Rev. Lett.* **110**, 067207 (2013).

48. Lin, T., Tang, C. & Shi, J. Induced magneto-transport properties at palladium/yttrium iron garnet interface. *Appl. Phys. Lett.* **103**, 132407 (2013).

49. Lin, T., Tang, C., Alyahayaei, H. & Shi, J. Experimental investigation of the nature of the magnetoresistance effects in Pd-YIG hybrid structure. *Phys. Rev. Lett.* **113**, 037203 (2014).

50. Kondou, K., Sukegawa, H., Mitani, S., Tsukagoshi, K. & Kasai, S. Evaluation of spin Hall angle and spin diffusion length by using spin current-induced ferromagnetic resonance. *Appl. Phys. Expr.* **5**, 073002 (2012).

51. Steenwyk, S. D., Hsu, S. Y., Loloee, R., Bass, J. & PrattJr., W. P. Perpendicular-current exchanged-biased spin-valve evidence for a short spin-diffusion length in permalloy. *J. Magn. Magn. Mater.* **170**, L1–L6 (1997).

52. Costache, M. V., Sladkov, M., Watts, S. M., van der Wal, C. H. & van Wees, B. J. Electrical detection of spin pumping due to the precessing magnetization of a single ferromagnet. *Phys. Rev. Lett.* **97**, 216603 (2006).

53. Mosendz, O. *et al.* Quantifying spin Hall angles from spin pumping: experiments and theory. *Phys. Rev. Lett.* **104**, 046601 (2010).

54. Vlaminck, V. *et al.* Dependence of spin-pumping spin Hall effect measurements on layer thicknesses and stacking order. *Phys. Rev. B* **88**, 064414 (2013).

55. Zhang, W. *et al.* Spin Hall effects in metallic antiferromagnets. *Phys. Rev. Lett.* **113**, 196602 (2014).

56. Slonczewski, J. C. Current-driven excitation of magnetic multilayers. *J. Magn. Magn. Mater.* **159**, L1–L7 (1996).

57. Berger, L. Emission of spin waves by a magnetic multilayer traversed by a current. *Phys. Rev. B* **54**, 9353–9358 (1996).

58. Zhang, S. S.-L. & Zhang, S. Magnon mediated electric current drag across a ferromagnetic insulator layer. *Phys. Rev. Lett.* **109**, 096603 (2012).

59. Zhang, S. S.-L. & Zhang, S. Spin convertance at magnetic interfaces. *Phys. Rev. B* **86**, 214424 (2012).

60. Cornelissen, L. J. *et al.* Long distance transport of magnon spin information in a magnetic insulator at room temperature. *Nature Phys.* **11**, 453–461 (2015).

61. Takahashi, S., Saitoh, E. & Maekawa, S. Spin current through a normal metal/insulating-ferromagnet Junction. *J. Phys. Conf. Ser.* **200**, 062030 (2010).

62. Tanaka, T. *et al.* Intrinsic spin Hall effect and orbital Hall effect in 4d and 5d transition metals. *Phys. Rev. B* **77**, 165117 (2008).

63. Morota, M. *et al.* Indication of intrinsic spin Hall effect in 4d and 5d transition metals. *Phys. Rev. B* **83**, 174405 (2011).

64. Chen, Y-T. *et al.* Theory of spin Hall magnetoresistance. *Phys. Rev. B* **87**, 144411 (2013).

65. Lu, Y. M. *et al*. Hybrid magnetoresistance in the proximity of a ferromagnet. *Phys. Rev. B* **87**, 220409 (2013).

66. Lu, Y. M. *et al*. Pt magnetic polarization on $Y_3Fe_5O_{12}$ and magnetotransport characteristics. *Phys. Rev. Lett.* **110**, 147207 (2013).

67. Goennenwein, S. T. B., Schlitz, R., Pernpeintner, M., Ganzhorn, K., Althammer, M., Gross, R., and Huebl, H. Non-local magnetoresistance in YIG/Pt nanostructures. *Appl. Phys. Lett.* **107**, 172405 (2015).

68. Hasan, M. Z. & Kane, C. L. Colloquium: topological insulators. *Rev. Mod. Phys.* **82**, 3045–3067 (2010).

69. Qi, X.-L. & Zhang, S.-C. Topological insulators and superconductors. *Rev. Mod. Phys.* **83**, 1057–1110 (2011).

70. Hsieh, D. *et al*. Observation of unconventional quantum spin textures in topological insulators. *Science* **323**, 919–922 (2009).

71. Xia, Y. *et al*. Observation of a large-gap topological-insulator class with a single Dirac cone on the surface. *Nature Phys.* **5**, 398–402 (2009).

72. Chen, Y. L. *et al*. Experimental realization of a three-dimensional topological insulator, Bi_2Te_3. *Science* **325**, 178–181 (2009).

73. Shiomi, Y. *et al.* Spin-electricity conversion induced by spin injection into topological insulators. *Phys. Rev. Lett.* **113**, 196601 (2014).

74. Mellnik, A. R. *et al.* Spin-transfer torque generated by a topological insulator. *Nature* **511**, 449–451 (2014).

75. Wang, Y. *et al.* Topological surface states originated spin-orbit torques in Bi_2Se_3. *Phys. Rev. Lett.* **114**, 257202 (2015).

76. Kondou, K. *et al.* Fermi-level-dependent charge-to-spin current conversion by Dirac surface state of topological insulators. *Nature Phys.* **12**, 1027–1031 (2016)

77. Deorani, P. *et al.* Observation of inverse spin Hall effect in bismuth selenide. *Phys. Rev. B* **90**, 094403 (2014).

78. Jamali, M. *et al.* Giant spin pumping and inverse spin Hall effect in the presence of surface and bulk spin-orbit coupling of topological insulator Bi_2Se_3. *Nano Lett.* **15**, 7126–7132 (2015).

79. Wang, H. *et al.* Surface-state-dominated spin-charge current conversion in topological-insulator–ferromagnetic-insulator heterostructures. *Phys. Rev. Lett.* **117**, 076601 (2016)

80. Liu, L. *et al.* Spin-polarized tunneling study of spin-momentum locking in topological insulators. *Phys. Rev. B* **91**, 235437 (2015).

81. Li, C. H. *et al.* Electrical detection of charge-current-induced spin polarization due to spin momentum locking in Bi_2Se_3. *Nature Nanotech.* **9**, 218–224 (2014).

82. Tang, J. *et al*. Electrical detection of spin-polarized surface states conduction in $(Bi_{0.53}Sb_{0.47})_2Te_3$ topological insulator. *Nano Lett.* **14**, 5423–5429 (2014).

83. Ando, Y. *et al.* Electrical detection of the spin polarization due to charge flow in the surface state of the topological insulator $Bi_{1.5}Sb_{0.5}Te_{1.7}Se_{1.3}$. *Nano Lett.* **14**, 6226–6230 (2014).

84. Dankert A., Geurs J., Kamalakar M. V. & Dash S. P. Room temperature electrical detection of spin polarized currents in topological insulators. *Nano Lett.* **15**, 7976–7981 (2015).

85. Fan, Y. *et al.* Magnetization switching through giant spin-orbit torque in a magnetically doped topological insulator heterostructure. *Nature Mater.* **13**, 699–704 (2014)

86. Fan, Y. *et al.* Electric-field control of spin–orbit torque in a magnetically doped topological insulator. *Nature Nanotech*. **11**, 352–360 (2016).

87. Jiang, Z. *et al.* A comparative transport study of Bi_2Se_3 and Bi_2Se_3/yttrium iron garnet. *Appl. Phys. Lett.* **104**, 222409 (2014).

88. Jiang, Z. *et al.* Independent tuning of electronic properties and induced ferromagnetism in topological insulators with heterostructure approach. *Nano Lett.* **15**, 5835–5840 (2015).

89. Jiang, Z. *et al.* Structural and proximity-induced ferromagnetic properties of topological insulator-magnetic insulator heterostructures. *AIP Adv.* **6**, 055809 (2016).

90. Tang, C. *et al.* Exquisite growth control and magnetic properties of yttrium iron garnet thin films. *Appl. Phys. Lett.* **108**, 102403 (2016)

91. Zhang, J. *et al*. Band structure engineering in $(Bi_{1-x}Sb_x)_2Te_3$ ternary topological insulators. *Nature Commun.* **2**, 574 (2011).

92. Wilk, G.D., Wallace, R.M. & Anthony, J.M. High-κ gate dielectrics: current status and materials properties considerations. *J. Appl. Phys.* **89**, 5243–5275 (2001).